D5.5 Occupant models

Primary Author(s)	Klein Christoph | VIF Johan Davidsson | Chalmers
Related Work Package	5
Version/Status	1.0| Final
Issue date	01/03/2023
Deliverable type	R
Dissemination Level	PU
Project Acronym	SAFE-UP
Project Title	proactive SAFEty systems and tools for a constantly UPgrading road environment
Project Website	www.safe-up.eu
Project Coordinator	Núria Parera | Applus IDIADA
Grant Agreement No.	861570

This project has received funding from the European Union's Horizon 2020 research and innovation programme under Grant Agreement 861570.

Co-Authors

Name	Organisation
Yash Niranjan Poojary	Chalmers
Johan Iraeus	Chalmers
Domink Breitfuss	Virtual Vehicle

Document Distribution

Version	Date	Distributed to
0.3	30.05.2023	Coordination Team
1.0	30.05.2023	Submission in the EC System
		Approved by the EC

This project has received funding from the European Union's Horizon 2020 research and innovation programme under Grant Agreement 861570.

Copyright statement

This project has received funding from the European Union's Horizon 2020 research and innovation programme under Grant Agreement 861570.

Executive summary

This report documents enhancements on Human Body Models (HBMs) for the lumbar spine, the pelvic bone, a study on occupant kinematics in pre-crash manoeuvres and the enhancement of an active kinematics controller for HBMs.

A new lumbar spine model and associated injury risk function

Lumbar spine fractures have been identified as a problem in motor vehicle crashes, and it is expected that this problem might increase with the introduction of reclined postures in autonomous vehicles. Human body models provide a mean to address this issue and develop countermeasures. In SAFE-UP a finite element lumbar spine model intended for use in advanced HBMs and previously developed in the EU-project OSCCAR has been improved, and its biofidelity has been tuned and validated. In addition, a tissue-based injury risk function for use with the new lumbar spine model was developed and validated. The injury risk function was based on trabecular compressive strain in the superior-inferior direction.

The kinematic and kinetic validation showed that the model compared reasonably to experimental data, with axial compression and flexion predictions being closest to experimental results. The model was found to be morphable to several anthropometries with maintained element quality. The new risk function was found to have a good quality index.

Even though the model evaluations indicated that the onset of fracture risk was somewhat overpredicted, it was judged that the current model together with the associated injury risk function can be used to estimate the risk for compressive fractures in the lumbar spine, with the knowledge that these estimates are most likely somewhat conservative.

Updates on pelvic bone

Pelvic fracture remains one of the most common AIS2+ moderate to severe injuries in vehicle crashes. A fundamental tool for the development of superior restraints are finite element HBMs. Several of these models have superior thorax and head response, but state-of-the-art pelvis models are less matured. In SAFE-UP, new detailed pelvis finite element models of the average male and female were developed. The models, including bone and pubic symphysis joint and lumbosacral joint properties, were tuned, and evaluated using published force-displacement data from post-mortem human subjects subjected to lateral loading of the denuded pelvis.

The force-displacements showed that the model compared reasonable to experimental data in lateral loading. The model was found to be morphable to several anthropometries with maintained element quality.

Volunteer study

To determine the occupant kinematics in reclined sitting positions in typical pre-crash manoeuvres like braking or steering, a volunteer study was conducted. 27 male and 12 female participants were seated in an automated driven vehicle (sedan) on the co-driver side. A seat with a seat-integrated belt was mounted in the vehicle instead of the serial seat

This project has received funding from the European Union's Horizon 2020 research and innovation programme under Grant Agreement 861570.

to allow a reclined sitting position without any belt slack. Braking and steering manoeuvres in aware and unaware state in reclined and upright sitting position at two different velocities (30 km/h, 50 km/h) were driven, which resulted in 11 manoeuvres per volunteer.

Two motion capturing systems (Video based and redundant inertia sensors) were used to determine the kinematics. The vehicle accelerations were recorded, as well as the occupants' pressure on the seat and the muscle activity. Prior to the tests, the anthropometry of the volunteers was documented.

A statistical approach was used to analyse the kinematics and to develop mathematical models which can predict the kinematics for each manoeuvre based on anthropometric parameters, age, and gender.

Active kinematics controller

As the pre-crash kinematics of the occupant has an influence on the in-crash kinematics [99] and on the injury risk [101], models are required which can depict occupant motion in braking and steering manoeuvres. Several approaches exist to enhance (passive) Human Body Models (HBMs) with active muscles. The method, which was enhanced in this project, uses torque controllers, which are mounted on each vertebra in the FE HBM and are controlled by an external PD controller. A braking scenario was chosen to develop the controller principle for reclined sitting positions. A THUMSv3 was used as the HBM, and the target kinematic data was taken from the conducted volunteer study in this project.

This project has received funding from the European Union's Horizon 2020 research and innovation programme under Grant Agreement 861570.

Table of contents

1. Introduction 14
1.1 Development of a lumbar spine model and associated injury risk function 14
1.2 Development of a pelvis model 15
1.3 Volunteer study 15
1.4 HBM active torque controller 15

2. Development of a lumbar spine model and associated injury risk function 16
2.1 Methods 16
2.1.1 Development of a lumbar spine model 16
2.1.2 Tuning of nucleus properties and ligament initial length 18
2.1.3 Kinematic and kinetic validation of lumbar spine model 19
2.1.4 Development of an Injury Risk Function 20
2.1.5 Evaluation of the Injury Risk Function 22
2.2 Results 23
2.2.1 Development of a lumbar spine model 23
2.2.2 Tuning of nucleus properties and ligament initial length 24
2.2.3 Kinematic and kinetic validation of the new lumbar spine model 25
2.2.4 Development of an Injury Risk Function 25
2.2.5 Evaluation of the Injury Risk Function 27
2.3 Discussion 28
2.4 Conclusions 31

3. Development of a pelvis model 32
3.1 Methods 32
3.1.1 Development of a morphable pelvis model 32
3.1.2 Tuning of joint properties 34
3.1.3 Validation of the new pelvis model 35
3.1.4 Positioning and integration into the VIVA+ model 36
3.2 Results 37
3.2.1 Development of a new pelvis model 37
3.2.2 Tuning of joint properties 37
3.2.3 Validation of the new pelvis model 39

This project has received funding from the European Union's Horizon 2020 research and innovation programme under Grant Agreement 861570.

3.2.4 Positioning and integration into the VIVA+ model 41
3.3 Discussion 41
3.4 Conclusions 43
4. Volunteer study 44
4.1 Test vehicle and performed manoeuvres 44
4.2 Volunteer characteristics 46
4.2.1 Pre survey 47
4.2.2 Vehicle survey 48
4.3 Data acquisition, -processing and analysis 49
4.3.1 Measurement equipment 49
4.4 Results 51
4.4.1 Vehicle kinematic 51
4.4.2 Occupant kinematic 51
4.4.3 Pressure mat data 54
4.4.4 Muscle activity 54
4.5 Conclusion 58
5. Active HBM torque controller 59
5.1 Environment 59
5.2 Controller 60
5.2.1 Surrogate model and inverse model 61
5.3 Determination of the controller parameters 61
5.4 Controller application 62
5.4.1 Selected manoeuvre and occupant response 62
5.4.2 Results with active controller 63
5.5 Conclusion and next steps 64
6. Dissemination and Exploitation 65
References 66
Appendix A – Comparisons between predicted and biomechanical lumbar FSU responses 74
Appendix B – Available PMHS data for IRF 77

This project has received funding from the European Union's Horizon 2020 research and innovation programme under Grant Agreement 861570.

Appendix C – Inclusion and exclusion of PMHS test data 80

Appendix D – Reconstructions of original tests 81

FSU in pure compression by Brinckmann et al.1989 81

Lumbar FSU Pure compression by Duma et al. 2006 81

Lumbar FSU Pure compression by Granhed et al. 1989 82

Lumbar FSU Flexion-compression by Hutton and Adams 1982 82

Lumbar FSU Flexion-compression by Tushak et al. 2022 83

Appendix F – Occupant response corridors 84

This project has received funding from the European Union's Horizon 2020 research and innovation programme under Grant Agreement 861570.

List of figures

Figure 1: Left: Example mesh for the L4-L5 FSU. Right: modelling of intervertebral disc (the annulus ground substance and nucleus pulposus is removed from half of the disc in the figure for visualization..... 17

Figure 2: Tuning of ligament initial unstretched length by adding one ligament or other anatomical structure at a time and comparing the force deflection properties to [41,42] ... 18

Figure 3: Validation load cases; left Yamamoto [43] and right Demetropoulos [44]. The orange arrows show the directions of the deformations applied. 20

Figure 4: FSU tests used to create IRF. From left to right; Brinkman[47], Duma [48], Granhed [49], Hutton [50], and Tushak [51]. The orange arrows show the directions of the deformations applied. The green cross marks the rotation centre and the yellow arrow indicates that the end was free to translate in that DOF, and finally the orange diagonal patterns mark that these ends were fixed. 21

Figure 5: Evaluation of IRF, left Ortiz-Paparoni [52] and right Yoganandan [55] 23

Figure 6: Images of the new lumbar spine model assembled into the VIVA+ 50F (left) and 50M (right) HBMs. The measurements defined in the figures are, Lumbar Lordosis angle (LL) measured from superior edge of the L1 vertebrae body to the superior edge of the L5 vertebrae body [56], and LumboSacral Lordosis angle (LSL) defined as the angle between the line from L5 centre to L3 centre and the line between L5 centre and S1 centre [58]. .. 24

Figure 7: Resulting force-deflection for L4-L5 FSU in axial compression (left) and axial tension (right) after nucleus pulposus material tuning, compared to[37-40]. 24

Figure 8: Validation of whole spine rotational kinematics and kinetics [54], left: Flexion-Extension, mid: Lateral bending, and right: Axial rotation (same scale used in all plots for easier comparison of magnitudes) 25

Figure 9: Validation of whole spine translational kinematics and kinetic [55], left: Compression-Tension, mid: Posterior-Anterior shear, and right: Lateral shear (same scale used in all plots for easier comparison of magnitudes) 25

Figure 10: Injury risk curves recommended for use with the new lumbar spine model and for a 50-year-old male and female (left) and for a male 25, 50 and 75 years of age (right). ... 26

Figure 11: Results from evaluation of IRF. Left according to Ortiz-Paparoni [63], where the blue line represents the force-based injury risk from the PMHS tests (combination of spine curvatures), and the symbols represents the estimated injury risk from the simulation model, for the neutral, pre-flexed and pre-extended spines. Right according to Yoganadan et al. [66], dark grey bars represent the tests where fracture occurred in the lumbar spine. Light

This project has received funding from the European Union's Horizon 2020 research and innovation programme under Grant Agreement 861570.

grey bars represent tests not leading to spine fracture. Only the most severe tests when there was no injury are displayed. 28

Figure 12: FE pelvis models used in this study (left 50F and right 50M). 32

Figure 13: Distribution of the cortical bone thickness shown for the 50F model (the 50M model have the same thickness distribution). 33

Figure 14. Test set-up according to (Dakin 2001) used in the tuning of the pubic symphysis joint. 34

Figure 15: Test set-up according to (Miller 1987) used in the tuning of the sacroiliac joints. 35

Figure 16: Test set-up according to (Guillemot 1998) used in the validation of the pelvis model. 36

Figure 17. Orientation of pelvis, PA=Pelvis Angle, PT= Pelvis Tilt, SS= Sacral Slope 36

Figure 18. Positioning of the pelvis inside the hip. A-F distance is the distance form the ASIS to the skin surface, and AT height is the vertical distance from ASIS to a line extended from the leg upper surface 37

Figure 19. Tuning of the Pubic Symphysis joint properties in tension and compression. 38

Figure 20. Force deformation plots comparing the predicted response to responses presented in Li (2006) 38

Figure 21: Tuning results for the Sacroiliac joint properties in tension and shear and bending. 39

Figure 22. Comparison of pelvis predictions to physical test results in Guillemot static Iliac crest loading test. 39

Figure 23. Comparison of pelvis predictions to physical test results in Guillemot static acetabulum loading test. 40

Figure 24: Comparison of pelvis predictions to physical test results in Guillemot dynamic acetabulum loading test. 40

Figure 25: Test site with schematic sequence 44

Figure 26: Ford Mondeo - Virtual Vehicle Research GmbH 45

Figure 27: Distribution of height, weight and age of the volunteers 46

Figure 28: Pre-survey procedure 47

This project has received funding from the European Union's Horizon 2020 research and innovation programme under Grant Agreement 861570.

Figure 29: Vehicle interior with measured points 48

Figure 30: Measured volunteers in the test vehicle 49

Figure 31: Vehicle acceleration values for all performed tests 51

Figure 32: Coordinate system with evaluated segments for the quantification of occupant movement 52

Figure 33: Definition of front and side angle 52

Figure 34: Response corridors for the thorax (50th percentile +/- 25%) in 30 kph and 50 kph braking manoeuvres, reclined and upright sitting position and for male and female anthropometry 53

Figure 35: Exemplary evaluation of a pressure distribution for seat and backrest (left: start position, right: maximum lateral displacement of occupant) 54

Figure 36: Development of a FE seat model based on images 59

Figure 37: Concept of the active torque controller 60

Figure 38: Surrogate model of the torso and head/neck 61

Figure 39: Controller parameter determination with the surrogate model 62

Figure 40: Predicted occupant response (head and torso angle) and vehicle acceleration for a 50kph braking manoeuvre in aware and unaware state 63

Figure 41: Head/neck angle of the active torque controlled HBM 63

This project has received funding from the European Union's Horizon 2020 research and innovation programme under Grant Agreement 861570.

List of tables

Table 1: THE FINAL DATASET USED IN THE DEVELOPMENT OF RISK CURVES 22

Table 2: Distribution and parameters for the injury risk function recommended for the new lumbar spine model (Female: 0 and Male: 1). 26

Table 3: Injury risk and quality index for risk curves for 50-year-oldamle and female..... 27

Table 4: Manoeuvre overview for each volunteer..... 45

Table 5: Measurements in the vehicle interior 48

Table 6: Measurement devices 49

Table 7: Muscle activity in a 50kph braking manoeuvre..... 55

Table 8: Muscle activity in a steering (left) manoeuvre 56

Table 9: Muscle activity in a steering (right) manoeuvre 57

This project has received funding from the European Union's Horizon 2020 research and innovation programme under Grant Agreement 861570.

List of abbreviations

Abbreviation	Meaning
AV	Autonomous Vehicles
AD	Autonomous Driving
CA	Consortium Agreement
CAV	Connected Automated Vehicles
D	Deliverable
EC	European Commission
GA	Grant Agreement
HBM	Human Body Model
MaaS	Mobility as a Service
OEM	Original Equipment Manufacturer
PM	Person Month
R&D	Research and Development
SC	Steering Committee
SotA	State-of-the-Art
T	Task
VRU	Vulnerable road user
WP	Work Package
ALL	Anterior Longitudinal
PLL	Posterior Longitudinal
LF	Flavum
ITL	Intertransverse Ligaments
ISL	Interspinous Ligaments
SSL	Supraspinous Ligaments
FC	Facet Capsular

This project has received funding from the European Union's Horizon 2020 research and innovation programme under Grant Agreement 861570.

1. Introduction

1.1 Development of a lumbar spine model and associated injury risk function

Epidemiology studies have identified lumbar spine fractures to be a problem in motor vehicle collisions [1][2][3][4][5][6][7]. While these injuries are overrepresented in crash types including a vertical crash pulse component, they are also frequent in frontal impacts without a vertical component [2][3][6][7]. It has also been shown that the incidence has increased for newer vehicles [2][4][5][7]. Many studies have identified vertebrae compression and wedge fractures, at levels T12-L1, resulting from axial compression and flexion, as the most frequent injury type and location [2][4][6]. These findings have also been confirmed in frontal crash test using belted Post-Mortem Human Subjects (PMHSs) [8][9][10][11][12]. With the introduction of autonomous vehicles, it is expected that vehicle passengers will ride in more reclined positions than is common today. This may increase the lumbar spine load in frontal crashes [11][12][13][14][15][16]. Thus, it is possible that this injury type will increase even more in future if not properly addressed.

Finite Element (FE) Human Body Models have been shown to be a good complement to traditional crash test dummies, as these can predict omnidirectional kinematics and kinetics and offers the possibility to evaluate injury at the tissue level. Examples of some contemporary FE-HBMs for occupant safety are the Total Human Model for Safety (THUMS) [17], the Global Human Body Model Consortium (GHBMC) model [18], the SAFER HBM [19], and the VIVA+ HBM [31]. While both the THUMS (version 4+) and the detailed GHBMC models include detailed lumbar spine models, validation presented in the open literature is lacking. An exception is the validation of the detailed GHBMC lumbar spine model in axial compression and flexion presented in [32], where the authors concluded that the model lacked somewhat in biofidelity. The SAFER HBM as well as the VIVA+ models have simplified lumbar spines, partly modelled as rigid structures, not suitable for tissue-based injury evaluation.

Lumbar spine injury risks are currently estimated based on cross sectional forces and moments, using Injury Risk Functions (IRFs) developed from biomechanical testing. While this can work sufficiently when an average sized HBM are used, it is insufficient for morphed HBMs, as most IRFs normally do not include size dependent covariates. A more attractive way of evaluating lumbar spine injury risks using HBMs is to use a tissue based IRF (for example stress or strain), which automatically scales with spine dimensions. None of the four HBMs presented above have an associated tissue based IRF for prediction of lumbar spine fracture risk.

Thus, the aim of this part of the SAFE-UP project was to improve an existing lumbar spine finite element model, tune and validate the model performance against PMHS test results. In addition, the aim was to generate an associated tissue level IRF for compression fractures

This project has received funding from the European Union's Horizon 2020 research and innovation programme under Grant Agreement 861570.

in the vertebrae. To maximize the use of the models, a model of an average male and a model of an average female will be licensed as open source.

1.2 Development of a pelvis model

Pelvic fractures are the third most common moderate to severe injury in motor vehicle crashes [20]. For lateral impacts specifically, the pelvic fractures are the dominating lower extremity injury [21]. In addition, pelvis bone geometry and its interaction with the lap belt segment determines the risk of submarining injuries. The most human like and an important tool for developments of advanced occupant restraints with superior protection are finite element HBMs. Several pelvis FE-HBMs for impact evaluations exist in the literature [22][23][24][25][26][27][28][29][30]. However, the available pelvis models are not adequate in terms of injury prediction and the ability to be morphed to the pelvis shape variance of the population at risk. Therefore, a new detailed pelvis finite element model, morphable to the anthropometry of the population at risk, was developed.

1.3 Volunteer study

To include the kinematics during the pre-crash phase (usually braking or steering) in the injury assessment, the knowledge of the pre-crash occupant kinematics is necessary. Moreover, the automated driving functions will allow different sitting positions. Therefore, a volunteer study, which gains knowledge of occupant behaviour in reclined and upright sitting positions was conducted with 12 female and 27 male volunteers.

1.4 HBM active torque controller

The prediction of pre-crash kinematics with HBM requires the modelling or the depiction of muscle activity at least in the spine. Several methods can be found in literature, where usually single muscles, or muscle groups are modelled and controlled. That requires the determination of numerous controller parameters. The method which is enhanced in this project is an active torque controller, which uses one active element for every vertebra. The controller parameters are determined for a reclined sitting position in a braking manoeuvre in the conducted volunteer study.

This project has received funding from the European Union's Horizon 2020 research and innovation programme under Grant Agreement 861570.

2. Development of a lumbar spine model and associated injury risk function

In this study a detailed finite element lumbar spine model was extensively improved, tuned and validated, and an associated tissue-based injury risk function were constructed and validated. The injury risk function was based on trabecular compressive strain in the superior-inferior direction. Finally, the model was morphed to the anthropometry of an average male and female and made available open-source.

2.1 Methods

A detailed FE lumbar spine model, modelled with a high-quality mesh to enable tissue base injury criteria and morphing, was created based on literature data. Specifically, the ligament unstretched length and the nucleus pulposus material properties were tuned based on Functional Spine Unit (FSU) data. Next, the kinetics and kinematics of the lumbar spine model were validated using published biomechanical data. Finally, a tissue based IRF targeting compression fractures in the spinal column was developed and evaluated. All simulations except the IRF evaluations were carried out using LS-DYNA MPP R11.1.0 (ANSYS/LST, Livermore, CA). The IRF evaluations were carried out using LS-DYNA MPP R12.1.0 (ANSYS/LST, Livermore, CA). Meshing and other pre-processing were done using ANSA (Beta CAE Systems, Luzern, Switzerland), post-processing using LS-PREPOST (ANSYS/LST, Livermore, CA) and Hypergraph (Altair, Troy, MI), and development of the IRFs in R (Vienna, Austria).

2.1.1 Development of a lumbar spine model

A detailed lumbar spine FE mesh, with mesh quality criteria according to [19], was created using a hexa block design, see Figure 1 for an example of the L4-L5 FSU. The geometry was based on an average sized female [34]. The trabecular bone was modelled using reduced order hexahedral elements, while the cortical bone and endplates were modelled using fully integrated quad shell elements.

The trabecular bone material (main interest for capturing compression fractures in this study) was modelled in detail using an orthotropic material model (*MAT_ORTHOTROPIC_ELASTIC) with young's modulus in main (inferior-superior) direction based on [35], and with all other orthotropic constant scaled from the main direction using information from [36]. The trabecular bone in the posterior part of the vertebrae, of less importance for the compression fractures, were modelled using an isotropic material model (*MAT_PIECEWISE_LINEAR_PLASTICITY), with Young's modulus like the Young's modulus in the main direction of the vertebrae body.

This project has received funding from the European Union's Horizon 2020 research and innovation programme under Grant Agreement 861570.

The thicknesses (range 0.51-0.82 mm) of the cortical shells and endplates of the vertebrae bodies were defined according to [37], and then interpolated between reported sites. The cortical bone was modelled using an anisotropic material model (*MAT_ANISTROPIC_ELASTIC_PLASTIC), assuming a transversely isotropic material (assumed superior-inferior to be main direction), with material constants fitted based on [38]. Similar to the trabecular bone the cortical bone in the posterior part was modelled using an isotropic material model with parameters according to [38]. The endplates were also modelled using an isotropic material model, with material constants according to [39].

The intervertebral discs were modelled using a combination of reduced order solid and fully integrated membrane elements. The annulus fibrosis was modelled using three layers of membrane elements, see Figure 1. The fibre directions of each layer (outer ± 64°, middle ± 54°, and inner ± 45°) were assigned according to [40] and the membrane thicknesses according to [41]. The annulus fibres were modelled using a tensile only material model for fabrics (*MAT_FABRIC), with a nonlinear stress-strain relationship according to [42]. The annulus ground substance and nucleus pulposus were modelled using solid elements. The dimension of the nucleus was defined to be about 40% of the total disc area [43]. The annulus ground substance was modelled using a foam material model (*MAT_HILL_FOAM), with material parameters according to [44], while the nucleus pulposus was modelled using a rubber material model (*MAT_OGDEN_RUBBER) with material constants tuned to fit the average response in FSU compression tests (see next section). The Anterior Longitudinal (ALL), Posterior Longitudinal (PLL), Flavum (LF), Intertransverse (ITL) and Interspinous + Supraspinous (ISL+SSL) ligaments were modelled using non-linear elastic beam elements (*MAT_ELASTIC_SPRING_DISCRETE_BEAM) with force-deflection properties according to [45] and strain rate properties according to [46]. The Facet Capsular (FC) ligament instead used force-deflection properties according to [47].

No element erosion was implemented for any of the tissues modelled. An automatic single surface contact, with friction coefficient of 0.1, was defined including all shells and membrane elements in the lumbar spine.

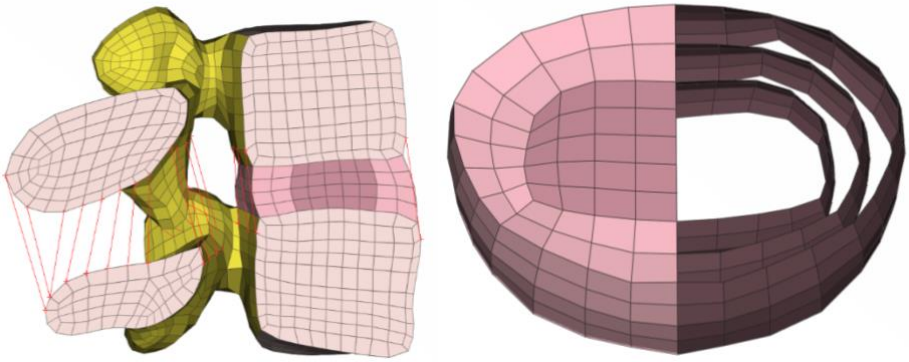

Figure 1: Left: Example mesh for the L4-L5 FSU. Right: modelling of intervertebral disc (the annulus ground substance and nucleus pulposus is removed from half of the disc in the figure for visualization.

This project has received funding from the European Union's Horizon 2020 research and innovation programme under Grant Agreement 861570.

2.1.2 Tuning of nucleus properties and ligament initial length

The Ogden material parameters for the nucleus pulposus were manually tuned to fit FSU compression [48][49][50][51] and tension [49] responses. To capture the non-linear force-deflection behaviour seen in the tests, three terms controlling the shear modulus were included. No viscous terms were included, meaning that strain rate effects were not modelled.

As the data sources for ligament mechanical properties [45][47] do not report the initial unstretched length corresponding to a neutral spine posture, this unstretched length had to be reverse-engineered (tuned) from lumbar spine FSU tests. This was done by simulating the stepwise reduction L4-L5 FSU tests reported in [52][53] (see Figure 2). First a model without any ligaments was simulated (step 1 in Figure 2). Then ligaments or other anatomical structures were added once at a time and new simulations were run. This was carried out all the way to the intact FSU (step 8 in Figure 2). At each step, the added ligament initial unstretched length was tuned, to match the moment-rotation curves from the physical tests. The tuning was done by translating the ligament force-deflection curve along the abscissa, introducing either ligament pre-stretch or slack. For each step, flexion, extension, lateral bending as well as axial rotation were simulated and compared to the physical tests. As the two data sets used L4-L5 FSUs from both male and female donors, the L4-L5 FSU FE model (matching an average female in size) was volumetrically scaled by 1.05 to match an FSU size in between an average male and female (basing the scaling from female to male on stature). Finally, a parameter “LUMB_FLEX” was introduced. This parameter scales the ligament pre-stretch/slack depending on the spine initial curvature. Recommended values are -1 for a lordotic (neutral) spine, typical for a standing person, and 0 for a straight (flexed) spine, typical for a seated vehicle occupant. The same scaling was used for ligaments at all levels of the lumbar spine.

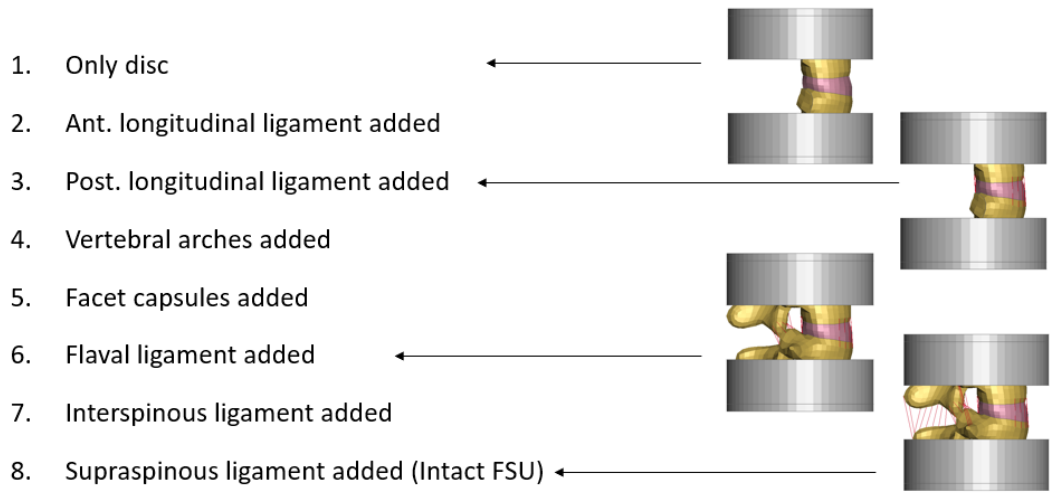

Figure 2: Tuning of ligament initial unstretched length by adding one ligament or other anatomical structure at a time and comparing the force deflection properties to [41,42]

This project has received funding from the European Union’s Horizon 2020 research and innovation programme under Grant Agreement 861570.

2.1.3 Kinematic and kinetic validation of lumbar spine model

Kinematic and kinetic whole lumbar spine validation was performed by comparing the predictions from the complete lumbar spine model to two reference data sets [54][55]. The first reference test series, performed by Yamamoto [54], included 10 lumbar spines from PMHSs aged between 25 and 63 years, but of unknown sex, stature, and weight. The second reference test series, performed by Demetropoulos [55], included 10 lumbar spines (8M/2F) from PMHSs with an average stature of 173 cm, an average weight of 73 kg and an average age of 60 years. As one of the data sets included specimens from both sexes and the PMHSs of the other dataset were of unknown sex, the simulation model (originally matching an average female in size) was volumetrically scaled with a factor of 1.05, which corresponds to a target size in between average females and males.

In the Yamamoto test series, the sacral vertebrae (and pelvis) were constrained in an epoxy block rigidly attached to the test table (see Figure 3 left). At the superior end the L1 vertebrae was also potted in another epoxy block. The potting was modelled using an elastic material model (*MAT_ELASTIC) with Young's modulus 2 GPa. The spine was connected to the potting using a penalty based constrain (*CONSTRAINED_SHELL_IN_SOLID_PENALTY). Pure moment loads (extension-flexion, lateral bending, and axial rotation) in steps of 2.5 Nm up to 10 Nm, were separately applied to the superior potting, and rotations were recorded at each vertebrae level. The superior potting was free to move in all directions, except the one currently tested. Based on the figures and the description in [54] it was estimated that the spine was initially in a neutral (lordotic) position corresponding to a "LUMB_FLEX" parameter of -1.

In the Demetropoulos test series, the T12 vertebrae were constrained in epoxy, rigidly attached to the test fixture (see Figure 3 right). At the inferior end, L5 was also potted in epoxy. The potting material and connection between the potting and the spine was modelled in the same way as in the first load case. Compression (up to 6.5 mm), tension (up to 2.5 mm), anterior-posterior shear (up to 35 mm) and lateral shear (up to 13 mm) was applied to the inferior potting. The superior potting was constrained in all degrees of freedom. Based on the figures and the description in [55] it was estimated that the spine was in a neutral (lordotic) position corresponding to a "LUMB_FLEX" parameter of -1.

This project has received funding from the European Union's Horizon 2020 research and innovation programme under Grant Agreement 861570.

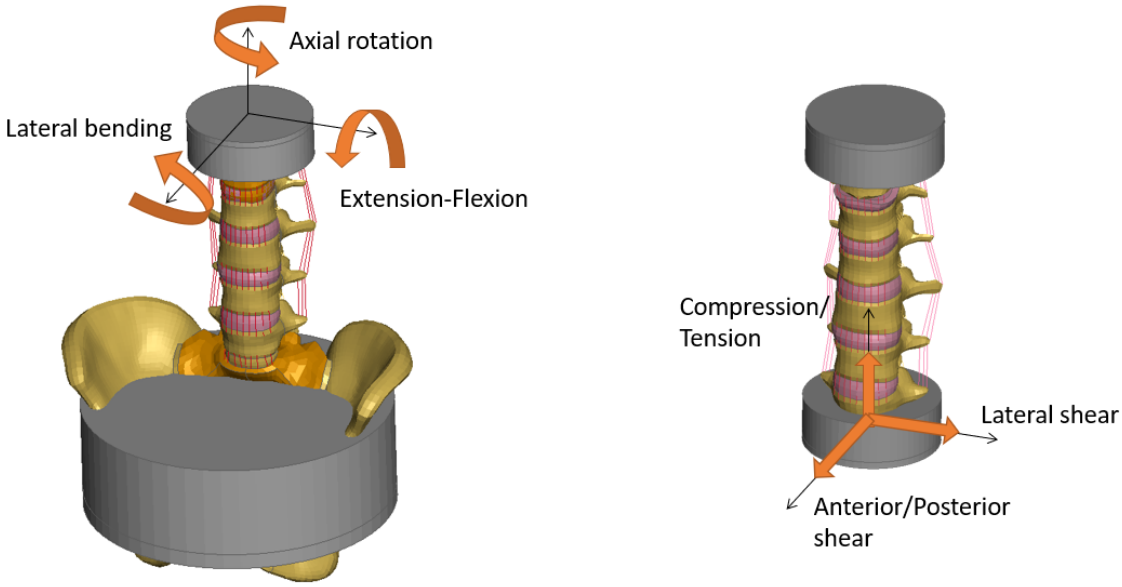

Figure 3: Validation load cases; left Yamamoto [43] and right Demetropoulos [44]. The orange arrows show the directions of the deformations applied.

2.1.4 Development of an Injury Risk Function

This study followed the guidelines defined by ISO/TC22/SC12/WG6 [56] and those presented in [57] in the construction of IRFs. In brief, an in-depth literature review was conducted to identify available datasets for reconstructions (see Appendix B – Available PMHS data for IRF). The tests selected, based on developed inclusion and exclusion criteria

(see Appendix C – Inclusion and exclusion of PMHS test data), were those where two and three vertebral body FSUs were loaded in compression and combined flexion-compression. The specimens were from donors with an average age of 46 years, but of unknown stature and weight. The proportion of men doners were 64%. These tests were successfully reproduced with sub-models, scaled to either that of on average female or male, of the developed lumbar spine model (Figure 4). See additional information on test and reconstruction of these tests in Appendix D – Reconstructions of original tests.

The injury to the FSUs were scored, either an endplate fracture or uninjured, and assigned censoring, exact or right (tests that did not result in any injury). The selected injury metric was the inferior-superior compressive strain in the trabecular bone of the vertebrae body.

This project has received funding from the European Union's Horizon 2020 research and innovation programme under Grant Agreement 861570.

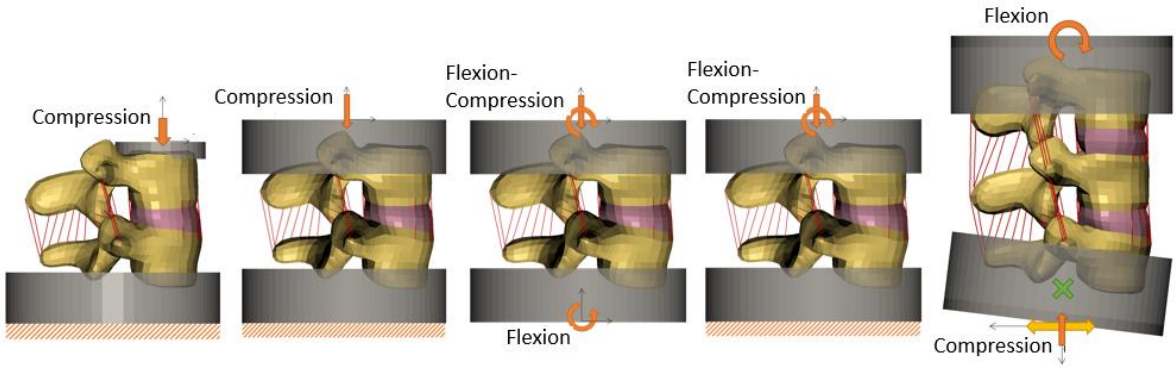

Figure 4: FSU tests used to create IRF. From left to right; Brinkman[47], Duma [48], Granhed [49], Hutton [50], and Tushak [51]. The orange arrows show the directions of the deformations applied. The green cross marks the rotation centre and the yellow arrow indicates that the end was free to translate in that DOF, and finally the orange diagonal patterns mark that these ends were fixed.

Finally, the injury metric from the simulations and the injury scores from the original FSU tests were used to construct an IRF using parametric survival analysis using the R package "flexsurv". As part of the analysis, the effect of subject characteristics was studied using Cox regression for multiple covariates. The characteristics assessed were age, sex, level of vertebrae (L1/L2 – ordinate 1, L2/L3 – ordinate 2, L3/L4 – ordinate 3, L4/L5 – ordinate 4, T12-L1-L2 - ordinate 5, L3-L4-L5 – ordinate 6) and data source (ordinate 1 to 5). The two latter characteristics were included to check for any influence of the test methods used in the original tests and vertebra level. Backwards stepwise regression was carried out using the R package "stepwiseCox" to select the final set of covariates. A p-value less than 0.05 inferred a statistical significance. In addition, an evaluation was conducted to assess any presence of bias within the dataset by analysing the distribution in the selected test data across both age and sex categories. Then overly influential observations were removed by using DFBETA analysis with a limit of 0.17. Thereafter the distribution assumptions were checked and evaluated to recommend the one that best predicts the true IRF. In short, the estimated risk curve for each of the three distributions (Weibull, log-normal and log-logistic) was compared with a spline function fitted to the simulation data. If any curve was substantially different from the spline, another distribution was considered. Then the distribution with the lowest Akaike Information Criterion (AIC) was selected. Finally, the 95% confidence interval of each IRF was calculated using the R package "confint". The relative size of the confidence interval was defined as the width of the 95% confidence interval at a given injury risk relative to the value of the stimulus at this same injury risk and was assigned a quality index (four categories were used – good from 0 to 0.5, fair from 0.5 to 1.0, marginal from 1.0 to 1.5 and unacceptable over 1.5). These indexes were calculated at 5%, 25% and 50% risks of injury.

The final IRF was constructed using data from tests and reconstructions of those test according to Table 1. Risk curves were constructed for 50-year-old females and 25, 50 and 75-year-old males for display.

This project has received funding from the European Union's Horizon 2020 research and innovation programme under Grant Agreement 861570.

Table 1: THE FINAL DATASET USED IN THE DEVELOPMENT OF RISK CURVES

Information source	Loading speed	Type of loading	Number of tests/ injured (proportion males %)
Brinckmann (1989)	1 kN/s	Compression	41/41 (51)
Granhed (1989)	0.0002 m/s	Compression combined with flexion 5, 10 or 15°	27/22 (67)
Hutton and Adams et al. (1982)	3 kN/s	Compression combined with initial flexion	24/24 (71)
Duma et al. (2006)	1 m/s	Compression	4/4 (100)
Tushak et al. (2022)	Compression 2.2-4.5 kN, Flexion 600 °/s	Compression followed by flexion	23/6 (70)

2.1.5 Evaluation of the Injury Risk Function

To evaluate the feasibility of the newly developed tissue based IRF, two reference test series were selected from literature. In the first test series performed by Ortiz-Paparoni, isolated lumbar spines were subjected to a combination of compression and flexion loading [63] (see Figure 5 left). Complete spines from 32 (only Duke data used) male specimens (average height 177 cm, mass 81 kg, and age 66 years) were tested. The sacrum and T12 were potted in firm plastic, modelled similarly as described in previous section. Different amount of flexion was assured by positioning the spine in three different curvatures: neutral, pre-flexed and pre-extended. The superior end was fixed, while the inferior end was moved with a constant velocity of 4 m/s. The fracture risk according to the newly developed IRF (for the age of 66 years), was computed for the different combinations of axial loads and spine curvatures. The elements in the superior half of the L1 vertebrae had to be excluded from the risk calculation, as these interacted with the simplified and rigid T12 in a non-biomechanical fashion. The results were then compared to the force-based risk curve developed in [63].

In the second test series reported by Yoganandan et al., whole PMHSs were subjected to underbody blast acceleration profiles of different shape and severity [64][65] (see Figure 5 right). Each PMHS was subjected to repeated loading of increased severity (seat cushion acceleration and velocity change) until fracture was observed in either the pelvis or the spine or the test was stopped. Seat cushion velocity changes ranged between 2.84 – 12.46 m/s and peak acceleration ranged between 9 -60 g. Five male PMHSs (average height 178 cm, mass 64 kg and age 63 years) were exposed of which one was uninjured, two sustained only pelvis fractures, one sustained pelvis and spine fractures, and one exhibited only a spine fracture. To reproduce the first two tests the model of the torso was laid flat on the seat back while for the other tests the model of the torso was somewhat flexed into a slouch

This project has received funding from the European Union's Horizon 2020 research and innovation programme under Grant Agreement 861570.

position to match the test conditions. All acceleration profiles from [66] were applied to seat base and foot support, the lumbar spine fracture risks were estimate using the newly developed IRF (using the actual age for each PMHS), and the results were compared to the outcomes from the physical tests. For this load case the lumbar spine model was assembled into the seated VIVA+ 50M HBM, version 1.0.0 [31]. The model was gravity settled during 300 ms before the under-blast pulse was applied, and a friction coefficient of 0.3 was used for the contact between the HBM and the test bench.

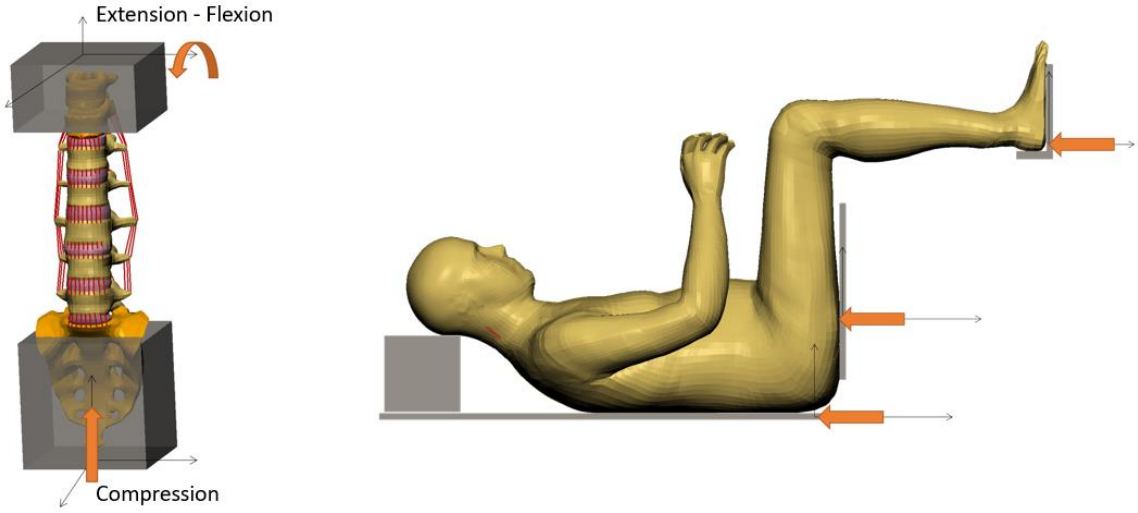

Figure 5: Evaluation of IRF, left Ortiz-Paparoni [52] and right Yoganandan [55]

2.2 Results

2.2.1 Development of a lumbar spine model

The final lumbar spine model, morphed to an average sized male and assembled into the seated VIVA+ 50M HBM can be seen in Figure 6. The lumbar spine model consists of about 10 000 shell elements with an average side length of 3.2 mm, 15 000 solid elements with an average side length of 2.8 mm, and 300 beam elements. In the assembled model the lumbar lordosis is 4°, which can be compared the average 0-6° for seated occupants [67][68]. The lumbosacral slope is 161°, which can be compared to the average 165° for seated occupants [69].

This project has received funding from the European Union's Horizon 2020 research and innovation programme under Grant Agreement 861570.

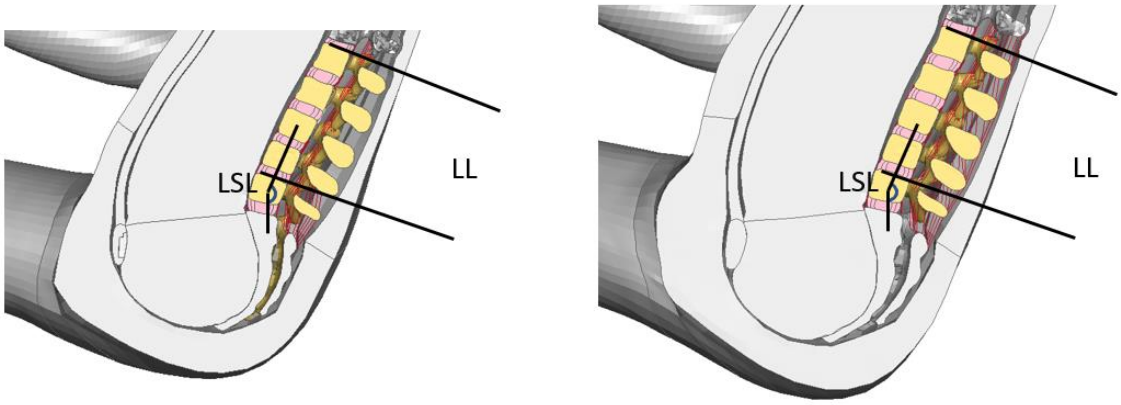

Figure 6: Images of the new lumbar spine model assembled into the VIVA+ 50F (left) and 50M (right) HBMs. The measurements defined in the figures are, Lumbar Lordosis angle (LL) measured from superior edge of the L1 vertebrae body to the superior edge of the L5 vertebrae body [56], and LumboSacral Lordosis angle (LSL) defined as the angle between the line from L5 centre to L3 centre and the line between L5 centre and S1 centre [58].

2.2.2 Tuning of nucleus properties and ligament initial length

The L4-L5 FSU model predictions in compression and tension were compared to the reference data in Figure 7. The predicted force-deflection response for compression was within the range of the physical tests, while the predicted tensile stiffness was slightly too high.

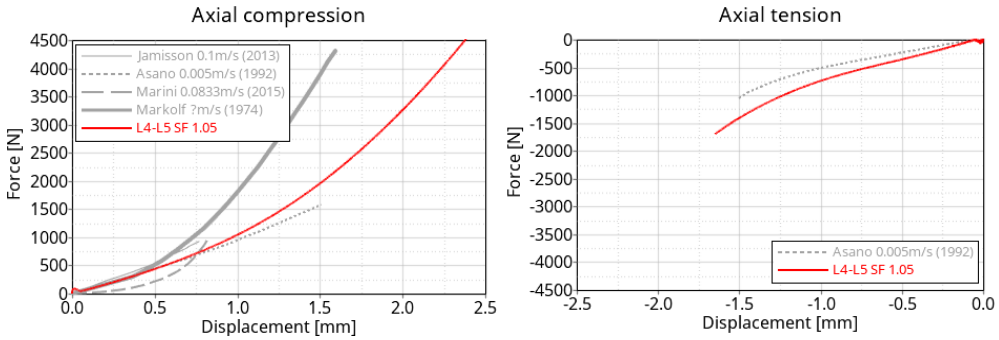

Figure 7: Resulting force-deflection for L4-L5 FSU in axial compression (left) and axial tension (right) after nucleus pulposus material tuning, compared to[37-40].

The results from the ligament initial length tuning can be seen in Appendix A – Comparisons between predicted and biomechanical lumbar FSU responses (see Fig. A 1 to Fig. A 8). Overall, the relative contribution from all ligaments and the vertebrae arches matches the physical test results, as seen by the close match in each of the eight steps. However, the stiffness in lateral bending was slightly too high, all the way from bending of the just the disc to bending of the complete FSU. Also, the stiffness in axial rotation is slightly too low in the complete FSU. To reach these results, the initial pre-stretch/slack that were added to the ligaments were, -1.5mm for ALL, +1.5mm for PLL, +2.0mm for FC and FL, and +5.0mm for ISL and SSL. These offsets will be included by setting the “LUMB_FLEX” parameter to -1.

This project has received funding from the European Union’s Horizon 2020 research and innovation programme under Grant Agreement 861570.

2.2.3 Kinematic and kinetic validation of the new lumbar spine model

The results from the whole spine rotational and translational kinematics and kinetics validation can be seen in Figure 8 and Figure 9. Generally, the model predictions were reasonably close to the physical experiments. The major deviation was seen for the posterior shear, where the model predicted a weaker response. Similar to the results from the FSU ligament tuning, the model predictions for the lateral bending stiffness were on the high side and for the axial rotation on the low side. Also, the transition to a higher stiffness started about 5° too early in flexion, and the low moment response (<9 Nm) for extension was on the stiff side.

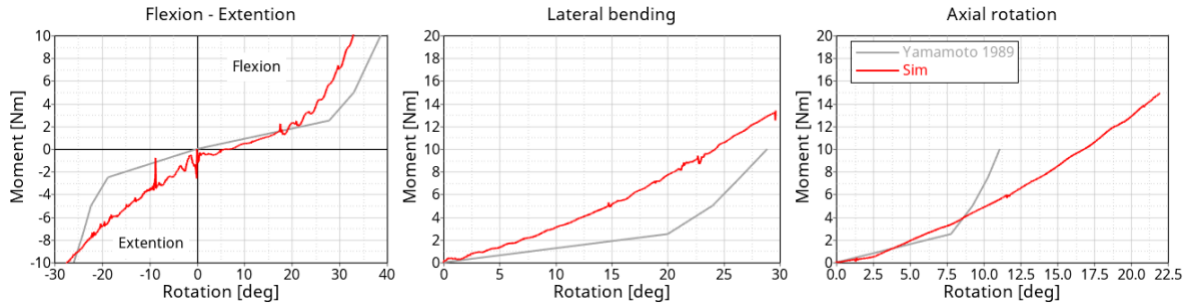

Figure 8: Validation of whole spine rotational kinematics and kinetics [54], left: Flexion-Extension, mid: Lateral bending, and right: Axial rotation (same scale used in all plots for easier comparison of magnitudes)

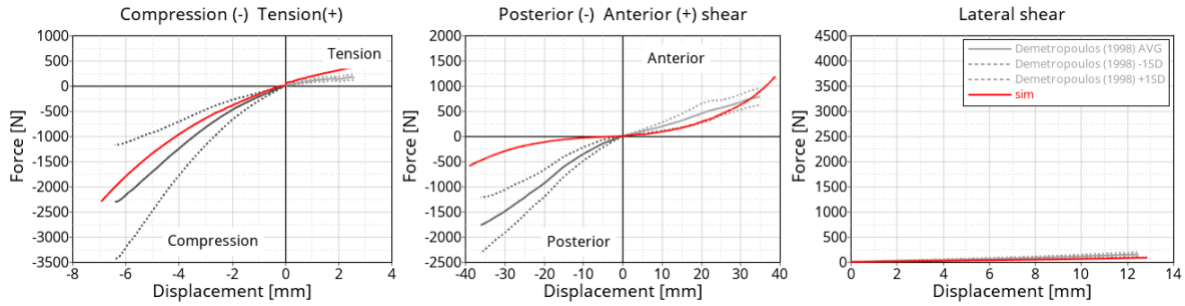

Figure 9: Validation of whole spine translational kinematics and kinetic [55], left: Compression-Tension, mid: Posterior-Anterior shear, and right: Lateral shear (same scale used in all plots for easier comparison of magnitudes)

2.2.4 Development of an Injury Risk Function

Statistical analysis – The Cox regression analysis for any effects of subject characteristics (age, sex, level of vertebrae and data source) revealed that the best model included age and sex covariates in the developed IRF. Further, an analysis on influential observations provided that a few observations (n=3) had to be removed prior to construction of the final IRF.

This project has received funding from the European Union's Horizon 2020 research and innovation programme under Grant Agreement 861570.

Injury risk function – An endplate fracture IRF recommended for use with the new lumbar spine model was developed using maximum inferior-superior compressive strain in the trabecular bone. Curves for a model representative of a 50-year-old female and a 25, 50 and 75-year-old male are provided in Figure 10.

Equation 1 with the coefficients given in Table 2 provide the lumbar spine IRF for the new lumbar spine model. The risk according to the log-normal distribution is:

$$\text{Risk} = \frac{1}{2} + \frac{1}{2}\,\text{erf}\left(\frac{\ln(\text{injury criteria}) - (\beta_1 + \text{age} * \text{coef}_{\text{age}} + \text{sex} * \text{coef}_{\text{sex}})}{\sqrt{2 * (\exp(\beta_2))^2}}\right) \quad (1)$$

Table 2: Distribution and parameters for the injury risk function recommended for the new lumbar spine model (Female: 0 and Male: 1).

Injury risk	Injury criteria	Distribution	β_1	β_2	$coef_{age}$	$coef_{sex}$
Fracture	Strain	Log-normal	-3.1178	-1.0314	-0.0118	0.3045

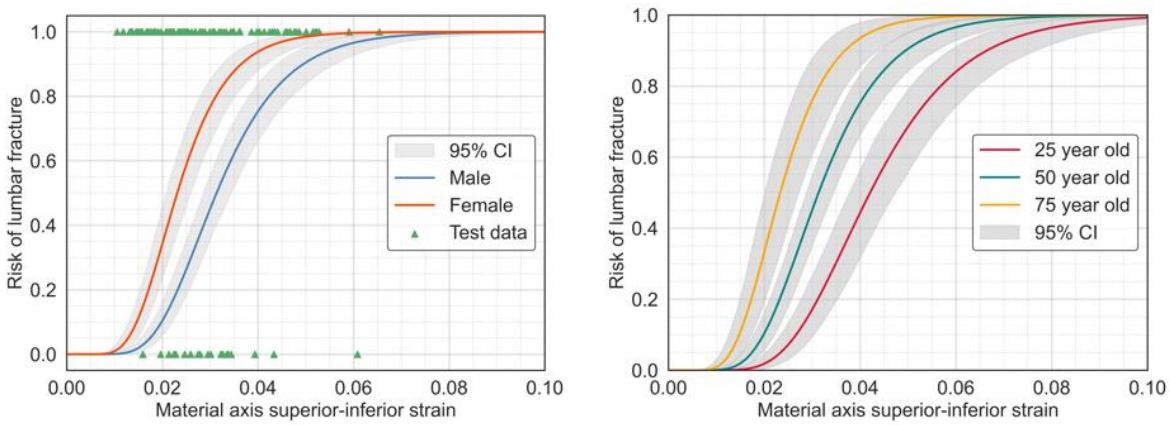

Figure 10: Injury risk curves recommended for use with the new lumbar spine model and for a 50-year-old male and female (left) and for a male 25, 50 and 75 years of age (right).

This project has received funding from the European Union's Horizon 2020 research and innovation programme under Grant Agreement 861570.

Table 3 provides the confidence limits and the quality index that correspond to 5%, 25% and 50% risks of injury from the recommended curves.

Table 3: Injury risk and quality index for risk curves for 50-year-oldamle and female.

Sex	Risk (%)	Mean inferior-superior compressive strain	Confidence limit, lower	Confidence limit, upper	Confidence error	Grade
Male	5	0. 017	0. 016	0. 019	0.22	Good
	25	0. 025	0. 023	0. 027	0.17	Good
	50	0. 031	0. 029	0. 034	0.17	Good
Female	5	0. 013	0. 011	0. 015	0.26	Good
	25	0. 018	0. 016	0. 020	0.22	Good
	50	0. 023	0. 021	0. 026	0.21	Good

2.2.5 Evaluation of the Injury Risk Function

Selected results from the IRF evaluation can be seen in Figure 11. The comparison to the Ortiz-Paparoni risk curve shows that the simulation model somewhat overpredicts the fracture risk (as all the symbols corresponding to simulation results are located to the left of the blue force-based risk curve), with only a few results within the confidence bands. Comparing the three spine curvatures, the pre-extended spine model predicts the lowest risk, and the pre-flexed spine model predicts the highest risk. In all cases the highest strain was in the L1 vertebrae (lower half).

Even though the number of PMHSs was low in the Yoganandan test series, the comparison to the results from the second test series, supported the indications from the first test series, i.e., that the fracture risk based on the newly developed IRF was somewhat over predicted, as the predicted risk was close to 100% in both the tests that led to spine fracture, but even more importantly also above 80% for some tests where fracture did not occur.

This project has received funding from the European Union's Horizon 2020 research and innovation programme under Grant Agreement 861570.

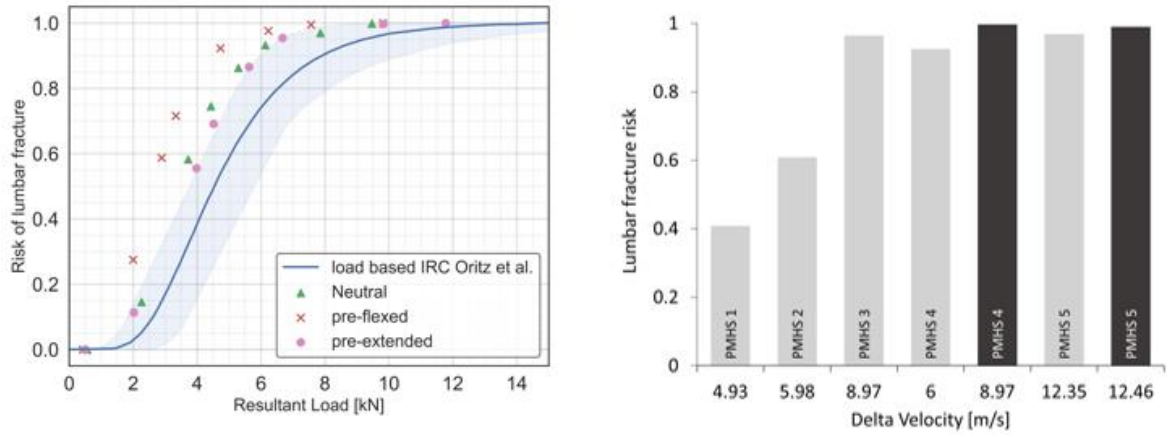

Figure 11: Results from evaluation of IRF. Left according to Ortiz-Paparoni [63], where the blue line represents the force-based injury risk from the PMHS tests (combination of spine curvatures), and the symbols represents the estimated injury risk from the simulation model, for the neutral, pre-flexed and pre-extended spines. Right according to Yoganadan et al. [66], dark grey bars represent the tests where fracture occurred in the lumbar spine. Light grey bars represent tests not leading to spine fracture. Only the most severe tests when there was no injury are displayed.

2.3 Discussion

The current study presents the development and validation of a lumbar spine FE model with an associated IRF for the assessment of lumbar spine compression fractures. The model is primary intended for injury prevention applications in the traffic environment but might also be used for other applications.

The modelling of the disc has been shown to be important for the loading of the end plate and the trabecular bone underneath the endplate [70]. In the current study the annulus was modelled based on published material parameters, whereas the nucleus was tuned to FSU compression and tension test data. While the area of the nucleus was matched to literature sources, it is also important that the load sharing between the nucleus and anulus is correct, as this will contribute to the fracture onset and location. However, no validation data was found to confirm the load sharing between the nucleus and annulus. Further, it has also been shown that the disc is highly strain rate dependent [43], which might also influence the vertebrae fracture onset and location. In the current study neither the annulus nor the nucleus was modelled to include strain rate dependency. Also, material tuning of the nucleus was done based on quasi static (0.005 m/s) to low-speed dynamic (0.1 m/s) tests. Previous studies indicates that the disc stiffness might increase a lot around a loading speed of 1m/s [71]. Therefore, there is a risk the current model is too flexible at loading rates of 1m/s and above.

It was not possible to increase the axial stiffness without at the same time affecting the rotational stiffnesses, and in particular the lateral bending stiffness. As seen in Fig. A 1, the lateral bending stiffness for an FSU without any ligaments (only the disc contributes to the stiffness) is already too high compared to the experimental results, and this too high stiffness is carried all the way to the intact FSU in Fig. A 8. It should however be noted that the

This project has received funding from the European Union's Horizon 2020 research and innovation programme under Grant Agreement 861570.

physical rotational stiffness tests used for ligament tuning were performed at low loading speeds (1-2.8°/s), and thus, for a higher speed in line with a 1 m/s axial compression test, the rotational stiffness might be significantly higher.

In the IRF evaluation phase it was noticed that L1 interacted with the rigid T12 (from the original VIVA+ model) in an unphysical way. Shortly, as T12 could not deform as a result of the increased pressure in the disc during loading, L1 showed additional, unphysical deformations, and too high strain levels. It is thus recommended for future studies to model also T12 in detail if all vertebrae of the lumbar spine should be included in the calculation of injury risk. In the current study, the solution was to remove the superior half of L1 from the injury risk calculations.

The parameter “LUMB_FLEX” was introduced to account for ligament initial slack or pre-stretch, that depends on the curvature of the spine. If this effect would be disregarded the stiffness in flexion will be much too high. This was also noted for the Chazal ligament data (used for the current model), in a study comparing the influence of ligament mechanical properties [72]. In the tuning, all ligaments posterior of the joint centre of rotation (approximately at the rear 1/3 of the disc) got a positive offset (initial slack) in the tuning phase, while the ALL ligament got a negative offset (initial pre-stretch). The further away from the rotation centre the larger the offset, with the largest offset (+5 mm) for the ISL and SSL ligaments. Thus, it was hypothesized (as it was not reported) that the FSUs in the physical tests used for ligament initial length tuning was in a lordotic posture, slacking the posterior ligaments. Flexing the spine from this position will gradually remove the initial slack. In [56,58] the authors reports an average change in lumbar flexion of about 8° per motion segment, when transitioning from standing to sitting (in a vehicle seat). This rotation roughly matches the removal of the initial slack, and thus it is recommended to use LUMB_FLEX=-1 for a standing posture, and LUMB_FLEX=0 for a seated posture.

One limitation in the ligament tuning and validation of the lumbar spine FE model is that the rotational tests could only be compared up to 10Nm (maximum load in physical experiments), which is very low compared to flexion moments at fracture ranging up 300+ Nm [63]. It should be noted that the Demetropoulos [55] test series included rotational test up to failure, in flexion, extension, and lateral bending, in addition to the translational loads used for the validation in this study. While the stiffness in flexion reported by Demetropoulos matched the Yamamoto [54] results, the reported stiffnesses in extension and lateral bending were much higher. However, by comparing Demetropoulos extension and lateral bending results to the lumbar spine physical range of motion (RoM) [73] it was concluded that the stiffness curves were unrealistic (about 150Nm would be required to reach the RoM), at least for a neutral spine curvature, and thus these tests were not used for model validation. It was hypothesized that the lumbar spines tests in [55] might have started from a highly lordotic curvature, which could potentially explain the difference in results compared to other studies.

The quality of the data used in the construction of the IRF were deemed fair. The age was distributed evenly between the two sexes in the dataset and, e.g., the securing or the vertebrae bodies to the loading devices and the loading conditions were well described and could be modelled with fair accuracy. However, data was lacking that allowed for

This project has received funding from the European Union’s Horizon 2020 research and innovation programme under Grant Agreement 861570.

scaling/morphing the model of the FSU to the exact dimensions of the tested FSUs. In addition, information on the initial lordosis of the unloaded FSU was partially lacking.

Sex and age were the only significant parameters affecting the prediction of the inferior-superior compressive strains. These were also the covariates that provided the best IRF according to the Cox analysis. These results indicate that there may be differences in the mechanical properties of the trabecular bone between males and females. However, these results may be confounded by a size effect not captured correctly as the model could not be morphed to the exact geometry of the tested FSUs. This needs to be further addressed in future studies.

All left censored data that potentially could have been included in the development of the IRF in this study were dropped, as the number of cases with exact data was deemed sufficient.

Several types of lumbar vertebrae body compression fractures occur in vehicle crashes, including wedge fractures, burst fractures and biconcave fractures. Several studies have investigated the mechanisms of lumbar spine fractures, and many have found evidence that fracture initiates from the endplate [74][75]. Endplate injuries may well occur in the vehicle crashes, although not sufficiently detailed in vehicle crash databases, and may precede the fractures of the trabecular and cortical bones. The injury metric chosen for the IRF presented in this study was the compressive strain in the local vertebrae superior-inferior direction, measured in the solid elements representing the trabecular bone of the vertebrae body. Other metrics, such as effective plastic strain or 1st principal strain in the cortical bone or the endplates, were considered but were discarded as they could not separate between compressive and tensile loading, while the IRF should only predict risk for compression fractures. The choice of evaluating the superior-inferior strain in the trabecular bone, instead of for example the endplates, was due to several reasons. First, as the endplates were modelled using shell elements, the out of plane stresses (corresponding to the superior-inferior direction) are by element design not computed. Secondly, tests on lumbar spine segments were undertaken with the aim to measure the change in pressure in the trabecular bone during a burst fracture [74][75] and reported an increase in internal pressure in the vertebrae after an onset of endplate failure. In the current study, it was hypothesized that fracture of the end plate occurs at about the same time as in the underlying trabecular bone (supporting the endplates), and thus the fracture in the trabecular bone could be used as a proxy for end plate fractures. Similarly, it can be hypothesized that inferior-superior compressive strain in the trabecular bone of the vertebrae body can also be a fair proxy for the wedge and burst fractures in the lumbar spine.

Another limitation was that the IRF evaluation indicated that the model together with the associated IRF together overpredicted the injury risk. There could be many reasons for this, from improper model deformation at high loads, or improper load distribution in the disc (discussed in previous paragraphs), to unknown boundary condition that effected the simulations of the FSU tests used to develop the IRF. It should also be noted that the integrated lumbar spine model lacks potentially important structures, like muscle attachments, that could reduce the risk of buckling when subjected to axial loading. Adding these structures could potentially reduce the predicted injury risks in the full body evaluation

This project has received funding from the European Union's Horizon 2020 research and innovation programme under Grant Agreement 861570.

load cases. To address some of these limitations, future validation should preferably include additional tests with combined loading at higher loads, and higher loading speeds [62]. However, in the study by Yoganandan et al. [64] it was discussed that full body x-rays do not conclusively document/identify all possible fractures. Based on this it is fair to believe that there could have been minor fractures in the lumbar spine in some of the cases reported to be unfractured. Hence, the evaluation of the IRF carried out in this study is deemed to be inclusive, and it is judged that the current model together with the associated IRF can be used to estimate the risk for compressive fractures in the lumbar spine, with the knowledge that these estimates might be somewhat conservative.

The lumbar spine model, presented in this study, was integrated into the VIVA+ HBMs which can be downloaded at openvt.org [76].

2.4 Conclusions

A new open-source finite element lumbar spine model was developed and validated together with an associated tissue-based injury risk function. A parameter was introduced assigning ligament slack/pre-stretch based on initial spine curvature. The model was shown to predict kinematic and kinetic reasonable, with best performance for axial compression and flexion. The tissue-based injury risk function, based on reconstructions of 119 FSU tests, showed good statistical properties. The evaluation of the injury risk function indicated that the fracture risk was somewhat overpredicted. Despite this it is judged that the current model together with the associated IRF can be used to estimate the risk for compressive fractures in the lumbar spine.

This project has received funding from the European Union's Horizon 2020 research and innovation programme under Grant Agreement 861570.

3. Development of a pelvis model

In this study the finite element pelvis model, originally generated in the VIRTUAL EU project, was enhanced, tuned and validated. The model was also morphed to the anthropometries of an average male and average female and integrated into the open-source VIVA+ HBMs, made available at openvt.eu.

3.1 Methods

The FE pelvis model, modelled using pure hexahedral solid and quadrilateral shell elements, to enable injury estimation based on element strains, was originally created based on averaged data from computer tomography images (CT) [77] data in the VIRTUAL EU project. In the current project the cortical bone thickness was updated from a uniform thickness to a thickness varying continuous over the pelvis, using published data. In addition, the properties of the sacroiliac and pubic symphysis joints were re-tuned based on published data. Next, the kinetic and kinematic response of the pelvis model was validated in lateral loading, using published biomechanical data.

All simulations were carried out using LS-DYNA MPP R11.1.0 (ANSYS/LST, Livermore, CA). Meshing and other pre-processing were done using ANSA (Beta CAE Systems, Luzern, Switzerland), post-processing using LS-PREPOST (ANSYS/LST, Livermore, CA) and Hypergraph (Altair, Troy, MI).

3.1.1 Development of a morphable pelvis model

A pelvis FE-model, based on the average of 132 (75 female and 57 male) data sets from CT scans of the pelvis (University of Michigan Department of Radiology, USA) was originally created in the VIRTUAL EU project. The geometry was based on a morphometric statistical model, with sex, age, stature, and BMI as co-variates, with the shape variance analysed using sparse PCA [77]. This statistical model was used to morph the base model into average sized male (height = 175 cm, and weight = 77 kg) and an average sized female (height = 162 cm, and weight = 62 kg) pelvises, see Figure 12.

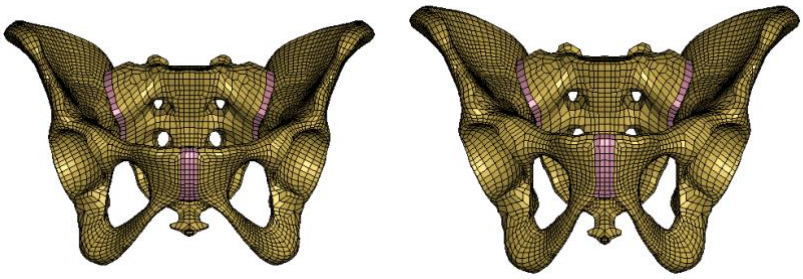

Figure 12: FE pelvis models used in this study (left 50F and right 50M).

This project has received funding from the European Union's Horizon 2020 research and innovation programme under Grant Agreement 861570.

The thickness of innominate cortical bone was based on the average of 10 subjects (5 females and 5 males) [78]. As the sample size was small no attempt was done to create separate thicknesses for the female and male models. For sacrum no information was available, and thus a uniform thickness of 1 mm was assumed. The thicknesses, ranging from 0.7 mm to 4.8 mm, mapped onto the FE mesh, can be seen in Figure 13.

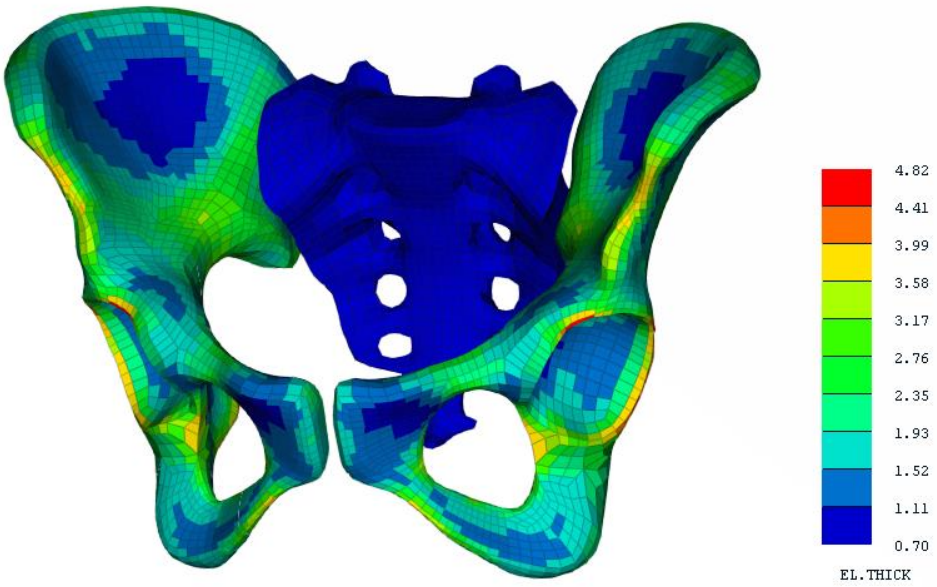

Figure 13: Distribution of the cortical bone thickness shown for the 50F model (the 50M model have the same thickness distribution).

The cortical bone was modelled using fully integrated shell elements (LS-DYNA type 16), using an isotropic material model (LS-DYNA MAT124) with material parameters estimated based on pelvis coupon tests [79]. Young's modulus was set to 10.8 GPa, the density to 2.0 kg/m^3, the yield stress to 59.4 MPa and using a non-linear hardening up to 126.9 MPa at 4.6% plastic strain. The trabecula bone was modelled using reduced order solid elements (LS-DYNA type 1) using an isotropic material model (LS-DYNA MAT24) with material parameters estimated based on [80]. Young's modulus was set to 0.024 GPa, the density to 0.35 kg/m3, and the yield stress to 1Gpa. No strain hardening was defined after yield. No material failure/element erosion was defined for either the cortical or trabecular bone.

The pubic symphysis joint was modelled using four layers of reduced integration solid elements, nodally connected to each innominate bone, see Figure 12. A hyper elastic material model, (LS-DYNA MAT77), with material parameters tuned to match the response of isolated pubic symphysis joints in tension and compression [81], was used. The tuning, further presented below, resulted in two Ogden terms, μ_1=-3.66e^{-5} GPa, α_1=-16, μ_2=1.25e^{-5} GPa, α_1=28.2, together with a Poisson ratio of 0.495 and a density of 1.2 kg/m^3.

The Sacroiliac joint was modelled with one layer of reduced order solid elements, nodally connected to the Sacrum, and connected to the innominate bones using a tied contact, see Figure 12. A hyper elastic material model, (LS-DYNA MAT77), with material parameters tuned to match the response of the sacroiliac joint in shear and rotation [82], was used. The

This project has received funding from the European Union's Horizon 2020 research and innovation programme under Grant Agreement 861570.

tuning, further presented below, resulted in one Ogden term, μ_1=0.00345 GPa, α_1=2, together with a Poisson ratio of 0.495 and a density of 1.2 kg/m^3.

3.1.2 Tuning of joint properties

The properties of the Pubic Symphysis joint were tuned to match the experiments performed by [83] with additional details published in [84]. The test series included 20 subjects of mixed sex with an average age of 66 years. In this tuning phase the response in both tensile and compressive loading was considered. The Pubic Symphysis together with part of the innominate bone on each side was constrained in a deformable potting material modelled using a linear elastic material model (LD-DYNA MAT1), with Young's modulus set to 2.85 GPa, and the density to 1.2 kg/m^3. The constraint, holding the innominate bone in the potting, was modelled using LS-DYNA CONSTRAINED_SHELL_IN_SOLID_PENALTY. The upper potting was moved at a constant speed of 1 mm/s (after a ramp up during the first 10 ms to reduce dynamic effects) up to the peak displacement of 0.8 mm. The stiffness (force versus deflection) was evaluated similarly to Dakin between 0-10% deformation (called toe region), and between 80-90% deformation (called linear region).

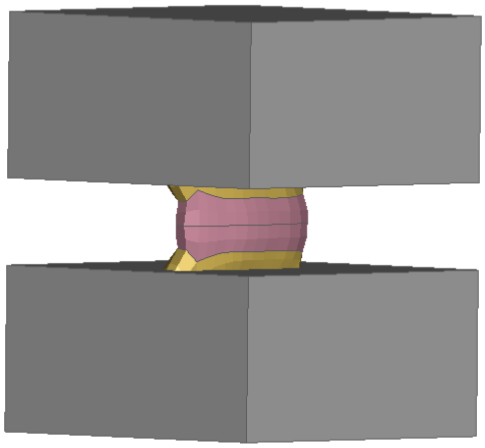

Figure 14. Test set-up according to (Dakin 2001) used in the tuning of the pubic symphysis joint.

The properties of the Sacro Iliac joint were tuned to match the experiments performed by [82]. The test series contained specimens from 7 males and 1 female, with an average age of 66 years. The linear stiffness in superior, inferior, anterior, posterior, and medial loading directions, as well as the rotational stiffness in flexion, extension, lateral bending as well as torsion, was simulated and compared to experimental results. Similar to the first tuning load case, the bones on each side of the joint were constrained in a deformable potting material, modelled using a linear elastic material model (LD-DYNA MAT1), with Young's modulus set to 2.2 GPa, and the density to 2 kg/m^3. The constraint, holding the innominate bone in the potting, was modelled using LS-DYNA CONSTRAINED_SHELL_IN_SOLID_PENALTY. For

This project has received funding from the European Union's Horizon 2020 research and innovation programme under Grant Agreement 861570.

the linear load cases, a force was applied at the centre of the sacrum body. The force was ramped up during 100 ms and then held at a constant level of 294 N. This is faster than in the original experiments, but the simulations were checked to not have any significant inertia effects, motivating this higher loading speed. For the rotational load cases a moment load of 42 Nm was applied similarly as for the linear load cases. The output, compared to the physical experiments, were the displacements or the rotations at peak load.

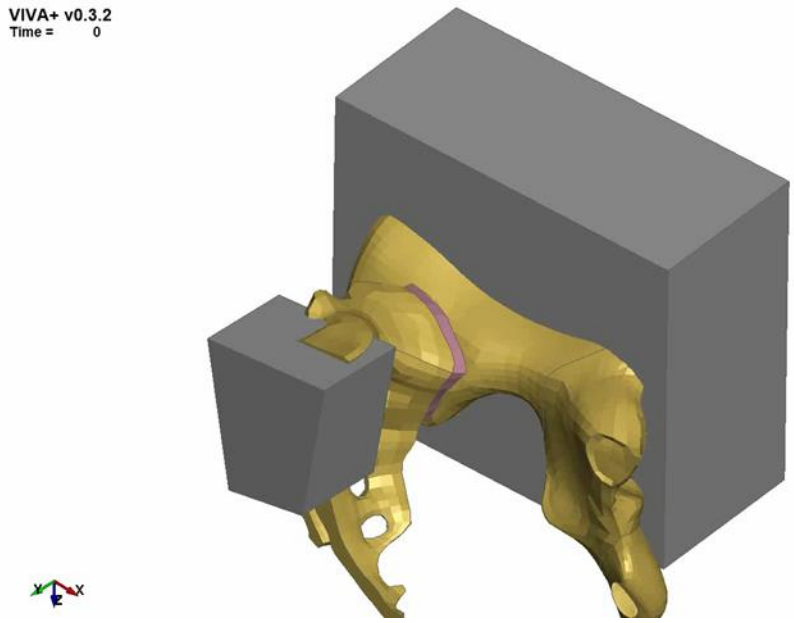

Figure 15: Test set-up according to (Miller 1987) used in the tuning of the sacroiliac joints.

3.1.3 Validation of the new pelvis model

Reference [85] carried out quasi-static and dynamic lateral loading experiments on denuded pelvic bones. The test series included pelvic bones from 10 subjects (9 males, 1 female). For the static load cases a load was applied at a constant speed of 5 mm/min using either a plate pressing on the iliac crest or a metallic ball pressing on the acetabulum. In addition, pelvic bones of 12 other subjects (6 males, 6 females) were dynamically loaded by dropping a weight (mass 3.68 kg, v=4 m/s) on the metallic ball inside acetabulum, via an 11 mm silicon padding.

To simulate the experimental scenario, the pelvis model was oriented on its side and constrained in a box filled with solid hexahedral elements, see Figure 16. The solid elements representing the potting were modelled using an elastic material model (LS-DYNA MAT1) with Young's modulus of 12.7 GPa, density of 0.94 kg/m^3, an yield stress of 26.2 MPa and using non-linear hardening according to [86]. The impact plane and the ball were considered fully rigid. The silicon padding was modelled using a hyper elastic material model (LS-DYNA MAT77), with one Ogden term (μ_1=0.0002 GPa, α_1=3), a poisons ratio of 0.499, and a density of 2 kg/m^3, according to specifications for B452 silicon at strain rate 40 s^{-1} in [87].

This project has received funding from the European Union's Horizon 2020 research and innovation programme under Grant Agreement 861570.

The predicted force deflection curves were compared to the results from the physical tests. In the physical test series only two subjects were uninjured after testing. As the model do not model injury including progressive fracture, the best comparison is to these two tests.

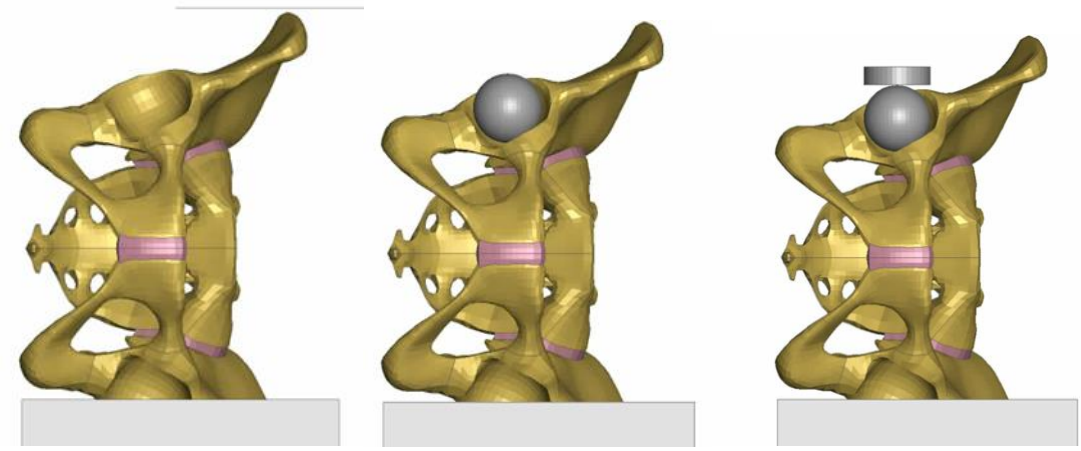

Figure 16: Test set-up according to (Guillemot 1998) used in the validation of the pelvis model.

3.1.4 Positioning and integration into the VIVA+ model

After integration into the VIVA+ HBMs, the rotation of the pelvis was evaluated based on literature data. The Pelvis Tilt (PT) was compared to [67], and the Pelvis Angle (PA) and Sacral Slope (SS) to [68]. Both studies are based on volunteers seated in a vehicle seat.

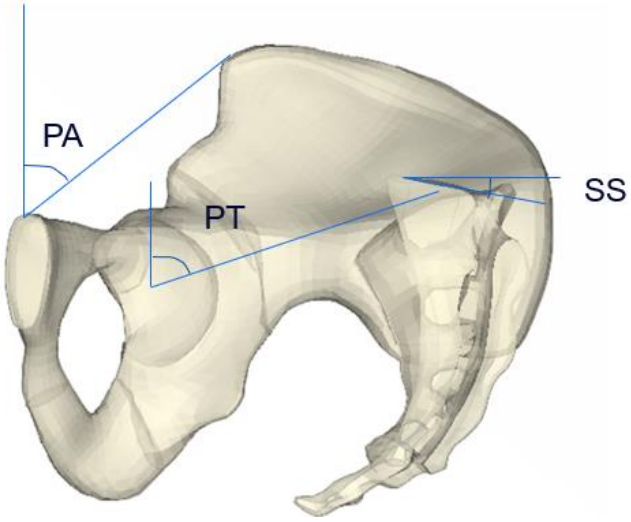

Figure 17. Orientation of pelvis, PA=Pelvis Angle, PT= Pelvis Tilt, SS= Sacral Slope

Further, the position of the pelvis within the hip was evaluated to literature data. [88] and [89] reported the ASIS flesh margin (A-F) defined according to Figure 18 and the ASIS to thigh distance (A-T) in Figure 18, for occupants of different recline angles. The models were evaluated against the predicted distances for the corresponding BMI levels (23-25).

This project has received funding from the European Union's Horizon 2020 research and innovation programme under Grant Agreement 861570.

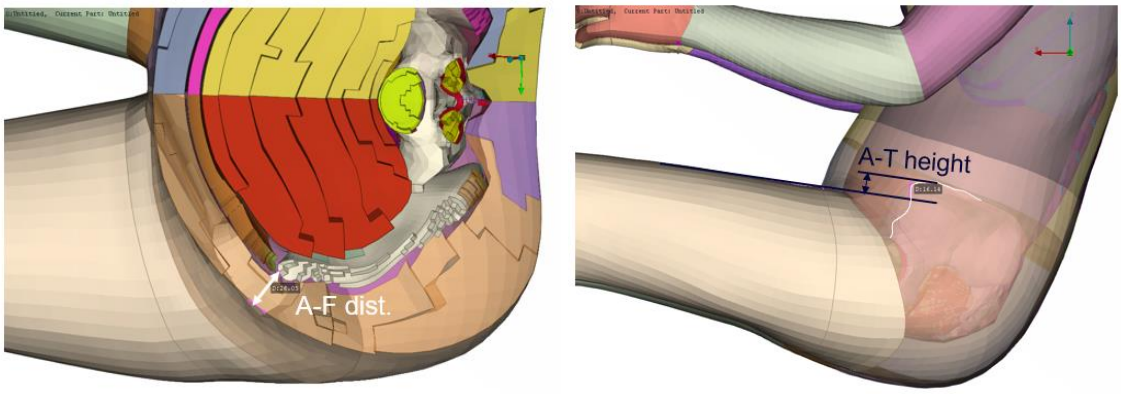

Figure 18. Positioning of the pelvis inside the hip. A-F distance is the distance form the ASIS to the skin surface, and AT height is the vertical distance from ASIS to a line extended from the leg upper surface.

3.2 Results

3.2.1 Development of a new pelvis model

The pelvis model including the joints consists of about 8 400 shell elements and 23 600 solid elements. All elements for both models fulfils the element quality criteria defined in [90].

3.2.2 Tuning of joint properties

In Figure 19 the predicted pubic symphysis toe and linear stiffnesses are compared to the experiments by [83], for both the male and the female pelvis models. In both loading directions and for both models the predicted responses are within one standard deviation of the test results (indicated by the lines). The full force deformation plots can be seen and compared to results presented in [84]in Figure 20.

This project has received funding from the European Union's Horizon 2020 research and innovation programme under Grant Agreement 861570.

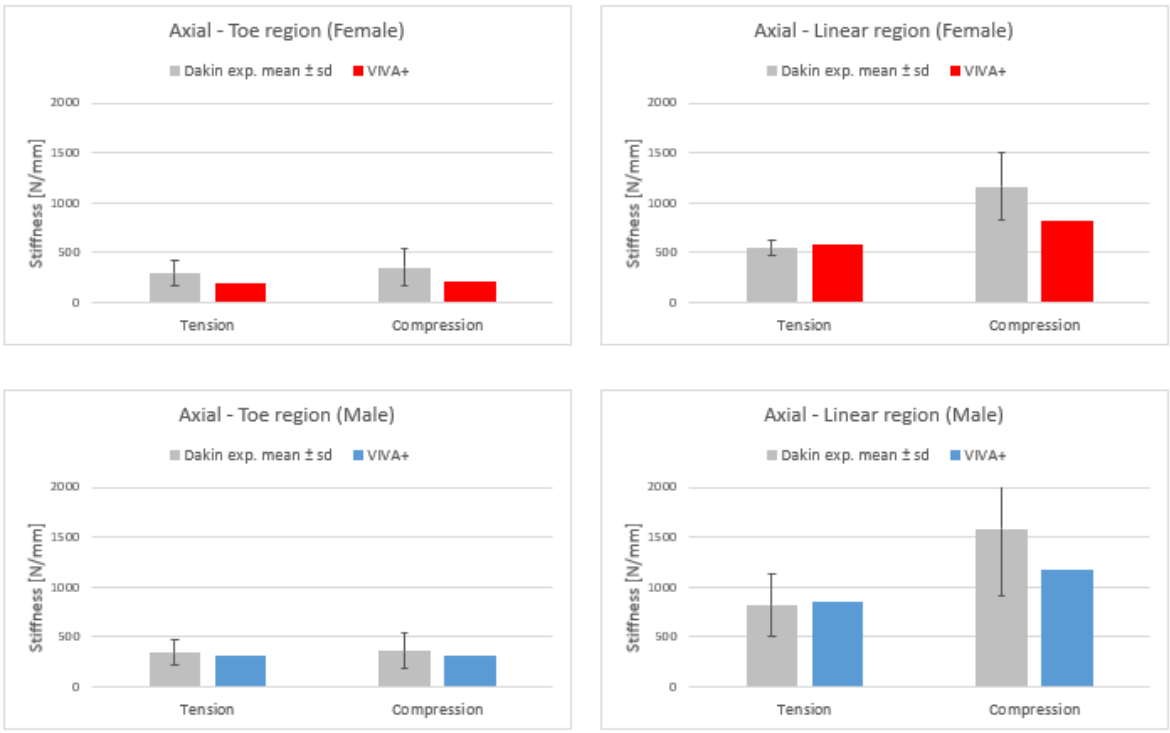

Figure 19. Tuning of the Pubic Symphysis joint properties in tension and compression.

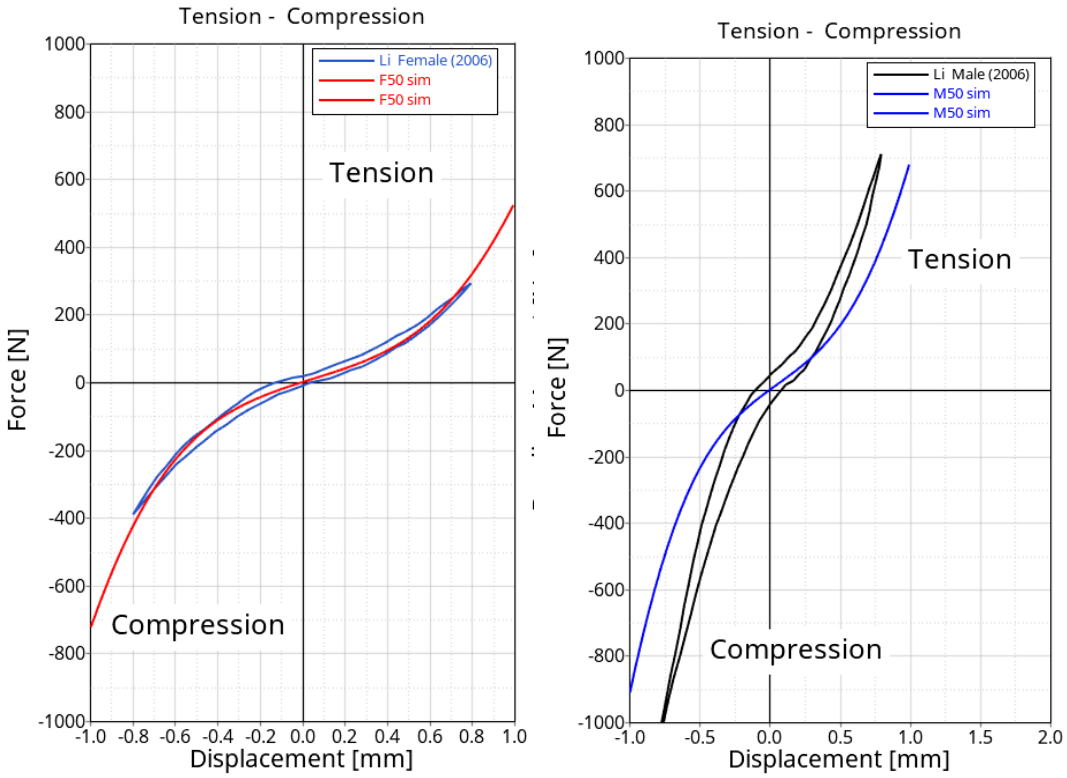

Figure 20. Force deformation plots comparing the predicted response to responses presented in Li (2006)

This project has received funding from the European Union's Horizon 2020 research and innovation programme under Grant Agreement 861570.

The results from the tuning of the sacroiliac joint properties can be seen in Figure 21. As the physical test series contained seven males and only one female, only the male results (blue bars) can accurately be compared to physical test results. The predicted stiffness for the male model matched the test results within one standard deviation for all load cases except anterior loading (where the model predicts a slightly too high stiffness) and for flexion moment loading (where the model predicts a slightly too low stiffness). The female model predicts a lower stiffness in all load cases, consistent with the results from the tuning of the pubic symphysis joint.

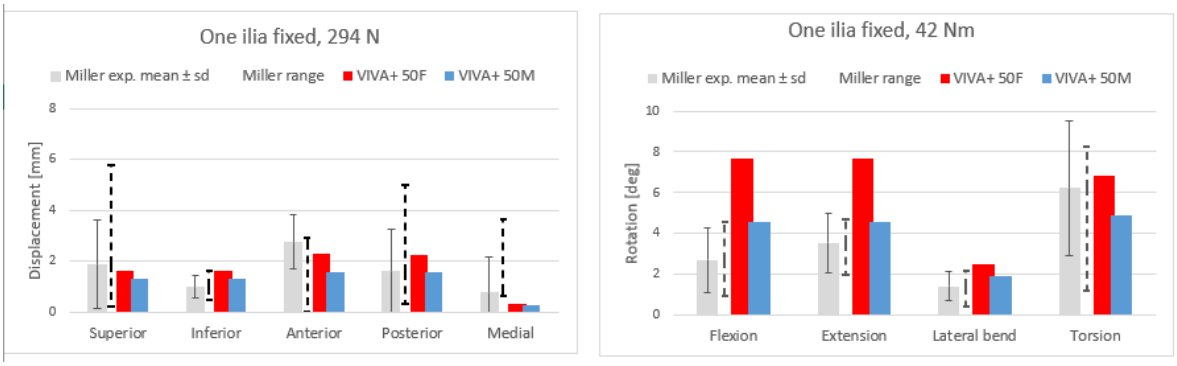

Figure 21: Tuning results for the Sacroiliac joint properties in tension and shear and bending.

3.2.3 Validation of the new pelvis model

The pelvis model prediction is compared to the results from the physical experiments for the static iliac crest load case in Figure 22. The predicted response for both the male and female pelvises are within one standard deviation of the physical test results. However, it should be noted that nine out of ten subjects were male in this part of the study, meaning that only the predicted response of the 50M model makes a proper comparison.

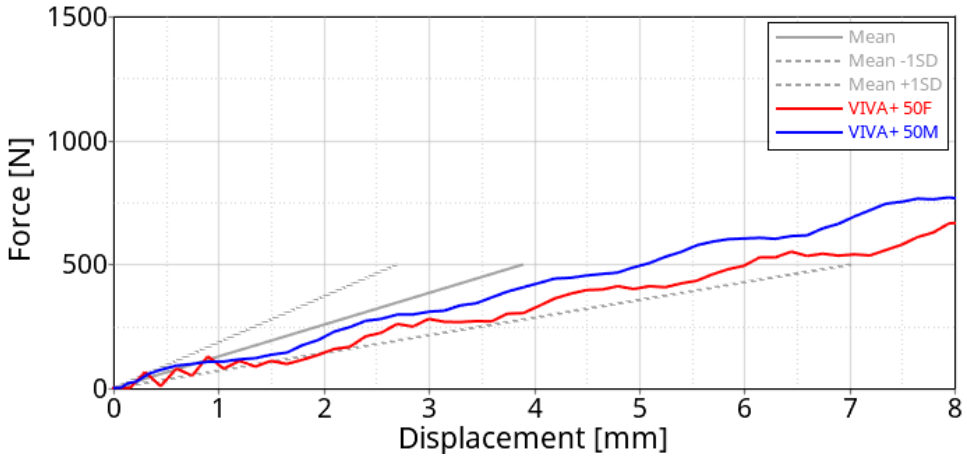

Figure 22. Comparison of pelvis predictions to physical test results in Guillemot static Iliac crest loading test.

This project has received funding from the European Union's Horizon 2020 research and innovation programme under Grant Agreement 861570.

Next, the pelvis model predictions are compared to the results from the physical experiments for the static acetabulum load case in Figure 23. The predicted response for the female pelvis is within one standard deviation of the physical test results, while the prediction for the male pelvis model is outside, on the stiffer side. Also, for this sub study, nine out of ten subjects were male.

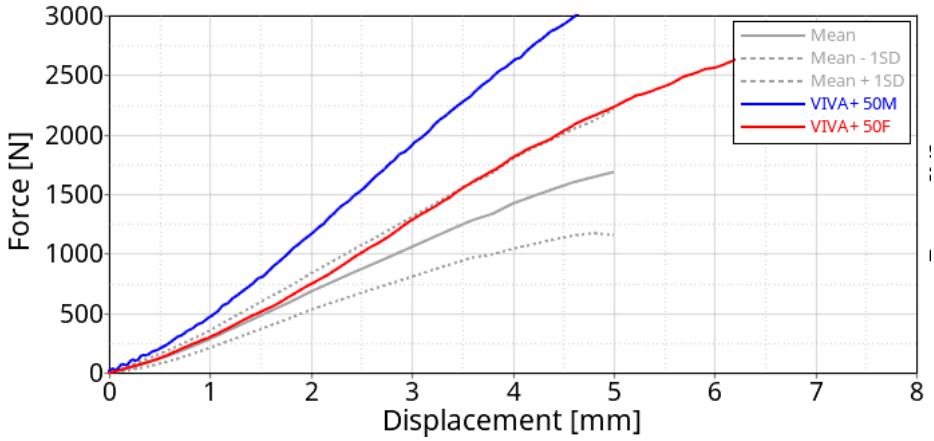

Figure 23. Comparison of pelvis predictions to physical test results in Guillemot static acetabulum loading test.

In Figure 24 the model predictions are compared to the physical test results for the dynamic acetabulum load case. The right subfigure shows that the predicted peak deformation and force for the female pelvis is close to the results from the uninjured female subjects, while the predicted response for the male pelvis is in-between the uninjured male and female subjects. The left subfigure shows that the predictions lag somewhat behind in the loading phase, and stays longer at a high force level, due to a second peak, not visible in the experimental corridors.

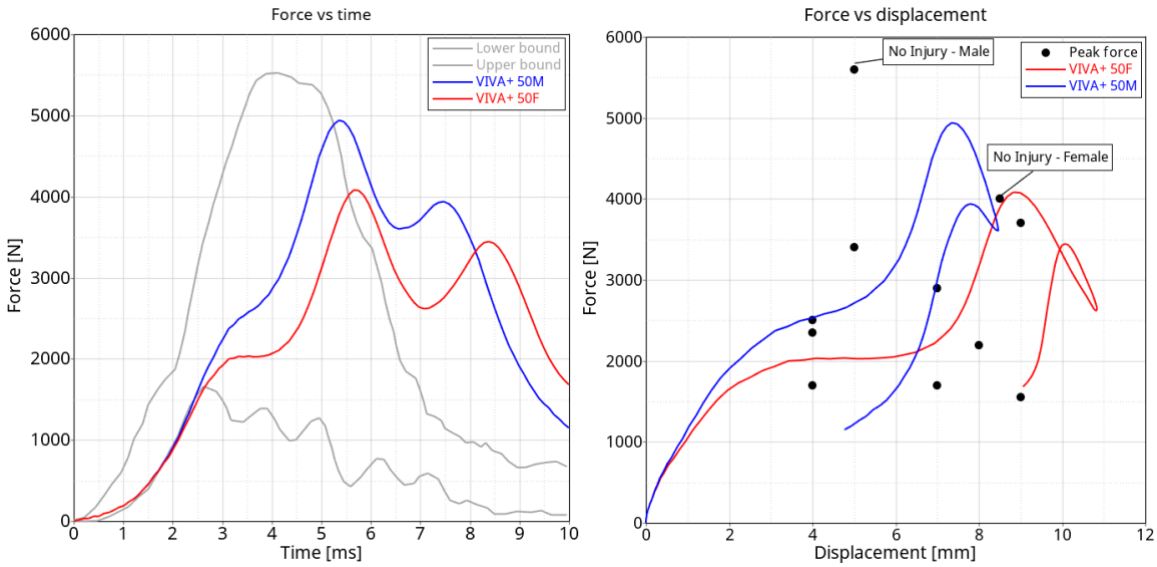

Figure 24: Comparison of pelvis predictions to physical test results in Guillemot dynamic acetabulum loading test.

This project has received funding from the European Union's Horizon 2020 research and innovation programme under Grant Agreement 861570.

3.2.4 Positioning and integration into the VIVA+ model

The PT for seated volunteers (mixed sex) is according to [67] 65°±8°. The 50F model have a PT of 67.5°, and the 50M model 64.9°. The PA and SS according to [68] are 43 to 48° and -13 to -21°, depending on degree of kyphosis. The 50F model have a PA of 51.7° and a SS of -14.5°, while the 50M model have a PA of 53.5° and SS of -11.9°.

The A-F distance is between 20 and 30 mm for seated volunteers with and BMI around 25 according to [88], roughly similar for males and female. The 50F model have an A-F distance of 26 mm, and the 50M model 29 mm. The A-T distance is roughly between 10 and 20 mm for females and -5 to 15 mm for males with an BMI around 25 according to Tanaka 2021), whereas [89] reports A-T distances around 10-30 mm for males with a BMI of 25. The 50F model have an A-T distance of 16 mm and the 50M model 19 mm.

3.3 Discussion

In this study the VIVA+ pelvis model was updated to include variable cortical thickness, and the pubic symphysis and sacroiliac joints were re-tuned to literature data. The pelvis was morphed to an average sized female and an average sized male. Both these pelvis models were then validated, with respect to kinematic and kinetics, to lateral impacts.

The pelvis model shares the base geometry and morphing with the pelvis in the SAFER-HBM, which have been presented in [77]. According to a follow up study [78] pelvis shape, the material properties of the cortical bone, and the thickness of the cortical bone, are all important parameters affecting the stiffness in lateral loading.

The current pelvis shape is based on a regression model based on 132 CT scans (from 75 males and 57 females) and should give a stable prediction of the average size and outer shape of the pelvises in the subpopulation of that study. It is not known if it represents also other populations, including the pelvises used in the validation of the current study. What can be compared is the volume of the models to the volumes of the pelvises in the dynamic validation test series. The volumes of the pelvises models are 788 cm^3 (50F) and 1030 cm^3 (50M), which can be compared to the average volumes reported in the experiment, 948 cm^3 (female) and 1178 cm^3 (male). Based on this information the experimental pelvises were on average larger than the models. However, it is not clear how well the experimental pelvises were cleaned of soft tissues, which could affect the volume measurements.

The material data for the cortical bone is based on tensile testing of 20 samples from just four subjects [91]. The test samples were extracted from different sites and at different angles. Previous studies (on other body parts) have shown that cortical bone have very different mechanical properties along and across the osteon direction [92]. However, as the osteon directions of the tested pelvises used for the current study were unknown, it was hard to estimate if the samples represent across or along osteon direction, or a mix of these. In addition, other studies (on other body parts) have also shown that tensile and compressive mechanical properties for cortical bone differs [93] and [94], with typically significant higher yield stress in compression. However, as only tensile tests were available for the pelvis model, it was assumed that the tensile and compressive mechanical properties are

This project has received funding from the European Union's Horizon 2020 research and innovation programme under Grant Agreement 861570.

symmetric, and the same material curve was used in both loading directions. This might underestimate the yield stress in compression, and thus the stress and strain distributions after the pelvis have reached loads leading to permanent deformations might be inaccurate.

The cortical thickness distribution for the innominate bones was mapped from the average thickness of a sample of 10 (5F and 5M) subjects. As the sample size was quite small, no attempt was made to separate the cortical female thickness distribution from male, although this data indicates that females might have a thinner cortex on average. In addition, by using averaged data instead of for example using the “most average” individual, there is a risk that local thickness features are smooth out, as the position of these might vary over the surface from individual to individual. However, due to the small sample size, it was judged that the average thickness of all subjects would be a better approximation than the “most average” subject, as input to the model.

The validation of the kinetics and kinematics for the static load cases showed that the model predictions were within one standard deviation of the average of the experimental response, except for the male model when loaded through the acetabulum. In this load case, the predicted pelvis deformation for a load of 2 kN was about 1.5 mm outside the upper experimental corridor. For the dynamic acetabulum load case the peak deformation as well as peak force matched the two uninjured pelvises well. The predicted female peak force predicted the uninjured female pelvis very closely, while the predicted male peak force was in between the uninjured female and male responses. However, even though the force response was within the experimental corridor during the loading phase, the model seems to have a time lag compared to the experimental setup. Most likely the reason is that the initial position and interaction between the metal sphere and the acetabulum is not correctly modelled. One possible explanation is the model lacks the lunate surface cartilage. Studies have shown that this cartilage have a thickness of 1.7-2.7 mm [95]. The lack of this tissue could possibly also explain some of the stiff behaviour seen in the static acetabulum load case.

The pelvis rotation evaluation after integration into the 50F and 50M VIVA+ models showed that the pelvis tilt for both models were within the volunteer range, while the pelvic angle and sacral slope were a few degrees outside reported ranges. However, all these measurements are related, meaning that it is not possible to match all three. The flesh thickness (A-F) in front of the ASIS as well as the vertical distance from the thigh upper edge to ASIS (A-T) matched the reported range for the 50F model. For the 50M model the A-F distance matched the reported range, while the A-T distance matched one study (Mizuno 2018). It should be noted that the volunteers in [89] and [88] were in an upright sitting posture, while the model represent a slightly reclined vehicle occupants posture corresponding to a seta back angle of about 23°. This might affect the flesh thicknesses. However, overall it was judged that the pelvises are positioned and rotated reasonably inside the VIVA+ models, compared to volunteers.

This project has received funding from the European Union’s Horizon 2020 research and innovation programme under Grant Agreement 861570.

3.4 Conclusions

The pelvis model in the VIVA+ HBMs have been updated, retuned, and validated for lateral loading. The predicted kinematics and kinetics for the two joints matched physical test results after tuning. The validation showed that the static stiffness model predictions match the physical results within one standard deviation when loaded through the iliac crest, while the model predictions is on the stiff side when loaded at through acetabulum. The validation to dynamic acetabulum loading showed that the kinematic and kinetic response is similar to pelvises that do not fracture during the test.

This project has received funding from the European Union's Horizon 2020 research and innovation programme under Grant Agreement 861570.

4. Volunteer study

Occupant motion in the pre-crash phase provides valuable information for the design of safety devices and offers a basis for the development of a simulation controller for active human body models.

The performed volunteer tests took place on a closed test track (ÖAMTC test site Lebring, Austria) over a period of six days in May 2022. Figure 25 shows the test site and illustrates the approximate sequence of the tests. The weather conditions were constant over the period and a high reproduction quality was achieved.

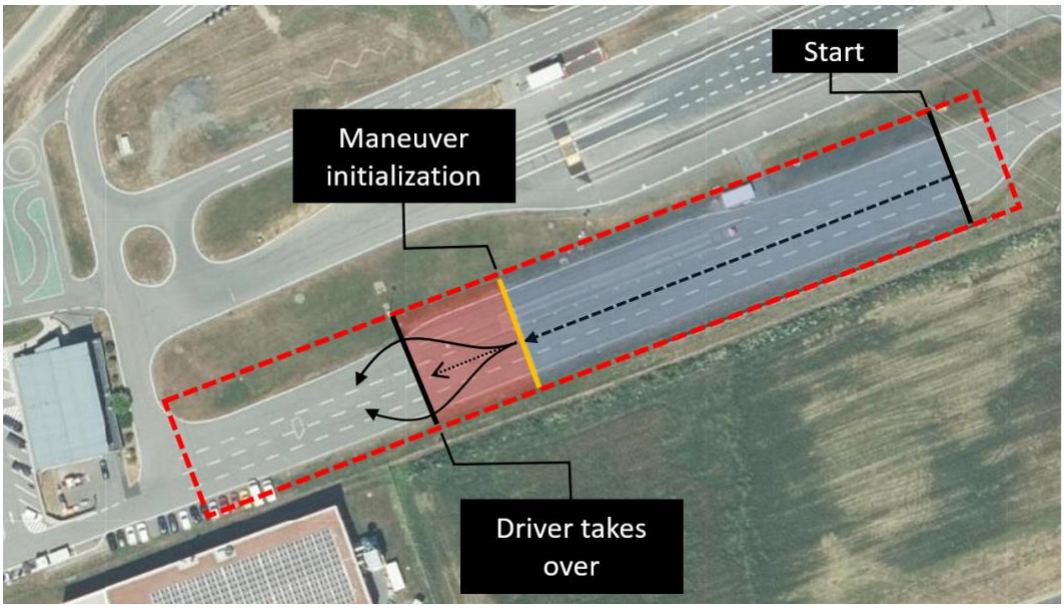

Figure 25: Test site with schematic sequence

Three manoeuvres with different speeds and seating positions were completed. The volunteer study includes 12 women and 27 men. The individual factors are discussed in more detail in the following chapters.

4.1 Test vehicle and performed manoeuvres

A 2017 Ford Mondeo was used as the test vehicle. Through extended functionalities, provided by Dataspeed Inc. as a drive-by-wire kit, GPS trajectories were recorded and tracked. Combined with the developed fault injection method – invented for test driver training – it was possible to create reproducible, highly dynamic driving maneuvers. [96]

This project has received funding from the European Union's Horizon 2020 research and innovation programme under Grant Agreement 861570.

Figure 26: Ford Mondeo - Virtual Vehicle Research GmbH

To be able to include the vehicle kinematics in the evaluation, the following CAN-BUS data was stored for all manoeuvres:

- Longitudinal acceleration
- Lateral acceleration
- Vertical acceleration

To have the best possible interaction with the belt system in a strongly reclined seating position, a seat (front right passenger seat of Ford B-max 2014) with an integrated belt system was installed.

Eleven manoeuvres were performed and recorded with each of the 37 volunteers. The following table gives an overview of the individual manoeuvres, in the order they were performed. As the manoeuvres prior to a crash event are in 40-50% [97] of the cases braking and steering manoeuvres, those were selected to be tested in this study.

Table 4: Manoeuvre overview for each volunteer

#	Event	Speed [km/h]	Backrest angle [°]	Status
1	Left turn	50	48	unaware
2	Right turn	50	48	unaware
3	Breaking	50	48	unaware
4	Left turn	50	48	aware
5	Right turn	50	48	aware
6	Breaking	50	48	aware
7	Breaking	30	48	aware
8	Breaking	30	24	aware
9	Left turn	50	24	aware
10	Right turn	50	24	aware
11	Breaking	50	24	aware

This project has received funding from the European Union's Horizon 2020 research and innovation programme under Grant Agreement 861570.

The angle of the backrest is measured in relation to the plumb line. “Unaware" refers to manoeuvres in which the subject knows neither the time nor the event. In contrast, "aware" describes that the volunteers know when and which event will be performed.

4.2 Volunteer characteristics

When selecting volunteers, care has been taken to ensure that their proportions are within the desired range (females: 155 -170 cm, 55- 80 kg, males: 170 – 185 cm, 60 – 90 kg) The distribution of height, weight, and age for the 12 women and 27 men is shown below.

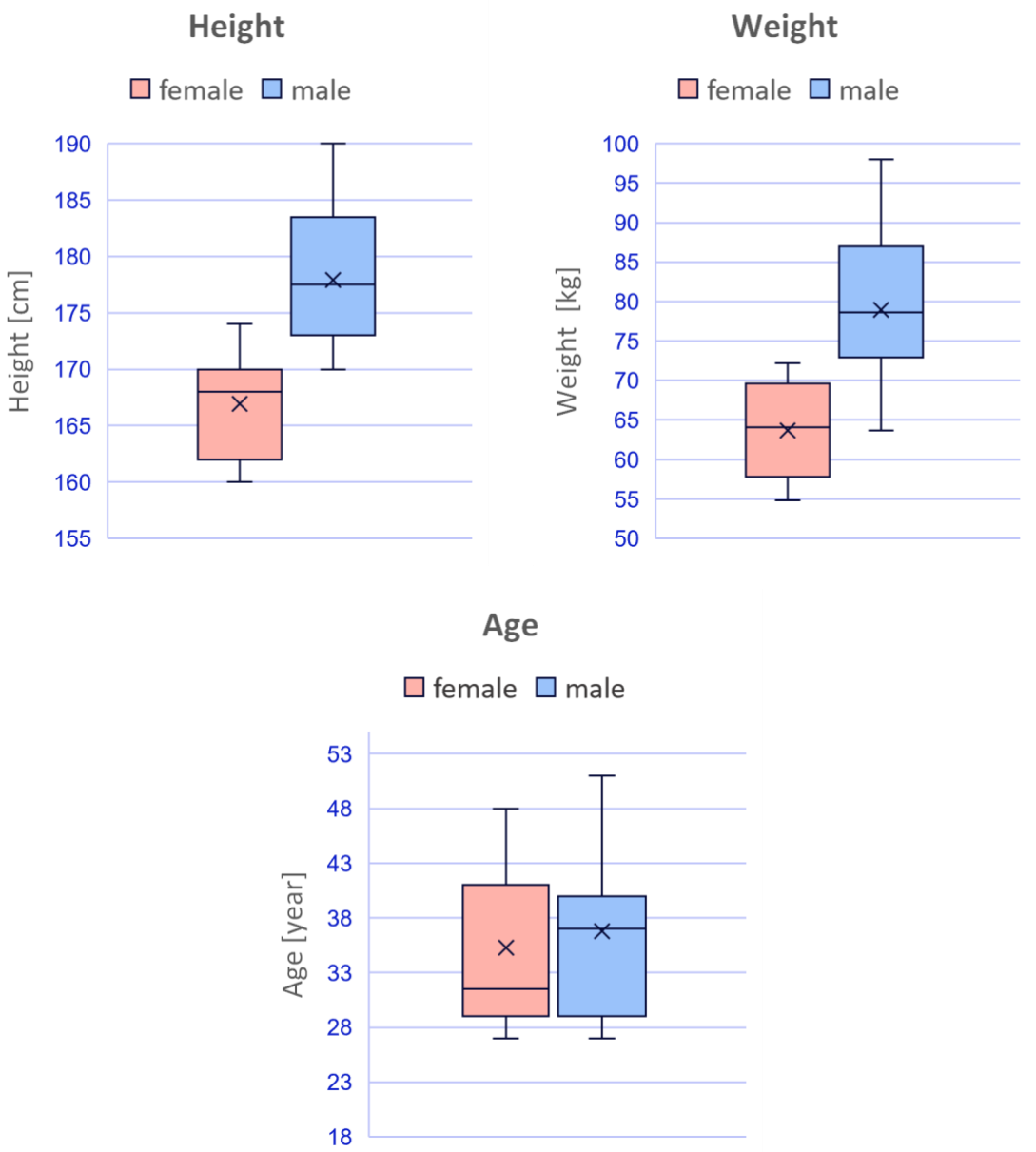

Figure 27: Distribution of height, weight and age of the volunteers

This project has received funding from the European Union’s Horizon 2020 research and innovation programme under Grant Agreement 861570.

Before a volunteer started a series of measurements, he or she was dressed in tight black clothing. Specific anatomical landmarks were equipped with “target stickers” (see Figure 27).

4.2.1 Pre survey

In addition to the specifications already recorded (height, weight, age), measurements were taken to obtain information regarding the anthropometry. As the following figures show, the measurements were taken in the upright position.

Figure 28: Pre-survey procedure

The following measurements were taken using a structured process for each volunteer:

- Knee height [cm]
- Trochanter height [cm]
- Shoulder height [cm]
- Length Collarbone [cm]
- Distance: body centre to collarbone [cm]

This project has received funding from the European Union’s Horizon 2020 research and innovation programme under Grant Agreement 861570.

4.2.2 Vehicle survey

In addition, the position of the test person in the vehicle environment was measured. The interior is equipped for this purpose with easily recognisable markers of which the position is known.

Figure 29: Vehicle interior with measured points

The following positions relative to vehicle points and the absolute angles are determined.

Table 5: Measurements in the vehicle interior

Measurement	Further information
Seat	Longitudinal position in relation to the seat rail
Heel	Position in relation to interior markers
Knee	Position in relation to interior markers
Trochanter	Position in relation to interior markers
Belt	Position in relation to collarbone (body centre)
Belt angle	Opening angle (shoulder belt to lap belt) at D-anchor
Upper leg angle	Angle in relation to horizontal
Lower leg angle	Opening angle (upper- to lower leg)
Head angle	Frankfurt plan in relation to horizontal
Knee distance	Centre of kneecap as reference

The anthropometrics and the position in the vehicle are determined for all volunteers (see Figure 35).

This project has received funding from the European Union's Horizon 2020 research and innovation programme under Grant Agreement 861570.


Figure 30: Measured volunteers in the test vehicle

4.3 Data acquisition, -processing and analysis

An overview of the used measurement technology, its area of coverage, as well as its evaluation is given.

4.3.1 Measurement equipment

The central unit of data acquisition was the Dewesoft SBOX, a powerful data processing computer and highly reliable SSD data logger for SIRIUS modular data acquisition systems for mobile and field test and measurement applications.

The Dewesoft unit was set up to trigger the different measurement devices together at the same time. The following table provides an overview of the measurement techniques used.

Table 6: Measurement devices

Device	Frequency [Hz]	Unit
CAN-Bus	50	*several*
Kinect Azure	30	m
Tea Captiv Motion	64	mm
XSensor pressure mat	44.5	N/cm²
EMC/ECG	70 / 20	mV

This project has received funding from the European Union's Horizon 2020 research and innovation programme under Grant Agreement 861570.

- **Microsoft Kinect Azure DK**

  Azure Kinect is a state-of-the-art spatial computing developer kit with sophisticated machine vision and speech models, advanced AI sensors, and a set of powerful SDKs that connect to Azure Cognitive Services. The software was specially adapted for the volunteer tests. The recording is triggered by the Dewesoft environment, and a targeted storage of relevant body landmarks is performed.

- **TEA Captiv Motion**

  The inertial wireless sensors were mounted on the head, chest, and each of the upper arm and forearm. This system serves as a support for the visually recorded occupant motion. External triggering via Dewesoft has been implemented.

- **XSENSOR Pressure Mat:**

  The seat and the backrest were equipped with a pressure measurement mat. However, results are only available for selected volunteers.

- **EMC/ECG:**

  During the experiment, muscle activity in the lower and upper body was being measured using a wearable fitness technology, i.e., athletic compression shorts/leggings and shirt with integrated surface electromyography (EMG) electrodes (Athos®, Redwood City, CA, USA). Compression shorts for men and leggings for women both include eight electrodes covering four bilateral lower-body muscles in total: hamstrings (biceps femoris), outer quadriceps (vastus lateralis), inner quadriceps (vastus medialis), and glutes (gluteus maximus). Men's and women's compression shirts, on the other hand, include twelve electrodes covering six bilateral upper-body muscles in total: pecs (pectoralis major), triceps, biceps, shoulders (deltoid), upper back (trapezius), and lower back (latissimus dorsi). Prior to the experiment execution, participants were asked to perform several overcoming isometric exercises using objects available on the test track to measure maximum voluntary contraction (MVC) of the four upper-body and six lower-body muscles of each individual participant. The execution of the MVC exercises was being monitored by the data collection team. Muscle activity of each participant was defined as muscle contraction relative to the individual MVC (i.e., % MVC). The synchronization signal (Dewesoft trigger) is used to detect different driving manoeuvres during the experiment in the EMG and ECG data.

The recording of all measuring systems was started simultaneously at the beginning (drive off to the event initiation point). The test vehicle drives its recorded trajectory autonomously.

This project has received funding from the European Union's Horizon 2020 research and innovation programme under Grant Agreement 861570.

4.4 Results

In this chapter, exemplary results of the previously mentioned measuring systems are presented.

4.4.1 Vehicle kinematic

For the respective event, the corresponding vehicle acceleration values are shown for all tests performed. In order to be able to realize the temporal assignment mentioned at the beginning, the curves are synchronized to a threshold value (black dot in figure 8). Obvious outliers (e.g. yellow curve at 50 km/h braking) are not further considered.

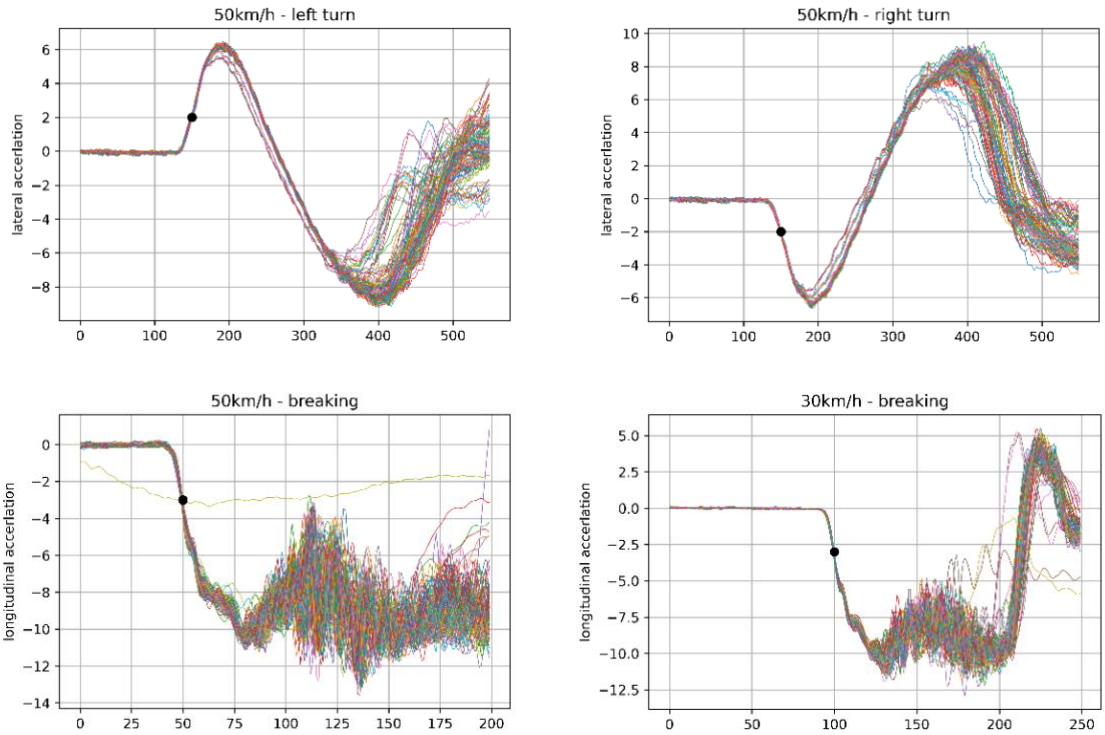

Figure 31: Vehicle acceleration values for all performed tests

Deviating acceleration values can be observed especially during braking manoeuvres. This is due to the antilock braking system (ABS) of the vehicle. Slight deviations in the acceleration values can be noticed for the left and right lane changes. The condition of the tyres as well as the coefficient of friction to the road can explain this behaviour.

4.4.2 Occupant kinematic

Data from the Kinect measurement system is used to quantify occupant motion. The data from the TEA Captiv Motion measurement system can be used to check the occupant motion recorded by the Kinect system. The evaluation is based on a change of the angle (front and side) of individual segments. The local coordinate system of every segment point is not

This project has received funding from the European Union's Horizon 2020 research and innovation programme under Grant Agreement 861570.

rotated but moves with the motion of the segment point. The following figure shows the orientation of the coordinate system (left) and an exemplary segment (right) for a specific timestep.

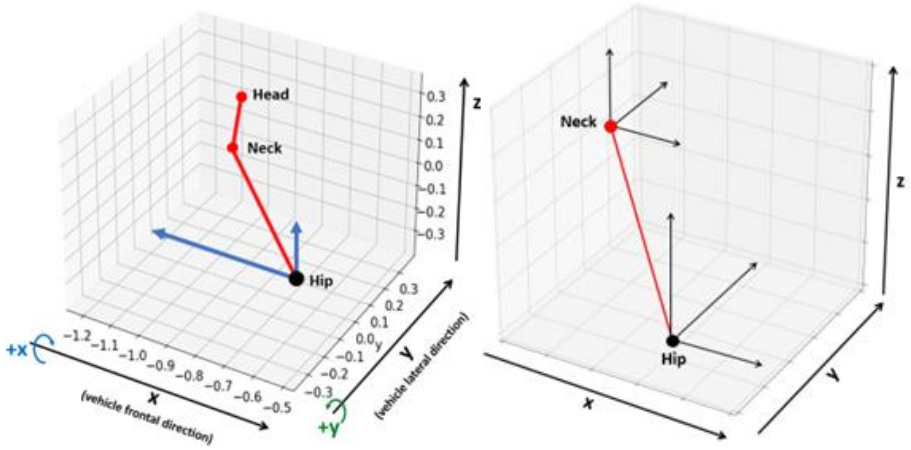

Figure 32: Coordinate system with evaluated segments for the quantification of occupant movement

Based on the approximated positions of the selected body points, the angles were defined according to the following figure.

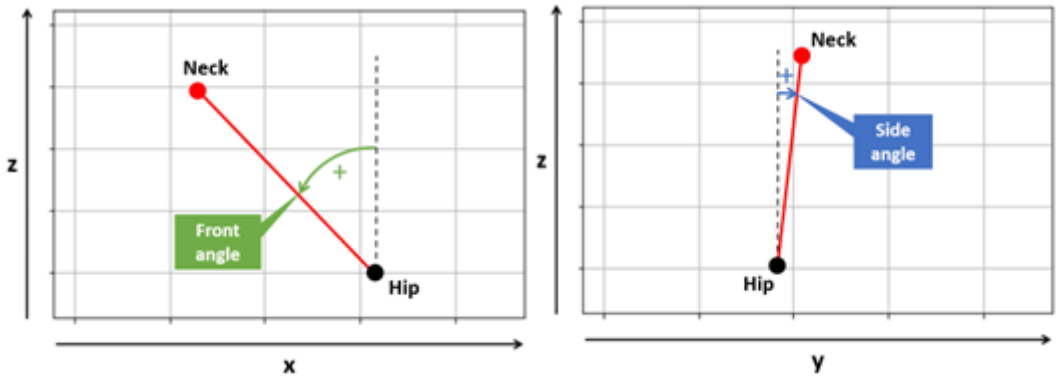

Figure 33: Definition of front and side angle

In accordance with [98] the collected data was statistically analysed. The goal was, to develop a mathematical model, which uses the kinematics data of all volunteers and their anthropometric data (see Chapter 4.2.1) to predict the head and thorax kinematics for given anthropometric distances, gender and age. This includes the following points:

- Time-zeroing the data based on identifying the first point at which acceleration on a specific axis exceeds a certain threshold.
- Assembling time-series data on head and centre of gravity locations.
- Smoothing and reducing the dimension of the data using cubic splines.
- Conducting a principal component analysis to identify the primary modes of variation in the data.

This project has received funding from the European Union's Horizon 2020 research and innovation programme under Grant Agreement 861570.

- Using regression analysis to predict the effects of test conditions and subject characteristics on the data.
- Illustrating the effects of these factors on the data using the results of the regression analysis.

Based on the statistical evaluation, a mathematical model is trained, to predict the kinematics of head and thorax based on age, gender and anthropometric parameters. This mathematical model is further used, to predict the kinematics of males with an anthropometry of a THUMS v3 and females with an anthropometry of the VIVA HBM. Figure 34 shows the predicted kinematics of head and thorax in a selected manoeuvre (30 kph braking).

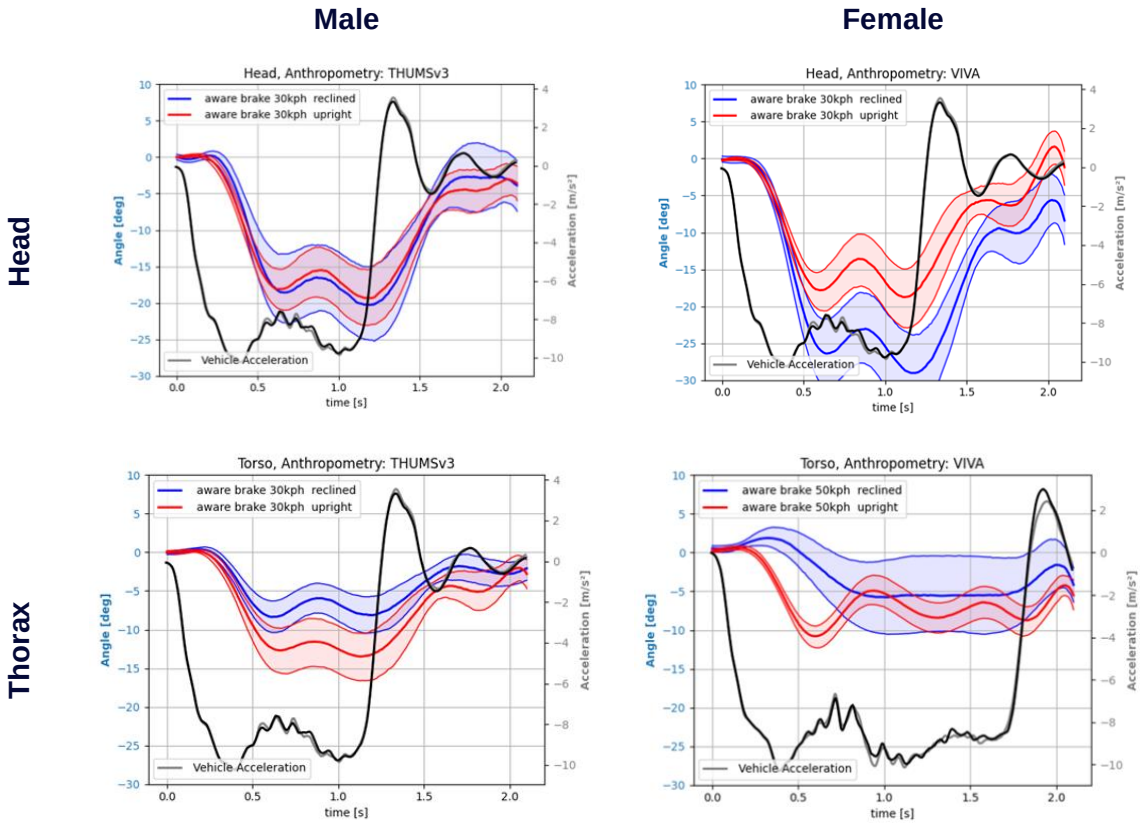

Figure 34: Response corridors for the thorax (50th percentile +/- 25%) in 30 kph and 50 kph braking manoeuvres, reclined and upright sitting position and for male and female anthropometry

For 30 kph the head excursion for a male occupant are roughly the same in reclined and upright sitting position. Females tend to have a slightly higher excursion in a reclined sitting position. The gradient of the first excursion is similar for all diagrams in Figure 34. Furthermore, the time at which the forward motion is initialized is similar in all shown cases.

The thoracic excursion is rather low and additionally the maximum excursions compared between males and females are similar, since the thoracic kinematic is determined by the belt characteristics.

This project has received funding from the European Union's Horizon 2020 research and innovation programme under Grant Agreement 861570.

Note, that the angles are relative to the initial position and that a seat integrated belt was used which avoids a belt slack at the beginning of the motion. The remaining manoeuvres are documented in Appendix F – Occupant response corridors.

4.4.3 Pressure mat data

The evaluation of the measurement data of the pressure mats is carried out with the aid of software produced in-house. The following figure shows two different times of a recorded manoeuvre.

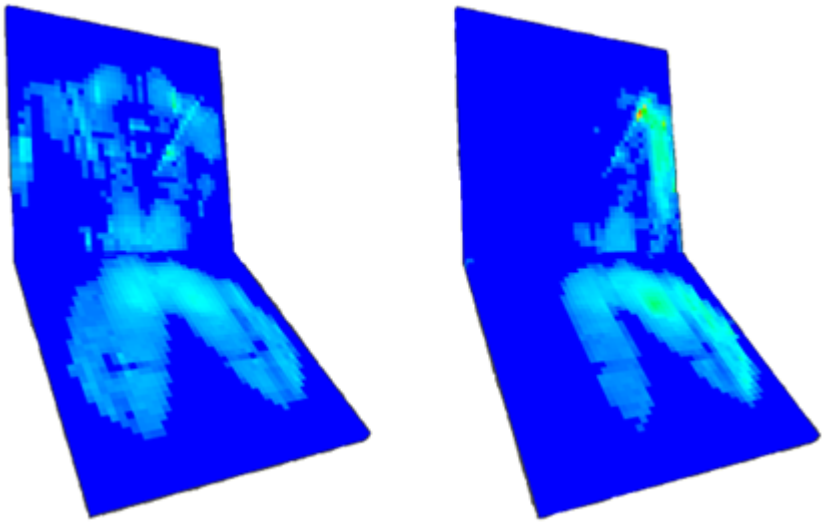

Figure 35: Exemplary evaluation of a pressure distribution for seat and backrest (left: start position, right: maximum lateral displacement of occupant)

With the help of this information, further interpretations of the occupant motion and their weight distributions are possible. For positioning HBMs the gained data allow to compare the initial sitting position in the FE simulation with the sitting position in the volunteer tests. The recorded data from the pressure mats is not further analysed in this project.

4.4.4 Muscle activity

Muscle activity was measured for 21 participants of the volunteer study. Muscle measurement was done for all listed manoeuvres in Table 7. Following diagrams show exemplarily the normalized muscle activity of a single volunteer in a breaking and in a steering (left) manoeuvre for the recorded muscles. Muscles are divided in the body regions leg, arms and back. Breaking and steering were initiated at a velocity of 50 km/h in an unaware state and in a reclined sitting position. Further analysis of the gained data will be done in future studies.

This project has received funding from the European Union's Horizon 2020 research and innovation programme under Grant Agreement 861570.

	Left	Right
Back	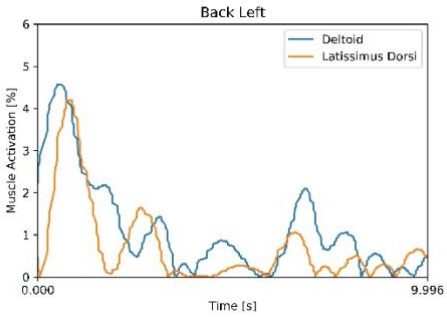	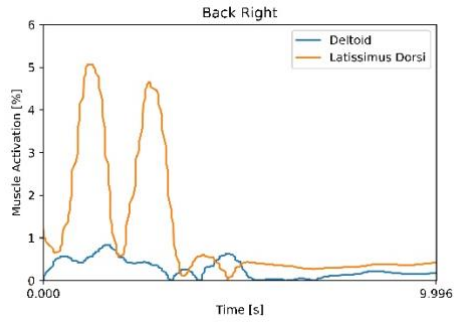
Leg	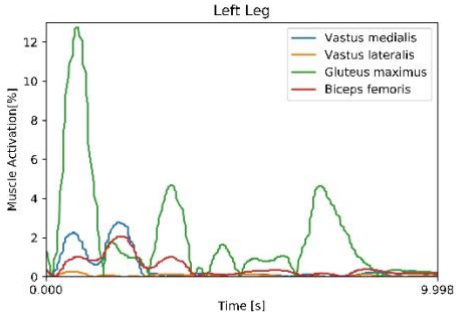	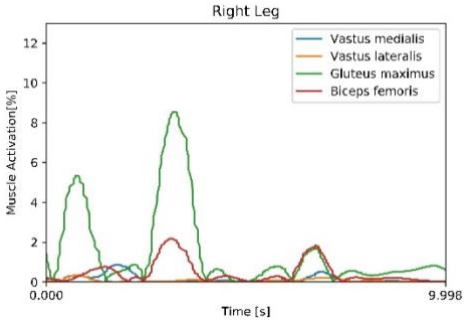
Arm	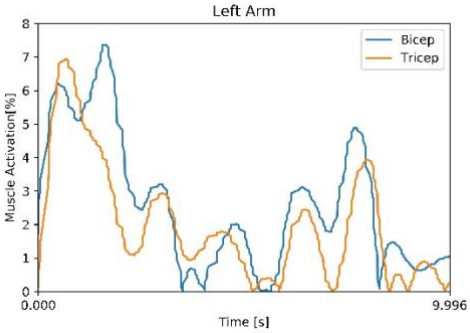	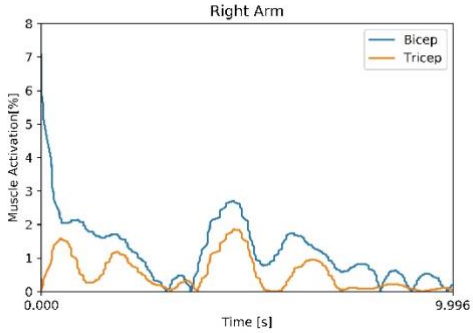

Table 7: Muscle activity in a 50kph braking manoeuvre

This project has received funding from the European Union's Horizon 2020 research and innovation programme under Grant Agreement 861570.

	Left	Right
Back	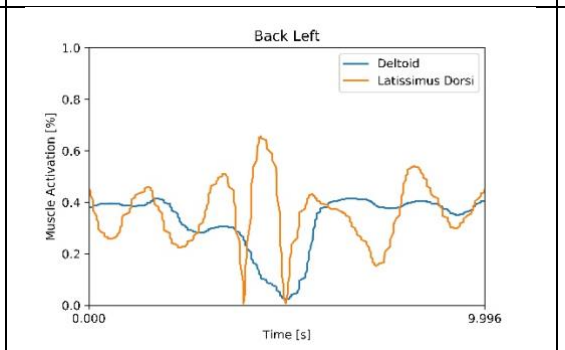	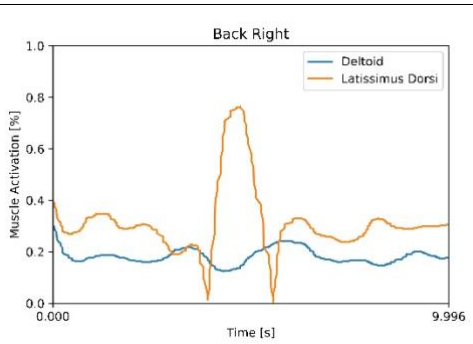
Leg	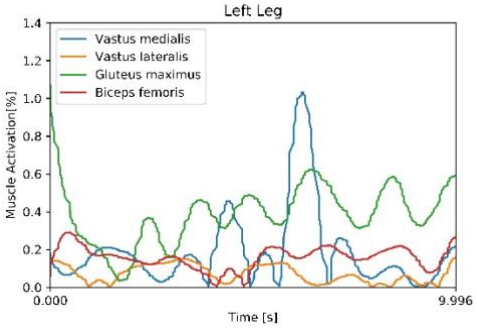	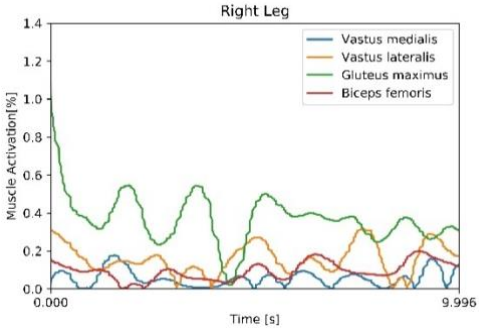
Arm	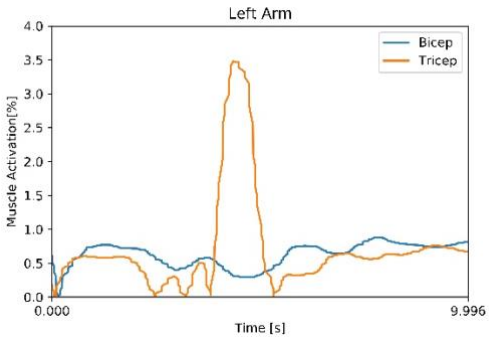	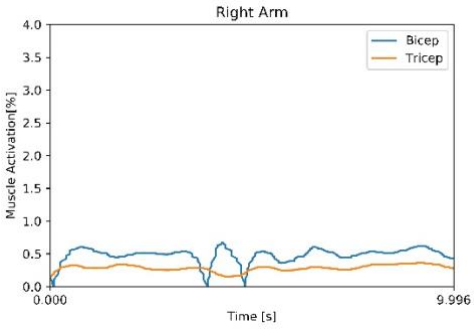

Table 8: Muscle activity in a steering (left) manoeuvre

This project has received funding from the European Union's Horizon 2020 research and innovation programme under Grant Agreement 861570.

	Left	Right
Back	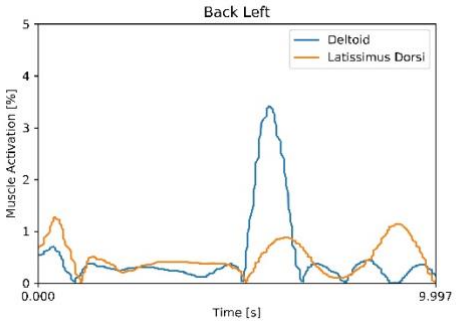	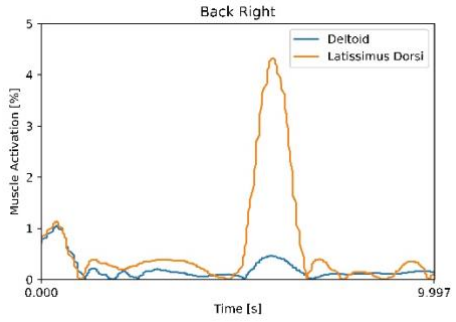
Leg	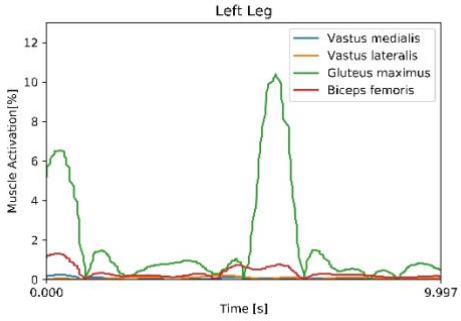	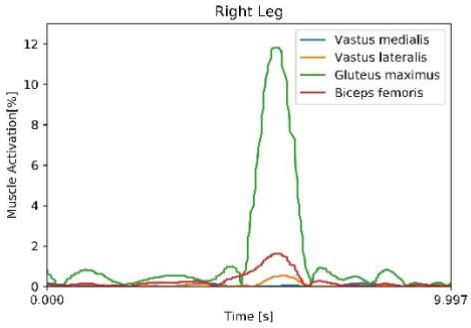
Arm	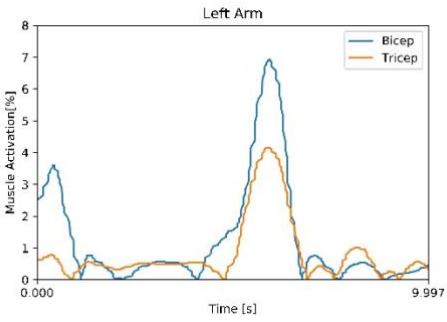	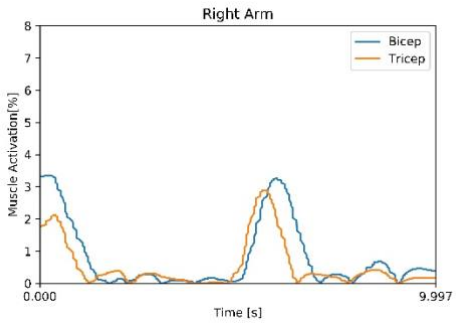

Table 9: Muscle activity in a steering (right) manoeuvre

This project has received funding from the European Union's Horizon 2020 research and innovation programme under Grant Agreement 861570.

4.5 Conclusion

39 female and male volunteers were participating in this study. Unfortunately, only 12 participants were females. Further, the average age is 35 years for females and 36 years for the males. For future studies, the aim should be to get a balanced field of participants with a higher average age.

Besides the kinematics, muscle activity and contact forces to the seat were recorded. An additional measurement of the contact force between shoes and the vehicle would be beneficial in future studies. Contact forces and muscle activity data were currently not further analysed. It is planned to use the muscle activity data for active Human Body Model enhancement, and the contact force data for the positioning of the HBMs.

A mathematical model was developed, which allows the prediction of head and thorax kinematics, based on certain anthropometric distances, gender and age. The data basis for the prediction are the kinematics data of the volunteer study.

For the unaware cases, the participants were not specifically distracted, they were just not informed. A specific distraction and different points on the test track for the manoeuvre initialization would also help to gain more realistic data. Following results can be observed for the braking and steering manoeuvre (see Figure 34 and Appendix F – Occupant response corridors):

Braking manoeuvres:

- Torso excursion depends on the belt characteristics → low compared to head excursion
- Similar head excursion for 30 kph and 50 kph
- Similar head excursion for males in reclined and upright positions
- Higher excursions for females in reclined sitting positions compared to upright sitting

Steering manoeuvres:

- Lower excursions for head and thorax compared to braking manoeuvres
- Similar excursions for males and females
- Differences in left and right steering → occupants try to avoid getting in contact with the B-pillar

This project has received funding from the European Union's Horizon 2020 research and innovation programme under Grant Agreement 861570.

5. Active HBM torque controller

The occupant kinematics during a pre-crash manoeuvre like braking or steering has an influence on the injury risk. The influence of pre-crash manoeuvres on the occupant kinematics is shown e.g. in [99] and. [101] demonstrated that e.g. Nij and VCmax were clearly reduced by the usage of active models. Further, [100] and [102] highlighted, that the injury risk is influenced by pre-crash occupant kinematics.

Human Body Models enable this consideration but require a kinematic controller to depict a human like response in typical pre-crash manoeuvres. Amongst others, [103] and [104] presented PID controlled muscle models which works with beam elements in the HBM. Each of the beams represents a muscle in the human body. A torque based controller is presented in [105], which does not depict the entire set of muscles in the human body, but uses torques which are applied on the vertebras of the HBM

In this project, this approach was enhanced to reclined sitting positions. Therefore, the dataset which was gained in a volunteer study (see Chapter 4) is used. A torque based controller was enhanced for reclined sitting positions, to depict volunteer kinematics (chapter 4) with the HBM. The method was demonstrated for a THUMS v3, but the modelling approach makes it possible to adapt to other HBMs easily.

5.1 Environment

For the development of the active controller, the data from the conducted volunteer series was used (see Chapter 4). Since the geometry of the seat is crucial for pre-crash kinematics, a FE model was built. Therefore, a 3D model of the seat, based on several images was computed. That was further used to create a FE model.

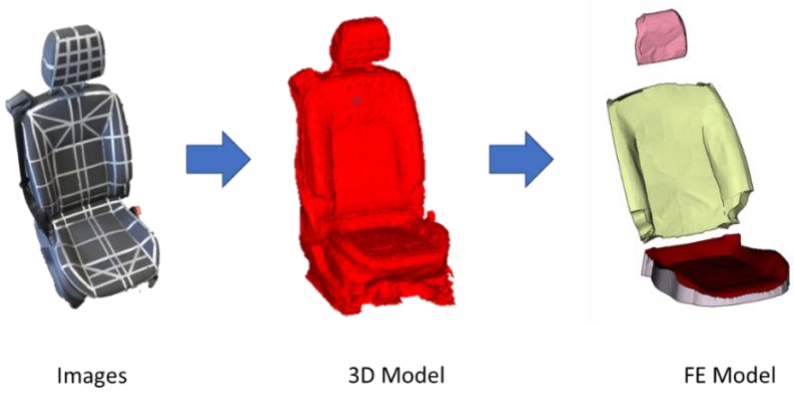

Figure 36: Development of a FE seat model based on images

This project has received funding from the European Union's Horizon 2020 research and innovation programme under Grant Agreement 861570.

An existing belt system was used. An analysis of the locking behaviour showed that the used belt in the real seat works very similar to the existing model. Therefore, no further analysis or model development documentation is given in this report.

5.2 Controller

The position of the HBM and the position of the underlying volunteer database are described by the head and thorax angle as described in in Chapter 4.4.2. The used FE solvercode was LS-Dyna v9.3.1. This section describes the principle of the PD torque controller for the active HBM.

The main principle of the active controller (see Figure 37) is to apply torques to each vertebra to keep the HBM in its initial position. That applies to all timesteps and should keep the HBM in its initial position, even if the seat is accelerated. Following points describe the workflow of the controller and are also indicated in Figure 37

1) Therefore, the deviation to the initial posture is described with the angle and the angular velocity for head and thorax in every timestep.
2) This deviations are multiplied by proportional and differential controller factors (2)
3) Next, they are applied to the inverse model (see chapter 5.2.1). The inverse model is capable of predicting the necessary torques (Mx, My) based on the current deviation and the current acceleration of the seat (sled). A more detailed description of the inverse model is given in chapter 5.2.1.
4) The determined torques are further limited (4) to avoid overprediction and unnatural behaviour.
5) A time delay is applied to depict a reaction time
6) Torques are applied to the vertebras of the FE HM

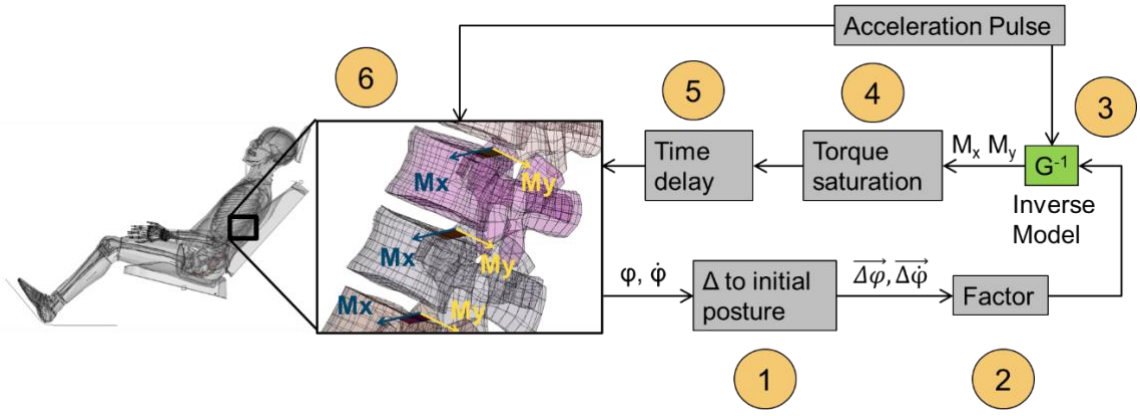

Figure 37: Concept of the active torque controller

This project has received funding from the European Union's Horizon 2020 research and innovation programme under Grant Agreement 861570.

5.2.1 Surrogate model and inverse model

The surrogate model depicts the thorax and the head kinematics with a multibody (multi-pendulum) model [75] (see Figure 38). The bodies were connected with joints with rotational stiffness. The stiffness is determined for every joint to guarantee similar kinematics of the surrogate model and the HBM. The surrogate model then shows a certain excursion if a certain torque is applied in a vertebra.

An inverse model does the opposite: It determines the torque in the vertebra which is necessary to reach a certain excursion. The surrogate model was formulated in the Python package PyBullet. It allows to build an inverse model of a multibody system.

The inverse model was further used in the controller for the torque prediction based on angular and velocity deviations.

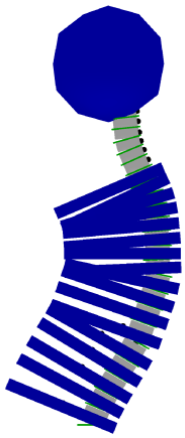

Figure 38: Surrogate model of the torso and head/neck

5.3 Determination of the controller parameters

As the determination of the controller parameters with an included FE model (see Figure 37) is very time consuming, the first estimation for the parameters was done with the surrogate model (see Figure 39).

This project has received funding from the European Union's Horizon 2020 research and innovation programme under Grant Agreement 861570.

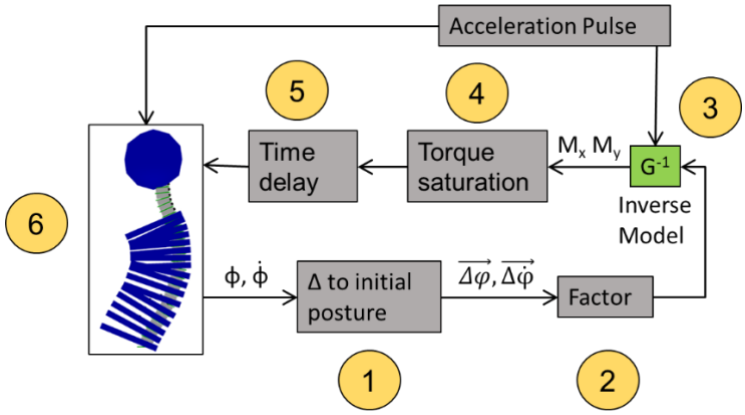

Figure 39: Controller parameter determination with the surrogate model

The fast-calculating surrogate model allows to run an optimization process to determine the controller parameters. In the next step, the surrogate model was replaced by the FE HBM and the controller parameters are adapted to fit to the occupant response from the volunteer study.

5.4 Controller application

5.4.1 Selected manoeuvre and occupant response

A Manoeuvre from Chapter 4 was selected to apply the controller. The analysis of the occupant kinematics showed that the torso kinematics was mostly influenced by the belt. Therefore, the controller development focuses on the head/neck kinematics. Further, the head excursion observed in the volunteer tests described in section 4 showed to be higher in the braking manoeuvres compared to the steering manoeuvres. For this reason, a 50 kph braking manoeuvre in an aware state and reclined sitting position was selected for the controller development.

With the mentioned linear models, it was possible to predict the kinematics for decided anthropometries, age, and gender. For this project, the THUMS v3 was used, which determines also the anthropometry and the gender. The age was defined with 35 which is the mean age of the volunteers in the dataset. That is done, to avoid “extrapolation” by the linear model, which might lead to unrealistic results. Figure 40 shows the predicted occupant kinematics and the vehicle acceleration.

This project has received funding from the European Union’s Horizon 2020 research and innovation programme under Grant Agreement 861570.

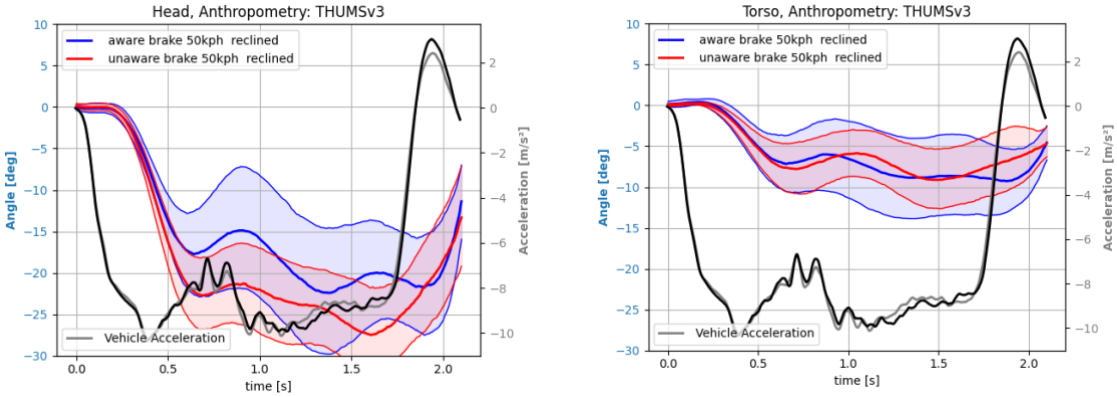

Figure 40: Predicted occupant response (head and torso angle) and vehicle acceleration for a 50kph braking manoeuvre in aware and unaware state

5.4.2 Results with active controller

Figure 41 shows the kinematics (head/neck angle) for a controlled THUMSv3 in a 50 kph braking scenario. The corridors were the +/- 25% to the 50% kinematics. The controlled HBM follows the 50% curve with small deviations during the forward bending. At the maximum forward excursion (roughly at 600 ms in this case) the controller strategy had to be switched. The goal of the controller was to bring the HBM back in its initial position. At the most forward point, the controller strategy was changed to keep the HBM in its most forward position and torque limiting is also adapted. With these settings, the head was not pulled back by the controller and was kept in the same positions as it is done by the average volunteer.

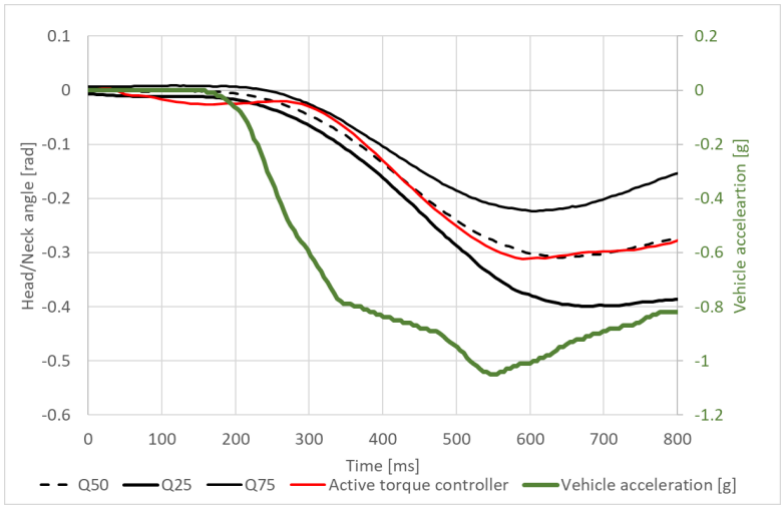

Figure 41: Head/neck angle of the active torque controlled HBM

This project has received funding from the European Union's Horizon 2020 research and innovation programme under Grant Agreement 861570.

5.5 Conclusion and next steps

Data from the volunteer study were used to predict the occupant kinematic of male and a female occupant with a THUMS v3 and a VIVA anthropometry (Chapter 4). To simulate the predicted kinematics was a HBM, an active torque controller was developed. The determined torques are imprinted on the vertebras of the model. Further, a multi-pendulum surrogate model of the HBM thorax and head was developed. This model is required of the controller and for the determination of the controller parameters.

The developed controller works for the selected 50 kph braking manoeuvre as demonstrated in this chapter. It enables the selected THUMS v3 HBM to follow the head excursion which was determined based on the volunteer study. Besides an oscillation at the beginning of the simulation (100 ms – 200 ms), the head angle of the HBM was within the +/-25% corridor of the volunteer study and depicts the characteristic of the head kinematics. The thorax kinematics is not investigated since it is mainly determined by the interaction with the shoulder belt and therefore mostly independent from the active controller.

As described above, the controller strategy was changed at the maximum head excursion to avoid a pull back of the head and to depict the behaviour of the volunteers properly. In the current version, this adaption was done time based. That needs to be exchanged by an approach which adapts the controller strategy based on the angular velocity and the sled acceleration pulse.

The next step is, to apply the controller to other crash pulses, to avoid a tuning to a single case. Moreover, the principle will be applied to steering manoeuvres as well to enhance the controller also for lateral loadings.

Further, the developed controller will be applied in female HBMs. The chosen approach allows a simple adaption of the active torque elements. Besides that, a new surrogate model has to be defined.

This project has received funding from the European Union's Horizon 2020 research and innovation programme under Grant Agreement 861570.

6. Dissemination and Exploitation

Lumbar spine developments:

- Submitted for inclusion in the IRCOBI 2023 proceedings.

Volunteer study:

- Video at the TRA conference 2022 at the stand of the European Commission and at the SAFE-UP stand
- Report in the TV show “nano” on January 16th 2023 at the German/Austrian/Swiss TV channel “3sat”
- Submitted manuscript for a full conference paper at the IRCOBI conference 2023 “*Passenger Kinematics in Reclined Sitting Position in Braking and Steering Manoeuvres*”

Torque controller

- Submitted manuscript for a short communication at the IRCOBI conference 2023 “*Development of an HBM torque controller for reclined sitting positions*”

This project has received funding from the European Union’s Horizon 2020 research and innovation programme under Grant Agreement 861570.

References

[1] Huelke, D.F., Mackay, G.M., and Morris, A. Vertebral column injuries and lap-shoulder belts. Journal of Trauma and Acute Care Surgery, 1995. 38(4): p. 547-556

[2] Pintar, F.A., Yoganandan, N., Maiman, D.J., Scarboro, M., and Rudd, R.W. Thoracolumbar spine fractures in frontal impact crashes. Proceedings of Annals of Advances in Automotive Medicine/Annual Scientific Conference, 2012.

[3] Adolph, T., Wisch, M., et al. Analyses of thoracic and lumbar spine injuries in frontal impacts. Proceedings of Proceedings of IRCOBI Conference on Biomechanics of Impacts, 2013.

[4] Kaufman, R.P., Ching, R.P., et al. Burst fractures of the lumbar spine in frontal crashes. Accident Analysis & Prevention, 2013. 59: p. 153-163

[5] Doud, A.N., Weaver, A.A., et al. Has the incidence of thoracolumbar spine injuries increased in the United States from 1998 to 2011? Clinical Orthopaedics and Related Research®, 2015. 473: p. 297-304

[6] Jakobsson, L., Björklund, M., and Westerlund, A. Thoracolumbar spine injuries in car crashes. Proceedings of International Conference on the Biomechanics of Injury, 2016.

[7] Shaikh, J., Thathia, H., and Lubbe, N. Lumbar spine injuries in motor vehicle crashes. Proceedings of Proceedings of IRCOBI Asia Conference, 2020.

[8] Begeman, P.C., King, A.I., and Prasad, P. Spinal loads resulting from-Gx acceleration. 1973, SAE Technical Paper.

[9] Patrick, L. and Levine, R. Injury to unembalmed belted cadavers in simulated collisions. 1975, SAE Technical Paper.

[10] Rouhana, S.W., Bedewi, P.G., et al. Biomechanics of 4-point seat belt systems in frontal impacts. *Stapp car crash journal*, 2003. 47: p. 367

[11] Richardson, R., Donlon, J.-P., et al. Kinematic and injury response of reclined PMHS in frontal impacts. *Stapp car crash journal*, 2020. 64: p. 83-153

[12] Richardson, R., Jayathirtha, M., et al. Thoracolumbar spine kinematics and injuries in frontal impacts with reclined occupants. *Traffic injury prevention*, 2020. 21(sup1): p. S66-S71

[13] Katsuhara, T., Takahira, Y., Hayashi, S., Kitagawa, Y., and Yasuki, T. Analysis of driver kinematics and lower thoracic spine injury in world endurance championship race cars during frontal impacts. *SAE International journal of transportation safety*, 2017. 5(1): p. 120-132

[14] Boyle, K.J., Reed, M.P., Zaseck, L.W., and Hu, J. A human modelling study on occupant kinematics in highly reclined seats during frontal crashes. *Proceedings of Proceedings of the International Research Conference on the Biomechanics of Impact, IRCOBI, Florence, Italy, 11th September-13th September. IRC-19-43*, 2019.

This project has received funding from the European Union's Horizon 2020 research and innovation programme under Grant Agreement 861570.

[15] Rawska, K., Gepner, B., et al. Submarining sensitivity across varied anthropometry in an autonomous driving system environment. *Traffic injury prevention*, 2019. 20(sup2): p. S123-S127

[16] Butala, K., Gotwals, D., Tangirala, R., and Shanks, K. Occupant Behavior in Small Front Overlap Event – A Parametric Study. *Proceedings of 23st International Technical Conference on the Enhanced Safety of Vehicles*, 2013. Seoul, Republic of Korea

[17] Gayzik, F.S., Moreno, D.P., Vavalle, N.A., Rhyne, A.C., and Stitzel, J.D. Development of a full human body finite element model for blunt injury prediction utilizing a multi-modality medical imaging protocol. Proceedings of 12th International LS-DYNA User Conference, 2012.

[18] Shigeta, K., Kitagawa, Y., and Yasuki, T. Development of next generation human FE model capable of organ injury prediction. Proceedings of The 21st Annual Enhanced Safety of Vehicles, 2009. Stuttgart, Germany

[19] Pipkorn, B., Östh, J., et al. Validation of the SAFER Human Body Model Kinematics in Far-Side Impacts. Proceedings of the International IRCOBI Conference, 2021. Online

[20] Weaver AA, Barnard RT, Kilgo PD, Martin RS, Stitzel JD. Mortality-based Quantification of Injury Severity for Frequently Occurring Motor Vehicle Crash Injuries. In: *Proceedings of the AAAM Annual Conference*. Québec City, Canada; 2013:235–46.

[21] Pipkorn B, Iraeus J, Lindkvist M, Puthan P, Bunketorp O. Occupant injuries in light passenger vehicles—A NASS study to enable priorities for development of injury prediction capabilities of human body models. *Accident Analysis and Prevention* 2020; **138**. doi:10.1016/j.aap.2020.105443.

[22] Renaudin F, Guillemot H, Lavaste F, Skalli W, Lesage F, Pecheux C. A 3D finite element model of pelvis in side impact. *SAE Technical Paper 933130* 1993. doi:10.4271/933130.

[23] Plummer JW, Bidez MW, Alonso J. Parametric Finite Element Studies of the Human Pelvis: The Influence of Load Magnitude and Duration on Pelvic Tolerance During Side Impact. In: *Proceedings of the Stapp Car Crash Conference*. Albuquerque, New Mexico, USA; 1996:17–28.

[24] Besnault B, Lavaste F, Guillemot H, Robin S, Coz J-Y Le. A Parametric Finite Element Model of the Human Pelvis. *SAE Technical Paper 983147* 1998. doi:10.4271/983147.

[25] Konosu A. Development of a biofidelic human pelvic FE-model with several modifications onto a commercial use model for lateral loading conditions. *SAE Technical Paper 2003-01-0163* 2003. doi:10.4271/2003-01-0163.

[26] Kikuchi Y, Takahashi Y, Mori F. Development of a Finite Element Model for a Pedestrian Pelvis and Lower Limb. *SAE Technical Paper 2006-01-0683* 2006. doi:10.4271/2006-01-0683.

This project has received funding from the European Union's Horizon 2020 research and innovation programme under Grant Agreement 861570.

[27] Song E, Trosseille X, Guillemot H. Side Impact: Influence of Impact Conditions and Bone Mechanical Properties on Pelvic Response Using a Fracturable Pelvis Model. *Stapp Car Crash Journal* 2006; **50**:75–95. doi:10.4271/2006-22-0004.

[28] Untaroiu CD, Guillemot H, Salzar RS, Crandall JR. The Strain Distribution and Force Transmission Path Through Pubic Rami During Lateral Pelvic Impacts. In: *Proceedings of the IMECE*. Boston, Massachusetts, USA; 2008.

[29] Ma Z, Lan F, Chen J, Liu W. Finite Element Study of Human Pelvis Model in Side Impact for Chinese Adult Occupants. *Traffic Injury Prevention* 2015; **16**(4):409–417. doi:10.1080/15389588.2014.950370.

[30] Kunitomi S, Yamamoto Y, Kato R, et al. The Development of the Lower Extremity of a Human FE Model and the Influence of Anatomical Detailed Modelling in Vehicle-to-Pedestrian Impacts. In: *Proceedings of the IRCOBI Conference*. Antwerp, Belgium; 2017.

[31] John, J., Klug, C., Kranjec, M., Svenning, E., and Iraeus, J. Hello, world! VIVA+: A human body model lineup to evaluate sex-differences in crash protection. Frontiers in bioengineering and biotechnology, 2022. 10

[32] Tushak, S.K., Gepner, B.D., Pipkorn, B., and Kerrigan, J.R. Evaluation of the GHBMC lumbar spine in sub-injurious and injurious loading. Proceedings of Conference Proceedings of International Research Council on Biomechanics of Injury, 2022.

[33] Yoganandan, N., Moore, J., et al. Human lumbar spinal column injury criteria from vertical loading at the base: Applications to military environments. Journal of the Mechanical Behavior of Biomedical Materials, 2020: p. 103690

[34] Gayzik, F., Hamilton, C.A., et al. A Multi-Modality Image Data Collection Protocol for Full Body Finite Element Model Development. 2009, SAE Technical Paper.

[35] Kopperdahl, D.L., Morgan, E.F., and Keaveny, T.M. Quantitative computed tomography estimates of the mechanical properties of human vertebral trabecular bone. Journal of orthopaedic research, 2002. 20(4): p. 801-805

[36] Ulrich, D., Van Rietbergen, B., Laib, A., and Ruegsegger, P. The ability of three-dimensional structural indices to reflect mechanical aspects of trabecular bone. Bone, 1999. 25(1): p. 55-60

[37] Edwards, W.T., Zheng, Y., Ferrara, L.A., and Yuan, H.A. Structural features and thickness of the vertebral cortex in the thoracolumbar spine. Spine, 2001. 26(2): p. 218-225

[38] Khor, F., Cronin, D.S., Watson, B., Gierczycka, D., and Malcolm, S. Importance of asymmetry and anisotropy in predicting cortical bone response and fracture using human body model femur in three-point bending and axial rotation. Journal of the mechanical behavior of biomedical materials, 2018. 87: p. 213-229

[39] Wu, Y., Loaiza, J., Banerji, R., Blouin, O., and Morgan, E. Structure-function relationships of the human vertebral endplate. JOR spine, 2021. 4(3): p. e1170

This project has received funding from the European Union's Horizon 2020 research and innovation programme under Grant Agreement 861570.

[40] Cassidy, J., Hiltner, A., and Baer, E. Hierarchical structure of the intervertebral disc. Connective tissue research, 1989. 23(1): p. 75-88

[41] Alonso, F. and Hart, D., "Encyclopedia of the Neurological Sciences", Elsevier, 2014

[42] Holzapfel, G.A., Schulze-Bauer, C., Feigl, G., and Regitnig, P. Single lamellar mechanics of the human lumbar anulus fibrosus. Biomechanics and modeling in mechanobiology, 2005. 3(3): p. 125-140

[43] Newell, N., Little, J., et al. Biomechanics of the human intervertebral disc: A review of testing techniques and results. Journal of the mechanical behavior of biomedical materials, 2017. 69: p. 420-434

[44] Panzer, M.B. and Cronin, D.S. C4–C5 segment finite element model development, validation, and load-sharing investigation. Journal of biomechanics, 2009. 42(4): p. 480-490

[45] Chazal, J., Tanguy, A., et al. Biomechanical properties of spinal ligaments and a histological study of the supraspinal ligament in traction. Journal of biomechanics, 1985. 18(3): p. 167-176

[46] Mattucci, S.F. and Cronin, D.S. A method to characterize average cervical spine ligament response based on raw data sets for implementation into injury biomechanics models. Journal of the mechanical behavior of biomedical materials, 2015. 41: p. 251-260

[47] Nolte, L.P., Panjabi, M., and Oxland, T. Biomechanical properties of lumbar spinal ligaments. Clinical implant materials, advances in biomaterials, 1990. 9: p. 663-668

[48] Jamison, D., Cannella, M., Pierce, E.C., and Marcolongo, M.S. A comparison of the human lumbar intervertebral disc mechanical response to normal and impact loading conditions. Journal of Biomechanical Engineering, 2013. 135(9)

[49] Asano, S., Kaneda, K., Umehara, S., and Tadano, S. The Mechanical Properties of the Human L4–5 Functional Spinal Unit During Cyclic Loading: The Structural Effects of the Posterior Elements. Spine, 1992. 17(11): p. 1343-1352

[50] Marini, G., Studer, H., Huber, G., Püschel, K., and Ferguson, S.J. Geometrical aspects of patient-specific modelling of the intervertebral disc: Collagen fibre orientation and residual stress distribution. Biomechanics and modeling in mechanobiology, 2016. 15(3): p. 543-560

[51] Markolf, K.L. and Morris, J.M. The structural components of the intervertebral disc: a study of their contributions to the ability of the disc to withstand compressive forces. JBJS, 1974. 56(4): p. 675-687

[52] Heuer, F., Schmidt, H., Claes, L., and Wilke, H.-J. Stepwise reduction of functional spinal structures increase vertebral translation and intradiscal pressure. Journal of biomechanics, 2007. 40(4): p. 795-803

[53] Jaramillo, H.E., Puttlitz, C.M., McGilvray, K., and García, J.J. Characterization of the L4–L5–S1 motion segment using the stepwise reduction method. Journal of Biomechanics, 2016. 49(7): p. 1248-1254

This project has received funding from the European Union's Horizon 2020 research and innovation programme under Grant Agreement 861570.

[54] Yamamoto, I., Panjabi, M.M., Crisco, T., and Oxland, T. Three-dimensional movements of the whole lumbar spine and lumbosacral joint. Spine, 1989. 14(11): p. 1256-1260

[55] Demetropoulos, C.K., Yang, K.H., Grimm, M.J., Khalil, T.B., and King, A.I. Mechanical properties of the cadaveric and Hybrid III lumbar spines. SAE transactions, 1998: p. 2862-2871

[56] ISO/TR 12350:2013. Road vehicles -- Injury risk curves for the evaluation of occupant protection in side impact tests. 2013: Geneva, Switzerland.

[57] Petitjean, A. and Trosseille, X. Statistical simulations to evaluate the methods of the construction of injury risk curves. 2011, SAE Technical Paper.

[58] Brinckmann, P., Biggemann, M., and Hilweg, D. Prediction of the compressive strength of human lumbar vertebrae. Clinical Biomechanics, 1989. 4: p. iii-27

[59] Duma, S.M., Kemper, A.R., McNeely, D.M., Brolinson, P.G., and Matsuoka, F. Biomechanical response of the lumbar spine in dynamic compression. Biomedical sciences instrumentation, 2006. 42: p. 476-481

[60] Granhed, H., Jonson, R., and Hansson, T. Mineral content and strength of lumbar vertebrae A cadaver study. Acta Orthopaedica Scandinavica, 1989. 60(1): p. 105-109

[61] Hutton, W. and Adams, M. Can the lumbar spine be crushed in heavy lifting? Spine, 1982. 7(6): p. 586-590

[62] Tushak, S.K., Donlon, J.P., et al. Failure tolerance of the human lumbar spine in dynamic combined compression and flexion loading. Journal of Biomechanics, 2022. 135: p. 111051

[63] Ortiz-Paparoni, M., Op't Eynde, J., et al. The human lumbar spine during high-rate under seat loading: a combined metric injury criteria. Annals of biomedical engineering, 2021. 49: p. 3018-3030

[64] Yoganandan, N., Arun, M.W., Stemper, B.D., Pintar, F.A., and Maiman, D.J. Biomechanics of human thoracolumbar spinal column trauma from vertical impact loading. Annals of advances in automotive medicine, 2013. 57: p. 155

[65] Pintar, F.A. Biomedical analyses, tolerance, and mitigation of acute and chronic trauma. 2012, MEDICAL COLL OF WISCONSIN MILWAUKEE.

[66] Yoganandan, N., Moore, J., Arun, M.W., and Pintar, F.A. Dynamic responses of intact post mortem human surrogates from inferior-to-superior loading at the pelvis. 2014, SAE Technical Paper.

[67] Nishida, N., Izumiyama, T., et al. Changes in the global spine alignment in the sitting position in an automobile. The Spine Journal, 2020. 20(4): p. 614-620

[68] Izumiyama, T., Nishida, N., et al. Analysis of individual variabilities for lumbar and pelvic alignment in highly reclined seating postures and occupant kinematics in a collision. Proceedings 2022.

This project has received funding from the European Union's Horizon 2020 research and innovation programme under Grant Agreement 861570.

[69] De Carvalho, D.E., Soave, D., Ross, K., and Callaghan, J.P. Lumbar spine and pelvic posture between standing and sitting: a radiologic investigation including reliability and repeatability of the lumbar lordosis measure. Journal of Manipulative and Physiological Therapeutics, 2010. 33(1): p. 48-55

[70] Wagnac, E., Arnoux, P.-J., Garo, A., and Aubin, C.-E. Finite element analysis of the influence of loading rate on a model of the full lumbar spine under dynamic loading conditions. Medical & biological engineering & computing, 2012. 50(9): p. 903-915

[71] Kemper, A.R., McNally, C., and Duma, S.M. The influence of strain rate on the compressive stiffness properties of human lumbar intervertebral discs. Biomedical sciences instrumentation, 2007. 43: p. 176-181

[72] Naserkhaki, S., Arjmand, N., Shirazi-Adl, A., Farahmand, F., and El-Rich, M. Effects of eight different ligament property datasets on biomechanics of a lumbar L4-L5 finite element model. Journal of biomechanics, 2018. 70: p. 33-42

[73] Arshad, R., Pan, F., Reitmaier, S., and Schmidt, H. Effect of age and sex on lumbar lordosis and the range of motion. A systematic review and meta-analysis. Journal of biomechanics, 2019. 82: p. 1-19

[74] Yoganandan, N., Larson, S.J., et al. Correlation of microtrauma in the lumbar spine with intraosseous pressures. Spine, 1994. 19(4): p. 435-440

[75] Ochia, R.S. and Ching, R.P. Internal pressure measurements during burst fracture formation in human lumbar vertebrae. *Spine*, 2002. 27(11): p. 1160-1167

[76] John, J., Poojary, Y., Jaber, L., Thomson, R., and Iraeus, J. VIVA+ 2.0.0 Beta. 2023. DOI: 10.5281/zenodo.7789434

[77] Brynskog, E., Iraeus, J., Reed, M., Davidsson, J. (2021) Predicting pelvis geometry using a morphometric model with overall anthropometric variables Journal of Biomechanics, 126 http://dx.doi.org/10.1016/j.jbiomech.2021.110633

[78] Brynskog, E., Iraeus, J., Pipkorn, B., Davidsson, J. (2022) Population Variance in Pelvic Response to Lateral Impacts - A Global Sensitivity Analysis. Proceedings of the IRCOBI conference, Porto, Portugal, IRC-22-34

[79] Kemper, A.R., McNally, C., and Duma, S.M. Dynamic tensile material properties of human pelvic cortical bone. Biomedical sciences instrumentation, 2008. 44: p. 417-418.

[80] Dalstra, M., Huiskes, R., Odgaard, A., and Van Erning, L. Mechanical and textural properties of pelvic trabecular bone. Journal of biomechanics, 1993. 26(4-5): p. 523-535.

[81] Li, Z., Alonso, J.E., et al. Three-dimensional finite element models of the human pubic symphysis with viscohyperelastic soft tissues. Annals of biomedical engineering, 2006. 34(9): p. 1452-1462.

[82] Miller, J.A., Schultz, A.B., and Andersson, G.B. Load-displacement behavior of sacroiliac joints. Journal of orthopaedic research, 1987. 5(1): p. 92-101

This project has received funding from the European Union's Horizon 2020 research and innovation programme under Grant Agreement 861570.

[83] Dakin G. J. et al. Elastic and Viscoelastic Properties of the Human Pubic Symphysis Joint: Effects of Lateral Impact Loading, Journal of Biomechanical Engineering 123: 218-26

[84] Li Z et al, Three-Dimensional Finite Element models oft he Human Pubic Symphysis with Viscohyperelastic Soft Tissues, Annals of Biomedical Engineering, Vol. 34, No. 9 pp 1452 - 1462

[85] Guillemot H, Got C, Besnault B, et al. Pelvic Behavior in Side Collisions: Static and Dynamic Tests on Isolated Pelvic Bones. In: Proceedings of the International Technical Conference on the Enhanced Safety of Vehicles. Windsor Ontario, Canada; 1998.

[86] Kim, D.-G., Dong, X.N., et al. Evaluation of filler materials used for uniform load distribution at boundaries during structural biomechanical testing of whole vertebrae. 2006.

[87] Shergold, O.A., Fleck, N.A., and Radford, D. The uniaxial stress versus strain response of pig skin and silicone rubber at low and high strain rates. International Journal of Impact Engineering, 2006. 32(9): p. 1384-1402.

[88] Tanaka, Y., Nakashima, A., et al. Analysis of lap belt fit to human subjects using CT images. 2022, SAE Technical Paper.

[89] Mizuno, K., Hatano, W., et al. The geometrical relationship between the lap belt and occupants' anterior superior iliac spine. Proceedings of 26th International Technical Conference on the Enhanced Safety of Vehicles (ESV), Eindhoven, Netherlands, 2019.

[90] John, J., Klug, C., Kranjec, M., Svenning, E., and Iraeus, J. Hello, world! VIVA+: A human body model lineup to evaluate sex-differences in crash protection. Frontiers in bioengineering and biotechnology, 2022.

[91] Kemper, A.R., McNally, C., and Duma, S.M. Dynamic tensile material properties of human pelvic cortical bone. Biomedical sciences instrumentation, 2008. 44: p. 417-418.

[92] Natali, A. and Meroi, E. A review of the biomechanical properties of bone as a material. Journal of biomedical engineering, 1989. 11(4): p. 266-276.

[93] Katzenberger, M.J., Albert, D.L., Agnew, A.M., and Kemper, A.R. Effects of sex, age, and two loading rates on the tensile material properties of human rib cortical bone. Journal of the Mechanical Behavior of Biomedical Materials, 2019: p. 103410.

[94] Albert, D.L., Katzenberger, M.J., Agnew, A.M., and Kemper, A.R. A comparison of rib cortical bone compressive and tensile material properties: Trends with age, sex, and loading rate. Journal of the Mechanical Behavior of Biomedical Materials, 2021. 122: p. 104668.

[95] Steppacher, S.D., Meier, M.K., Albers, C.E., Tannast, M., and Siebenrock, K.A. Acetabular Cartilage thickness differs among cam, pincer, or mixed-type femoroacetabular impingement: a descriptive study using in vivo ultrasonic

This project has received funding from the European Union's Horizon 2020 research and innovation programme under Grant Agreement 861570.

measurements during surgical hip dislocation. Cartilage, 2021. 13(2_suppl): p. 465S-475S.

[96] Allan Tengg, Michael Stolz., “A Safety Gateway for Autonomous Driving Demonstrator Vehicles.” 2020. Victoria, BC, Canada : 2020 IEEE 92nd Vehicular Technology Conference, 2020. 10.1109/VTC2020-Fall49728.2020.9348861.

[97] Ejima S. et al. Prediction of pre-impact occupant kinematic behavior based on the muscle activity during frontal collision. *Paper presented at: 21th International Technical Conference on the Enhanced Safety of Vehicles (ESV);* June 15-18, 2009; Stuttgart, Germany.

[98] Reed 2021

[99] Gonzalez-Garcia M. et al., “Potential effect of pre-activated muscles under a far-side lateral impact”, Journal of Traffic Injury and Prevention, Vol. 22, 2021

[100] Gonzalez-Garcia M. et al., “Numerical Study to Quantify the Potential Influence of Pre Activated Muscles during the In Crash Phase”, Human Modeling and Simulation in Automotive Engineering, 2020

[101] Devane K. et al., “Active Human Body Models and Associated Risk of Injury for Out of Position Occupants in Frontal Crash”, Human Modeling and Simulation in Automotive Engineering, 2020

[102] Östh J. et al., “Human Body Model Muscle Activation Influence on Crash Response”, Proceedings of the IRCOBI conference, Porto, Portugal, 2022

[103] Iwamoto M. et al., “Development of a Human Body Finite Element Model with Multiple Muscles and their Controller for Estimating Occupant Motions and Impact Responses in Frontal Crash Situations”, Stapp Car Crash Journal, 56: pp.231–268, 2012

[104] Devane K. et al., “Validation of a simplified human body model in relaxed and braced conditions in low-speed frontal sled tests”, Journal of Traffic Injury and Prevention, Vol. 20, 2019

[105] Klein C., “Torque controller for active HBMs” (2021) in Davidsson J. et al., “Validated and Computationally Robust Active HBMs”, OSCCAR Deliverable D3.2 of the H2020 project OSCCAR, EC grant agreement no.: 768947

This project has received funding from the European Union’s Horizon 2020 research and innovation programme under Grant Agreement 861570.

Appendix A – Comparisons between predicted and biomechanical lumbar FSU responses

This project has received funding from the European Union's Horizon 2020 research and innovation programme under Grant Agreement 861570.

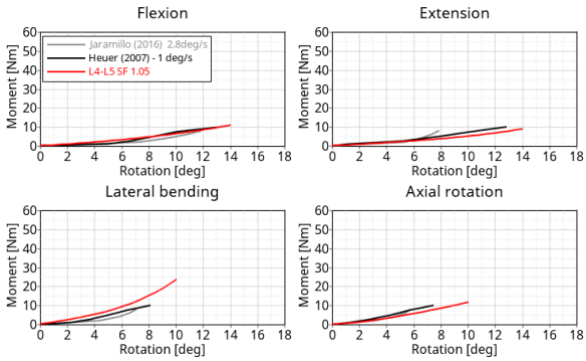

Fig. A 1. Step 1 – Only disc

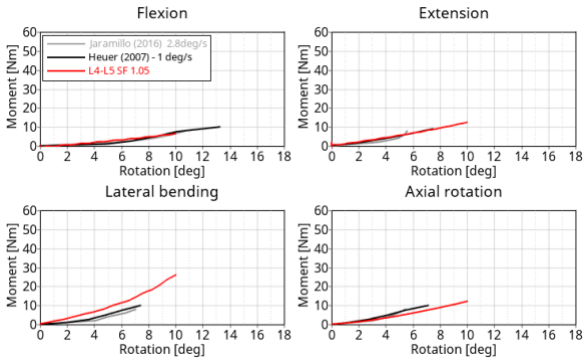

Fig. A 2. Step 2 – Anterior longitudinal ligament added (ALL offset -1.5mm)

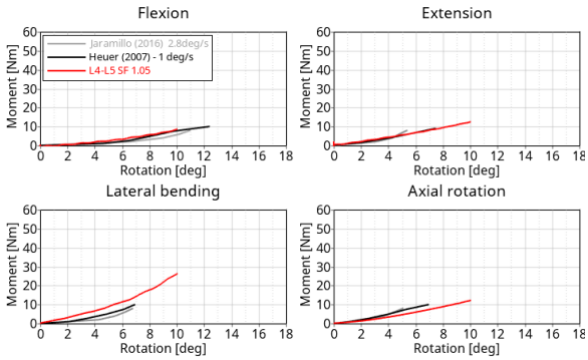

Fig. A 3. Step 3 – posterior longitudinal ligament added (PLL offset +1.5mm)

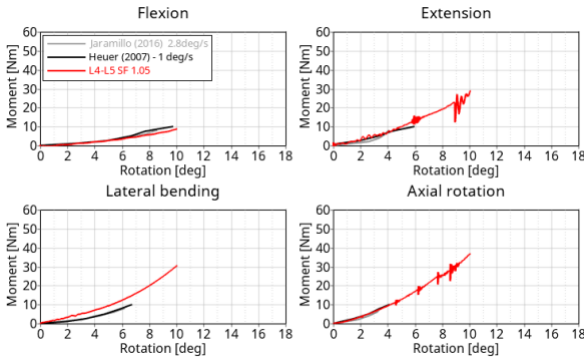

Fig. A 4. Step 4 - Vertebrae arches added

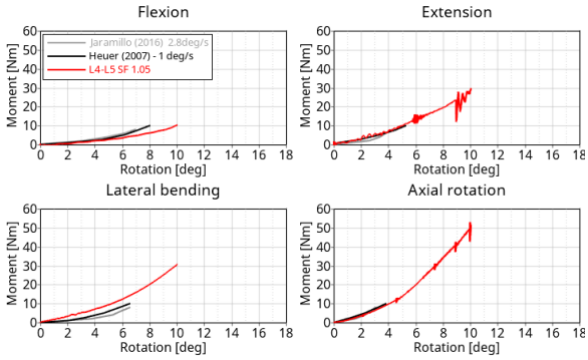

Fig. A 5. Step 5 – Facet capsules ligaments added
(FC offset +2mm)

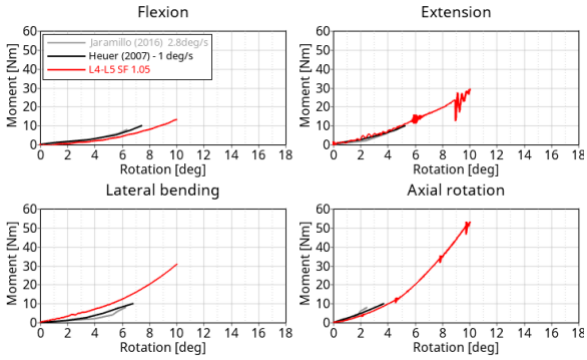

Fig. A 6. Step 6 – Flavum ligaments added
(FL offset +2mm)

This project has received funding from the European Union's Horizon 2020 research and innovation programme under Grant Agreement 861570.

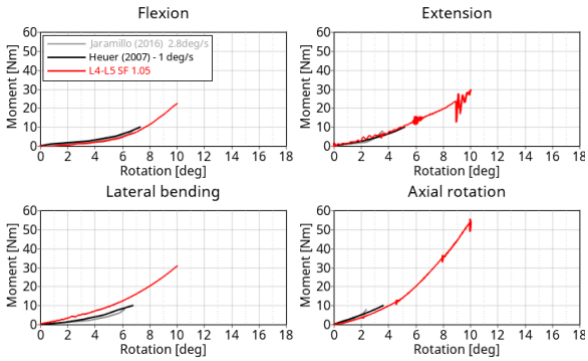

Fig. A 7. Step 7 – Interspinous ligament added (ISL offset +5mm)

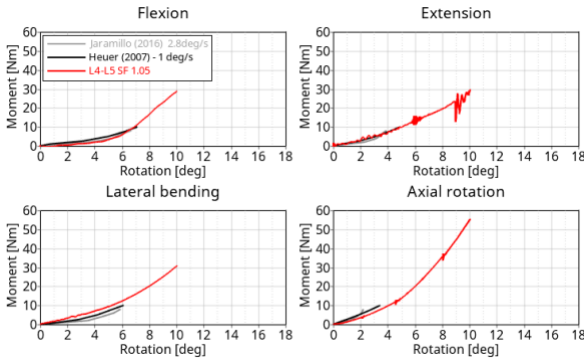

Fig. A 8. Step 8 – Intact FSU (Supraspinous ligament added) (SSL offset +5mm)

This project has received funding from the European Union's Horizon 2020 research and innovation programme under Grant Agreement 861570.

Appendix B – Available PMHS data for IRF

This project has received funding from the European Union's Horizon 2020 research and innovation programme under Grant Agreement 861570.

Author	Loading	Specimens	Reason to drop
Begeman (1994)	Shear	17 FSU	Loading condition
Belwadi (2008)	Flexion and Flexion + shear	10 T12-L2 9 L4-L5	Loading condition
Bisschop (2011)		20 FSU	Laminectomy carried out prior to testing
Bjarnason (1996)	Compression	32 isolated	Isolated
Brinckmann (1989)	Compression	98 FSU T12-L5	
Burklein (1989)	Compression	24 FSU L2-L4	Embalmed
Cheng (1997)		62 isolated	Isolated
Cyron (1979)	Shear	41 isolated	Embalmed
Cyron [68]	Neural arch bending	42 isolated	Loading condition
Demetropoulos (1998)	Compression	10 full lumbar	Unable to model loading conditions
Duma et al (2006)	Compression	FSU T12-L5	
Garges (2008)	Torsion + compression	15 FSU L2-L3 15 FSU L4-L5	Loading condition
Goel (1987)	Lateral bending and shear	6 FSU	Loading condition
Granhed (1989)	Compression of pre-flexed units	52 FSU T12-L5	
Hartensuer (2012)		7 full lumbar	Osteoporotic spine specimens were used
Hutton (1979)	Compression	17 FSU lumbar	Unable to model loading conditions
Hutton and Adams et al (1982)	Compression	16 FSU lumbar	
Jones (2011)	Compression	5 T10-L4	Unable to model loading conditions
Kifune		10 full lumbar	Unable to model loading conditions
Lagrana (2002)	Compression and Compression + flexion	3 T1x-Lx	No fracture location information
McBroom (1985)		40 isolated	Isolated
McCubbrey (1995)		20 FSU	No fractures recorded during testing
Moro (1994)		11 L1-L3	Unable to model loading conditions
Mykleburst (1983)		14 FSU 32 isolated	Unable to model loading conditions
Ochia [69]	Compression	24 isolated L4/L5	Isolated
Oswalder (1993)	Flexion	20 FSU L1-L2 or L3-L4	Unable to model loading conditions

This project has received funding from the European Union's Horizon 2020 research and innovation programme under Grant Agreement 861570.

Schultz (1979)		44 FSU	No fractures
Singer (1995)		76 isolated	Embalmed
Skzrypiec (2012)	Shear	21 FSU L2-L3	Loading condition
Stemper (2015)	Compression	8 full lumbar	Unable to model loading conditions
Tushak et al (2022)	Compression + Flexion	40 FSU T12-L2, L3-L5	
Yoganandan (1988)	Flexion and compression/Compression	35 full lumbar	Unable to model loading conditions
Yoganandan (1988)	Compression,	63 isolated	Unable to model loading conditions
Yoganandan (1994)		10 full lumbar	Unable to model loading conditions
Yoganandan (2013)	Compression	15 full lumbar	Unable to model loading conditions
Yoganandan (2018)	Compression	5 full lumbar	Unable to model loading conditions

This project has received funding from the European Union's Horizon 2020 research and innovation programme under Grant Agreement 861570.

Appendix C – Inclusion and exclusion of PMHS test data

The following inclusion and exclusion criteria were deployed in this study:

- Data from tests on FSUs that were from embalmed subjects were exclude.
- Data from tests on FSUs from individuals with any history of spinal fractures/surgery or with osteoporosis were exclude.
- Only data from tests on lumbar FSUs consisting of two or three vertebrae with discs were included in the development of the injury risk function.
- Data from test on isolated vertebrae were excluded.
- Only data from test were the inferior and superior ends of the FSUs were fixed to the loading device with some resin of know stiffness were include in the development of the injury risk function.
- Only test data from experiments on FSUs where the boundary conditions and initial spine curvatures are clearly defined were included.
- Only test data from experiments on FSUs where injury data, location of the injury and type of injury, are available were included.

This project has received funding from the European Union's Horizon 2020 research and innovation programme under Grant Agreement 861570.

Appendix D – Reconstructions of original tests

FSU in pure compression by Brinckmann et al.1989

Brinckmann et al. carried out quasi-static compressive tests on 98 fresh spine FSUs from T12 to L5. These FSUs consisted of two adjacent vertebral bodies with intervertebral disc. The posterior elements were intact. The superior surfaces of the superior vertebrae and the inferior surfaces of the inferior vertebrae were attached to the loading devices using a block of high-density bone cement. In the tests, the caudal ends of the FSUs were rigidly fixated while the other ends were loaded at a rate of 1 kN/s. Prior to testing, the mid-plane of the disc was orientated parallel to the horizontal plane. Hence, there were no lordotic spine curvature present during spines testing. The tests were stopped at the first signs of fracture; load and fracture type were reported. An endplate fracture was reported in 41 of the 98 specimens tested.

The block of bone cement was modelled using *MAT_ELASTIC with young's modulus 2.9 GPa and density 1.18 g/cm3 in the LS-DYNA. The block was attached to the vertebrae using *CONSTRAINT_SHELL_IN_SOLID_PENALTY. Rigid shell surfaces were defined at the bottom and top surface of the modelled blocks to define boundary conditions. The bottom surface was constrained in all directions while loads were described for the upper surface using *LOAD_RIGID_BODY at 1kN/s. Simulations were done for male and female separately and until the load reached 10 kN. LUMB_FLEX parameter was -0.5.

Lumbar FSU Pure compression by Duma et al. 2006

Duma et al. conducted compression tests on thawed FSUs from 4 male PMHSs. Each end of the FSUs was secured to the loading device using bonding compound. The mid-plane of the disc was positioned parallel with the potting cup, and that the disc was centered in the potting cup. The specimens were loaded at a rate of 1 m/s until fracture. All the tests resulted in endplate fractures.

The bonding compound was modelled using the model *MAT_ELASTIC with young's modulus 2.9 GPa and density 1.18 g/cm3. The spine was connected to the models of the bonding compound using *CONSTRAINED_SHELL_IN_SOLID_PENALTY. The surfaces of the bottom and the top of the models of the bonding compound were lined with rigid shell elements to define boundary conditions. The bottom surface of the bottom model of the bonding compound were constrained in all directions. A prescribed load at 1m/s was applied to the upper model of the bonding compound using *BOUNDARY_PRESCRIBED_MOTION. Individual simulations were carried out for each test condition. LUMB_FLEX parameter was -0.5.

This project has received funding from the European Union's Horizon 2020 research and innovation programme under Grant Agreement 861570.

Lumbar FSU Pure compression by Granhed et al. 1989

Granhed et al. carried out quasi-static compression tests on 52 flexed lumbar FSUs. These units consisted of two adjacent vertebrae with intervertebral disc harvested from the fresh cadavers. The extremities of the specimens were attached to the loading devices using plastic cement. The posterior elements were intact. The specimens were initially flexed to 5, 10 or 15° and thereafter loaded in axial compression at 12 mm/min. The tests were stopped at fracture. Two types of fractures were reported; while only the 29 segments that exhibited endplate fractures were reconstructed in this study. Five specimens that had no notable fracture after the tests were also reconstructed.

The plastic cement blocks were modelled using material model *MAT_ELASTIC with young's modulus 0.75 GPa and density 1.44 g/cm3. The blocks were attached to the vertebrae using *CONSTRAINT_SHELL_IN_SOLID_PENALTY. In addition, a surface of rigid shells was defined at the bottom and top surfaces of the two blocks. The FSU models were flexed to 5, 10 and 15°, depending on load case to be modelled, in a pre-simulation by rotating both blocks. After the pre-simulation was carried out the top block was constrained in rotation and the bottom block was constrained in all directions. Then the upper block was prescribed with a velocity of 12mm/min to a displacement of about 4 mm using *BOUNDRY_PRESCRIBED_MOTION. A specific simulation was carried for each test configuration. LUMB_FLEX parameter was -0.5.

Lumbar FSU Flexion-compression by Hutton and Adams 1982

Hutton and Adams et al. tested 33 lumbar FSUs, some fresh others thawed, with two vertebrae and an intervening disc. Both ends of the FSUs were attached to the loading devices using dental plaster. The specimens were initially flexed to a prescribed angle followed by compressive loading at a rate of 3000 N/s. Loading was removed at the time of fracture. The loading produced endplate fractures in all the tests.

The dental plaster block was modelled using LS-DYNA material model *MAT_ELASTIC with young's modulus 0.75 GPa and density 1.44 g/cm3. The spine was connected to the blocks using the LS-DYNA keyword *CONSTRAINED_SHELL_IN_SOLID_PENALTY. Top and bottom surfaces of the two blocks were lined with rigid shell elements to define boundary conditions. The bottom surface of the bottom block was constrained in all directions. A pre-simulation was executed where to FSUs were flexed to the specified angle using *BOUNDRY_PRESCRIBED_MOTION of the upper block. After the pre-simulation was carried out, the top block was constrained in rotation while a compressive load that increasing by 3 kN/s until the load reached ~15kN was modelled using *BOUNDRY_PRESCRIBED_MOTION. Individual simulations were executed for each test condition. LUMB_FLEX parameter was -0.5.

This project has received funding from the European Union's Horizon 2020 research and innovation programme under Grant Agreement 861570.

Lumbar FSU Flexion-compression by Tushak et al. 2022

Tushak et al. applied flexion loading on 40 thawed lumbar FSUs following compression loading. These FSUs consisted of 3-vertebrae and intervening discs from fresh frozen PMHS. Both ends of the FSUs were potted/attached to the loading devices using a hardening resin. The superior loading device was constrained in translation in all directions but allowed to rotate about the centre of the inferior potting cup (indicated with a cross in Fig. 4). The inferior loading devices was constrained in rotation but was allowed to translate in the X- and Z-direction. The lower potting was positioned parallel to the inferior endplate of the inferior vertebra and the upper potting was positioned parallel to superior endplate of the superior vertebra. In each of the tests, a quasi-static compressive load was applied to the upper loading device until a block of honeycomb, placed underneath the bottom loading device, started to crush. Then a dynamic flexion load was applied, at a peak rate of 600 °/s, to the upper loading device. The tests produced endplate and cortical bone failures.

In the simulation of these tests, the resin block was modelled using model *MAT_ELASTIC with young's modulus 2 GPa and density 1.5 g/cm3. The vertebrae models were connected to the models of the resin blocks using the *CONSTRAINED_SHELL_IN_SOLID_PENALTY. The bottom and top surfaces of the blocks were lined with rigid shell elements to define boundary conditions. The inferior block was free to move in anterior-posterior and axial directions. The superior block was constrained in translation in all directions while allowed to rotate about the centre of the inferior potting cup. The lower block was modelled so that the inferior endplate of the lower vertebra was parallel to the bottom surface of the block. The first step in the simulations was to apply a quasi-static compressive load, a defined "crush force", that was maintained throughout the simulation. This "crush force" was attained by ramping up to the reported initial compressive load using a lead time selected based on iterations to avoid dynamic effects. A flexion was thereafter applied to the superior model of the resin block and its rate was based on the average rotational acceleration time plots provided in the publication (peak rate of 600 °/s). The termination time for the simulation was set based on the reported final flexion angle. Individual simulations were carried out for each test. LUMB_FLEX parameter was -0.5.

This project has received funding from the European Union's Horizon 2020 research and innovation programme under Grant Agreement 861570.

Appendix F – Occupant response corridors

Braking 50 kph, aware, reclined vs. upright		
	Male	**Female**
Head	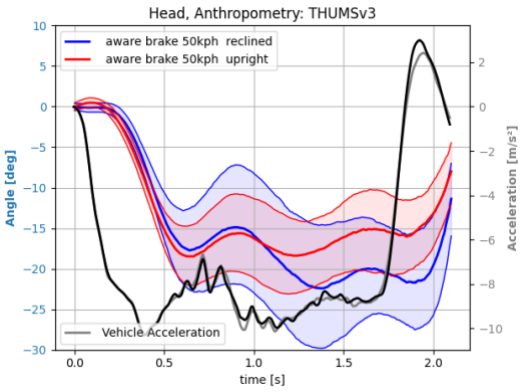	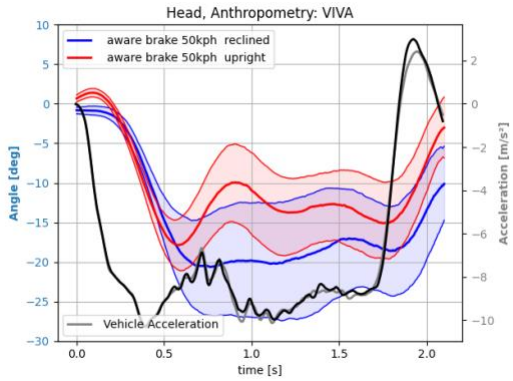
Torso	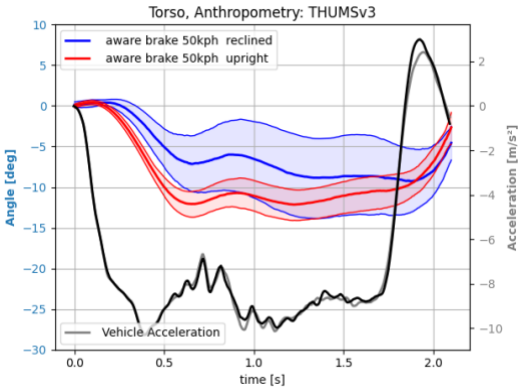	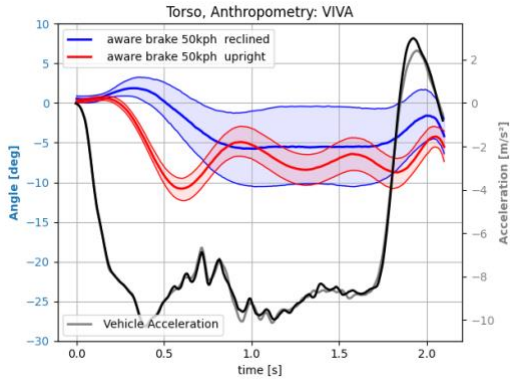

This project has received funding from the European Union's Horizon 2020 research and innovation programme under Grant Agreement 861570.

Braking 50 kph, reclined, aware vs. unaware		
	Male	**Female**
Head	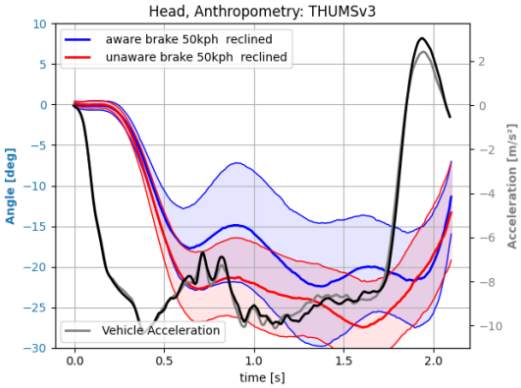	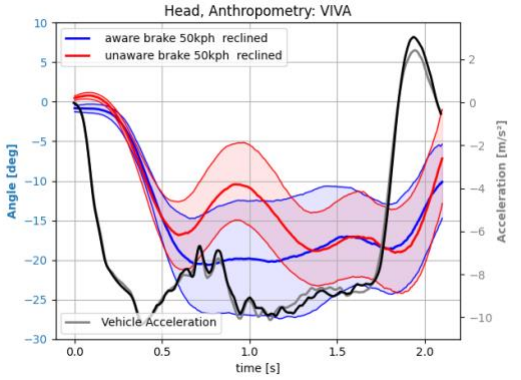
Torso	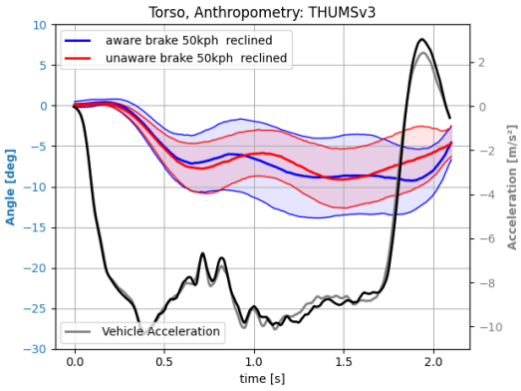	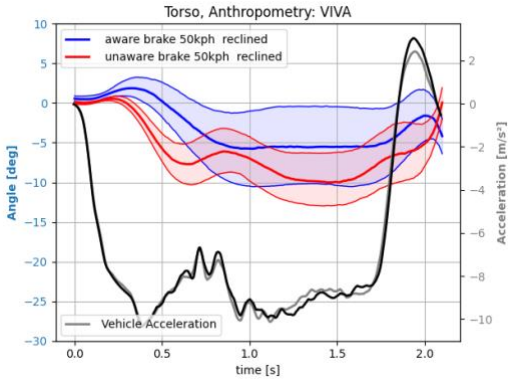

This project has received funding from the European Union's Horizon 2020 research and innovation programme under Grant Agreement 861570.

Steering, reclined, unaware – left vs. right		
	Male	**Female**
Head	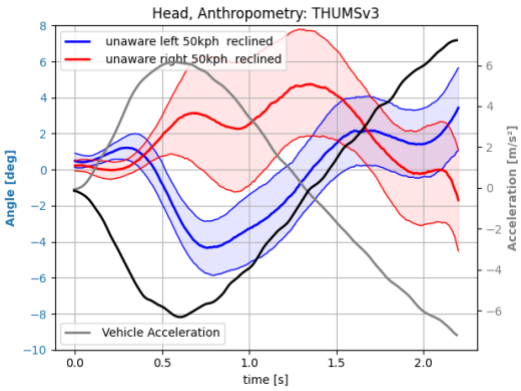	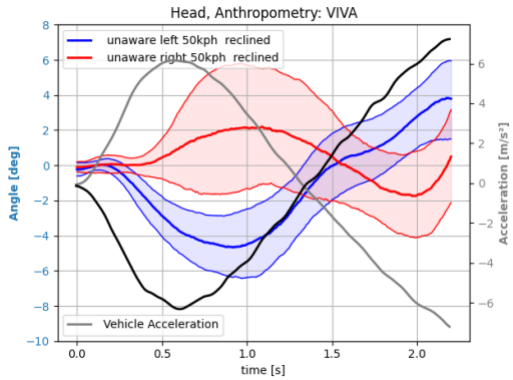
Torso	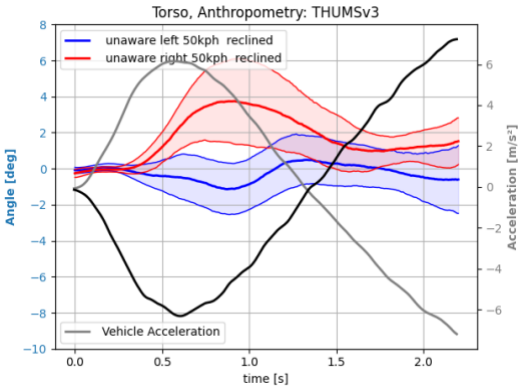	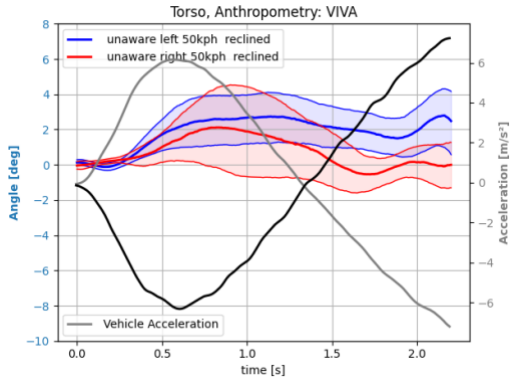

This project has received funding from the European Union's Horizon 2020 research and innovation programme under Grant Agreement 861570.

Steering, reclined, aware – left vs. right		
	Male	**Female**
Head	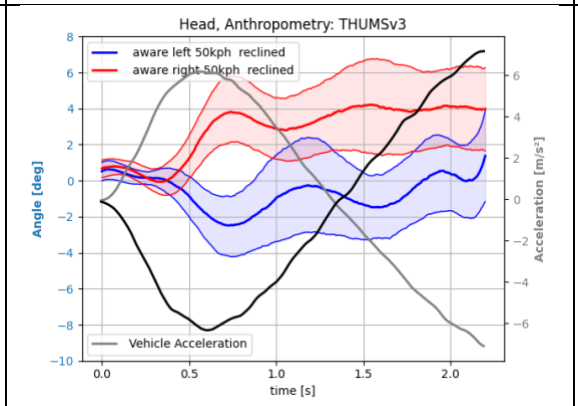	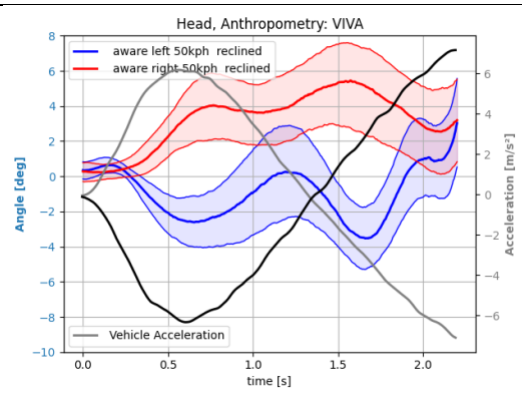
Torso	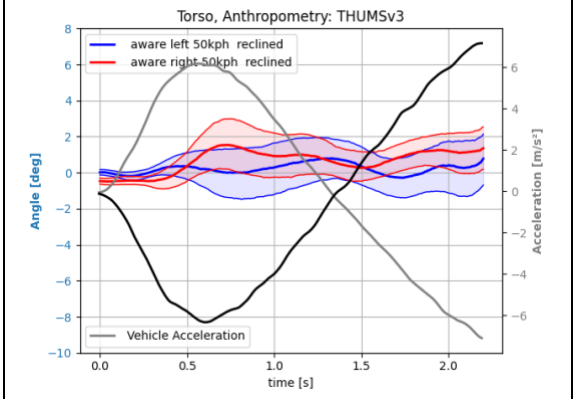	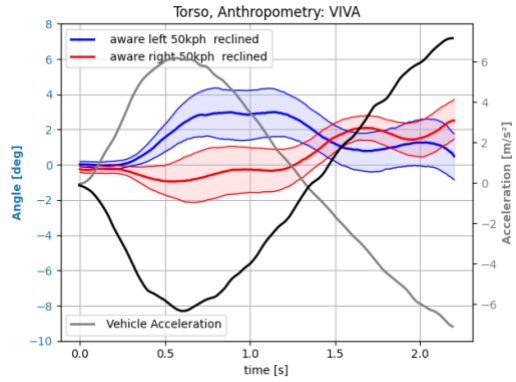

This project has received funding from the European Union's Horizon 2020 research and innovation programme under Grant Agreement 861570.

Steering left, aware, reclined vs. upright		
	Male	**Female**
Head	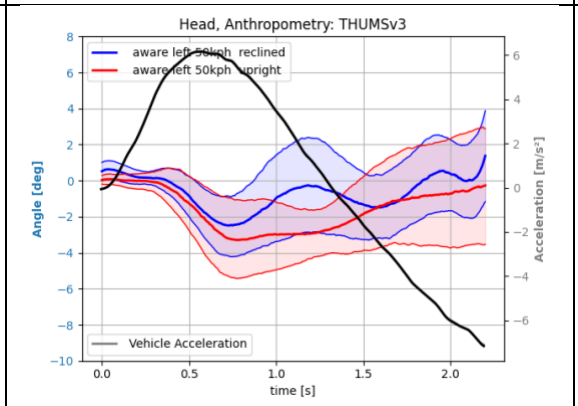	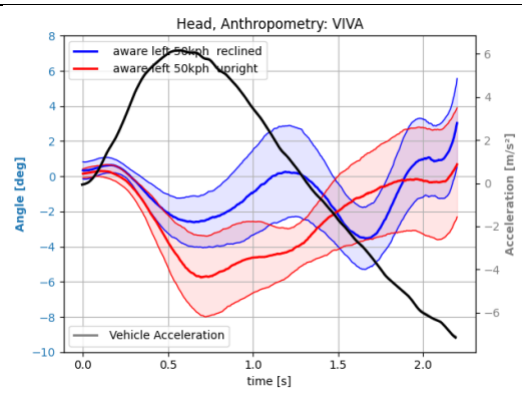
Torso	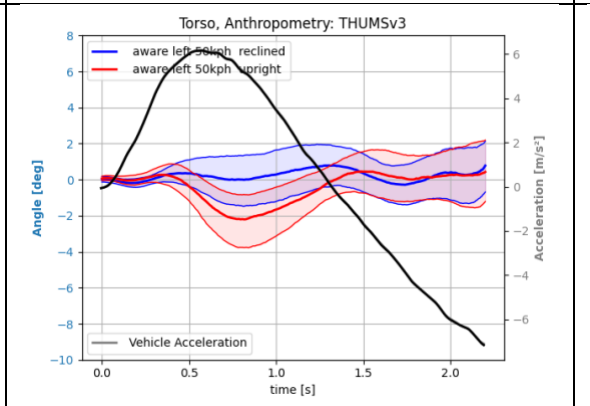	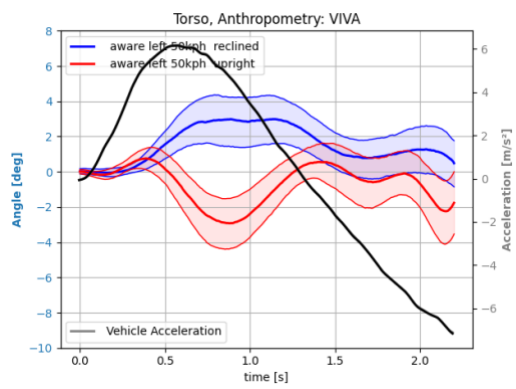

This project has received funding from the European Union's Horizon 2020 research and innovation programme under Grant Agreement 861570.

Steering right, aware, reclined vs. upright		
	Male	**Female**
Head	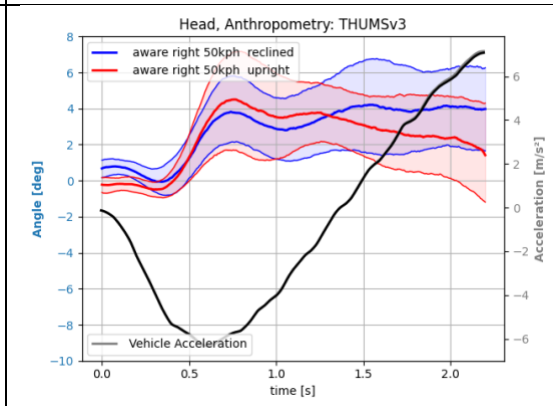	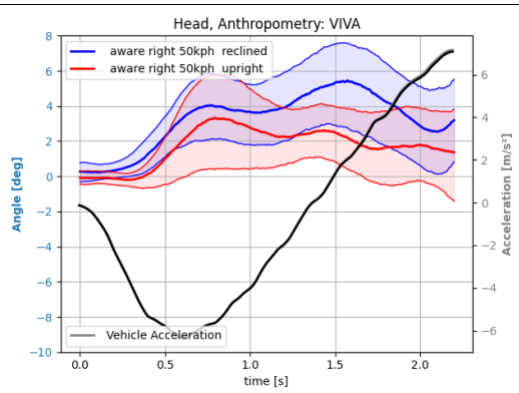
Torso	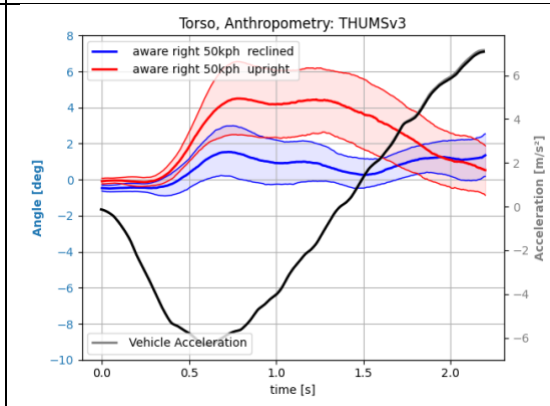	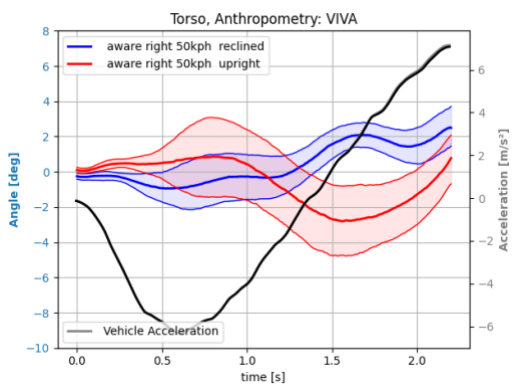

This project has received funding from the European Union's Horizon 2020 research and innovation programme under Grant Agreement 861570.